Review

Imaging Atomic Orbital Polarization in Photodissociation

Arthur G. Suits, and Oleg S. Vasyutinskii

Chem. Rev., **2008**, 108 (9), 3706-3746 • DOI: 10.1021/cr040085c • Publication Date (Web): 06 August 2008

Imaging Atomic Orbital Polarization in Photodissociation

Arthur G. Suits*,† and Oleg S. Vasyutinskii*,‡

Department of Chemistry, Wayne State University, 5101 Cass Avenue, Detroit, Michigan 48202, and Ioffe Physico-Technical Institute, Russian Academy of Sciences, 194021 St. Petersburg, Russia

Received June 13, 2007

Contents

1. Introduction 3706
2. Theoretical Foundation 3707
2.1. Quantum Mechanical Description of Photofragment Polarization Angular Distributions 3707
2.1.1. State Multipole Representation 3708
2.1.2. Dissociation Wave Function Expansion 3709
2.1.3. Photofragment State Multipole Angular Distribution: Axial Recoil and Quasiclassical Approximations 3709
2.1.4. Dynamical Functions 3710
2.1.5. Long-Range Coefficients $\mathscr{T}$ 3711
2.1.6. Rotational Factors 3713
2.1.7. Multipole Angular Distributions: Laboratory Frame 3713
2.1.8. Molecular Frame State Multipoles and Polarization Parameters 3717
2.1.9. Role of J, J' Coherence in Molecular Photodissociation 3720
2.1.10. Photofragment State Multipole Angular Distribution: Slow Predissociation 3720
2.2. Detection of the Photofragment Polarization Using 2 + 1 REMPI 3721
2.2.1. General Expressions for the 2 + 1 REMPI Signal 3721
2.2.2. Isolation of a Particular Rank State Multipole 3722
2.2.3. Determination of the Anisotropy Parameters from 2-Dimensional Velocity Images 3723
2.2.4. 2D Slice Image Basis Functions 3724
3. Experiment: Imaging Probes of Orbital Polarization 3725
3.1. Experimental Approach 3725
3.2. Applications: Diatomics 3726
3.2.1. Dihalogens 3726
3.2.2. Interhalogens XY 3728
3.2.3. HX 3730
3.2.4. O_2 3734
3.2.5. RbI 3735
3.3. Applications: Triatomic and Polyatomic Molecules 3736
3.3.1. NO_2 3736
3.3.2. N_2O 3737
3.3.3. O_3 3738
3.3.4. OCS 3741
3.3.5. SO_2 3742
3.3.6. Ethylene Sulfide 3743
4. Acknowledgments 3743
5. References 3744

* Corresponding authors.
† Wayne State University. E-mail: asuits@chem.wayne.edu.
‡ Russian Academy of Sciences. E-mail: osv@pms.ioffe.ru.

1. Introduction

In the late 1980s, Dixon, Hall, Houston, Simons, and others[1–6] recognized that experiments that probe the angular distribution of photofragments with spectroscopic techniques could be used to obtain the angular distribution of angular momentum polarization. These were generalized as "vector correlation" experiments, wherein one examines the correlations among the angular momentum polarization vector, the product recoil direction, the transition moment in the parent molecule, the laser polarization, the fluorescence polarization, or in scattering experiments, the relative velocity vector. Virtually all of the early studies were based on Doppler spectroscopy and emphasized rotational angular momentum polarization. Semiclassical models were used to interpret the experiments, largely, based on the bipolar harmonics approach introduced by Dixon.[5] Around the same time, Chandler and Houston introduced the ion-imaging technique,[7] in which the full recoil velocity distribution of state-resolved photofragments could be detected in a highly multiplexed approach. Soon thereafter, large orbital alignment effects in atoms were seen in imaging experiments, and it was immediately recognized that the semiclassical picture, developed to describe high-J rotational polarization, would not be suitable for interpretation of angular momentum polarization in atoms, and a new, fully quantum theory was required. The foundation for this theory was established in a paper in 1994 by Siebbeles et al.[8] (see also the earlier paper by Vasyutinskii).[9] The development of the theory is described fully in section 2.

These studies, probing the angular distribution of photofragment alignment and orientation, build upon a considerable history of investigation of angular momentum polarization, both in photodissociation[10–14] and in scattering.[15–19] The early photodissociation studies, however, examined the alignment or orientation integrated over the entire product angular distribution. These global measurements could not decompose the contributions of coherent and incoherent mechanisms and were thus of limited value in exploration of the underlying dynamics. The power of the present techniques lies in their ability to reveal the molecular-frame dynamics, to reveal coherent excitation mechanisms involving multiple electronic states, and to explore nonadiabatic processes at curve crossings and at long-range.[20,21] In short, they afford the full quantum insight into the dissociation

10.1021/cr040085c CCC: $71.00
Published on Web 08/06/2008

Arthur G. Suits is Professor of Chemistry and member of the Academy of Scholars at Wayne State University. He obtained a B.S. in Chemistry from the University of Missouri, Columbia, in 1986 and a Ph.D. from the University of California, Berkeley, under the supervision of Y. T. Lee. Following post-doctoral work at Cornell University with Paul Houston, he joined the staff at the Lawrence Berkeley National Laboratory. From 2000 to 2004, he held joint appointments at Stony Brook University and Brookhaven National Laboratory. In 2004, he joined the faculty at Wayne State. His research interests are in chemical reaction dynamics, chemical physics, astrochemistry, and new directions in mass spectrometry. He is a Fellow of the American Physical Society and was recently elected Vice-Chair of its Division of Chemical Physics.

Oleg S. Vasyutinskii is Leading Scientist of the Ioffe Institute, Russian Academy of Sciences, St. Petersburg, Russia, Professor of St. Petersburg Polytechnical University, and Adjunct Professor of Chemistry at Wayne State University, Detroit. He obtained his B.S. in Physics from the Polytechnical University, St.Petersburg and a Ph.D. in 1984 from the Ioffe Institute, St.Petersburg, under the supervision of Prof. R. A. Zhitnikov. After post-doctoral research at the University Paris VI, Paris, France, with Prof. M. Glass-Maujean in 1992−1993, he obtained the Russian Doctor of Sciences (Habilitation) degree in the Ioffe Institute in 1995. In 2001, he was rewarded with the International Humboldt Research Award and, in 2003, with the Konstantinov Award of the Ioffe Institute. His research interests are in processes of interaction between matter and radiation as well as in interaction and dynamics of the atomic, molecular, and cluster particles in the microscopic (nanometer) scale, in particular in dynamics of molecular photodissociation, reaction dynamics, and multiphoton spectroscopy. He is the Fellow of Institute of Physics (U.K.), Correspondent-Member of the Russian Academy of Natural Sciences, and the Member of the Editorial Broad of the International Journal of Quantum Chemistry.

event allowed by nature. These studies have led to observation of a series of remarkable new phenomena, such as the unexpectedly high photofragment polarization in photodissociation of polyatomic molecules, observation of a pure coherent quantum mechanical mechanism for production of atomic photofragment polarization, [22] observation of coherences showing that the electron cloud in the recoiling atom "remembers" the original molecular plane,[23] and observation of energy-dependent quantum oscillations in the cross section of photofragment polarization.[24,25] The latter has been exploited as a means of "seeing matter waves", that is, mapping the wave function for the dissociating molecule itself. More recently these studies have shown the possibility for direct experimental determination of the probability of nonadiabatic transitions and phase differences between different reaction channels.[26,27] This capability of monitoring the phase shifts between different outgoing reaction wave packets is quite new in the field of molecular dynamics and can find important applications for control of chemical reactions and for chemical reactions of ultracold molecules. We will examine all of these advances.

This rapidly growing field has not been reviewed in depth recently, but we note our earlier overview,[21] as well as recent reviews from Brouard and co-workers on atomic polarization in dissociation of diatomic[28] and polyatomic molecules,[29] that has some overlap with the material presented here. Our goal is to provide, for studies that probe the angular distribution of atomic orbital polarization in photodissociation, a single, comprehensive treatment of all relevant theory, as well as a thorough review of all experiments to-date. The emphasis here will be on results obtained using ion imaging techniques, clearly now the method of choice. However, alternative techniques have been used with considerable success to obtain the same information, in particular, core sampled ion time-of-flight (TOF) profiles used by Zare et al. [24,25,30–32] and Doppler and related methods by Vasyutinskii et al.[33,34] Results from these experiments will be considered as well. The outline of the article is as follows: In the following section, we establish the theoretical foundation of these studies, first providing an overview of the quantum mechanical description of photodissociation, then presenting the means of probing these events using $2 + 1$ REMPI and ion imaging. Finally, we provide a thorough summary of the experiments performed to-date, mostly on diatomic and triatomic systems. We have sought to prepare this review so that the reader who is solely interested in current state of experimental investigation of these phenomena may skip the detailed theoretical treatment in the following section and proceed directly to section 3. However, those interested in implementing the theoretical analysis of these experiments should find everything necessary in the following pages.

2. Theoretical Foundation

2.1. Quantum Mechanical Description of Photofragment Polarization Angular Distributions

The quantum mechanical theory for the angular distribution of polarized photofragments has been built by several authors.[8,9,26,35–44] Below we follow the approach of Siebbeles and co-workers[8] that results in analytical expressions for the photofragment angular distributions, which have been widely adopted for interpretation of the imaging experiments.

We consider the generic molecular photodissociation event in which the molecule AB produces fragments A and B. Each fragment can be either an open-shell atom or molecular radical. Fragments A and B have angular momenta $\mathbf{j_A}$ and $\mathbf{j_B}$, respectively, with z-components of m_A and m_B about the space-fixed $\mathbf{Z}$ axis. The initial and excited-state total angular momenta of the molecule are $\mathbf{J_i}$ and $\mathbf{J}$, respectively, and the corresponding space-fixed z-components are M_i and M. For

simplicity, we assume that an isotropic distribution of the angular momenta of the parent molecule, which means all initial M_i states are equally populated. A general case of polarized parent molecules has been investigated by Fuglesang et al.[40]

The generalized differential photodissociation cross section matrix elements $\sigma(\hat{\mathbf{k}}, E; \tilde{n}', \tilde{n})$ are specified by the total energy E of the fragments, the relative recoil direction $\hat{\mathbf{k}}$, and the index $\tilde{n}$, which is the set of quantum numbers specifying the electronic states and angular momenta (j_A, m_A, j_B, m_B) of the fragments. The diagonal elements of the matrix ($\tilde{n} = \tilde{n}'$) are the normal photofragmentation cross sections that give the probability of producing each fragment with a specific quantum numbers j_A, m_A, or j_B, m_B. The off-diagonal elements (for instance, $m_A \neq m'_A$) describe the coherence between different quantum states.[45,46]

Using first order time-dependent perturbation theory, the generalized photofragmentation cross section $\sigma(\hat{\mathbf{k}}, E; \tilde{n}\ n')$ can be written as[35,37,45]

$$\sigma(\hat{\mathbf{k}}, E;\ \tilde{n}', \tilde{n}) = \frac{2\pi^2\nu}{c\varepsilon_o(2J_i+1)} \sum_{M_i,M'_i} \langle \Psi^{-(\hat{\mathbf{k}},\tilde{n}')}(\mathbf{R}, \mathbf{r}, E)|\hat{\mathbf{d}}\cdot\mathbf{e}|\Psi_{J_iM'_i}\rangle \times \langle \Psi^{-(\hat{\mathbf{k}},\tilde{n})}(\mathbf{R}, \mathbf{r}, E)|\hat{\mathbf{d}}\cdot\mathbf{e}|\Psi_{J_iM_i}\rangle^* \rho^{J_i}_{M'_i,M_i} \quad (1)$$

where ν is the frequency of the incident light, $\mathbf{e}$ is a light polarization vector, $\hat{\mathbf{d}}$ is a dipole operator, $\mathbf{R} \equiv \mathbf{R}(\theta_R, \phi_R)$ is the vector specified by the polar angles θ_R and ϕ_R, which connects the centers of mass of the fragments, while $\mathbf{r}$ denotes collectively all the internal coordinates of the fragments.

In eq 1, Ψ_{J_i,M_i} is the wave function of the initial molecular state, $\rho^{J_i}_{M'_i,M_i}$ is the density matrix of the parent molecules and $\Psi^{-(\hat{\mathbf{k}},\tilde{n})}(\mathbf{R}, \mathbf{r}, E)$ is the scattering wave function describing two photofragments recoiling at a total energy $E = E_i + h\nu$ in a direction specified by the unit vector $\hat{\mathbf{k}}$, angles θ, ϕ. In this review, we do not consider the anisotropy in the parent molecules; therefore, the density matrix in the *rhs* of eq 1 is taken equal to unity, $\rho^{J_i}_{M'_i,M_i} = \delta_{M_i,M'_i}$.

Equation 1 describes a steady-state condition for photodissociation by monochromatic light of frequency ν. This is also appropriate if pulsed nanosecond lasers are employed as is commonly the case in photodissociation studies. Such experiments usually involve the detection of only one of the two products and therefore do not yield correlated measurements on both fragments. Moreover, the coherence between different fragment j_A, j'_A states has so far not been studied experimentally. Therefore, the cross section corresponding to the current experimental conditions involves $j_A = j'_A$ and averaging over the quantum numbers of the other, nondetected, fragment. Following the procedure recently used by Balint-Kurti and co-workers,[26] the differential cross section $\sigma(\hat{\mathbf{k}}, E;\ j_A, m'_A, j_B, m'_B; j_A, m_A, j_B, m_B)$ in eq (1) can be expanded over the cross sections $\sigma(\hat{\mathbf{k}}, E; j_A, j_B, j', m', j, m)$, where j and m are total angular momentum of the photofragments and its laboratory frame projection and then averaged over the j_B, m_B-states of the fragment B

$$\sigma^{j_A}_{m'_A;m_A}(\theta, \phi) = \sum_{j_Bm_B} \sum_{j,m} \sum_{j',m'} C^{j'm'}_{j_Am'_Aj_Bm_B} C^{jm}_{j_Am_Aj_Bm_B} \times \sigma(\hat{\mathbf{k}}, E; j_A,\ j_B, j', m', j, m) \quad (2)$$

where $C^{jm}_{j_Am_Aj_Bm_B}$ is a Clebsch−Gordan coefficient.

2.1.1. State Multipole Representation

One may recast the elements of the generalized differential cross section in eq 2, $\sigma^{j_A}_{m'_A;m_A}(\theta, \phi)$ using the angular momentum state multipoles $\rho_{KQ}(\theta, \phi)$, which are spherical tensors of rank K and projection Q

$$\rho_{KQ}(\theta, \phi) = \frac{(2K+1)^{1/2}}{(2j_A+1)^{1/2}\sigma_0} \sum_{m'_A,m_A} (-1)^{j_A-m_A} \times \begin{pmatrix} j_A & j_A & K \\ m_A & -m'_A & -Q \end{pmatrix} \sigma^{j_A}_{m'_A;m_A}(\theta, \phi) \quad (3)$$

where $\sigma_0 = (2_{j_A} + 1)^{-1/2}\langle Tr[\sigma^{j_A}_{m'_A;m_A}(\theta, \phi)]\rangle$ and the angle brackets signify integration over the angles θ and ϕ. The factor (:::) in eq 3 is a $3-j$ symbol.[47]

The definition of the photofragment state multipoles $\rho_{KQ}(\theta, \phi)$ in eq 3 is similar to that commonly used elsewhere;[45,46,48] however, it is not the same because the state multipoles in eq (3) depend on the recoil angles θ and ϕ. Unlike the conventional normalization rule,[45,46,48] the $\rho_{00}(\theta, \phi)$ element in eq 3 is not equal to a normalization constant but describes the photofragment angular distribution, as shown below. Instead, the state multipoles $\rho_{KQ}(\theta, \phi)$ in eq 3 obey the normalization condition $\langle\rho_{00}(\theta, \phi)\rangle = (2j_A + 1)^{-1/2}$ (where again the angle brackets mean averaging over the recoil angles.) The inverse relationship is

$$\sigma^{j_A}_{m'_A;m_A}(\theta, \phi) = (2j_A+1)^{1/2}\sigma_0 \sum_{K,Q} (-1)^{j_A-m_A}(2K+1)^{1/2} \times \begin{pmatrix} j_A & j_A & K \\ m_A & -m'_A & -Q \end{pmatrix} \rho^{j_A}_{KQ}(\theta, \phi) \quad (4)$$

In principle, the multipole rank K in eq 3 ranges from $K = 0$ to $2j_A$,[46] although for atomic photofragments only several lowest ranks need usually be considered. For instance, complete description of the $^1D_2$ oxygen atomic fragments requires up to $K = 4$ rank state multipoles [$K = 0$ (photofragment density), 1 (orientation), 2 (alignment), 3 (octupole moment), and 4 (hexadecapole moment)]. In many cases, the low-rank state multipoles with $K = 0$, 1, and 2 dominate experimental data; however, later we will encounter examples where the contribution from the high-rank terms $K = 3$ and 4 are also important.

Because of the symmetry of the $3-j$ symbols in eqs 3 and 4, the quantum number Q is constrained to the value $Q = m_A - m'_A$. Therefore, the terms with $Q = 0$ describe the normal (incoherent) differential cross sections, while the terms with $Q \neq 0$ describe the coherence between different photofragment quantum states.

An important advantage of the state multipole representation is that in the absence of external fields each state multipole ρ_{KQ} can be treated separately from all others.[46] Another important result is that in many practically important cases each state multipole has a unique spatial angular distribution and can in principle be separately determined from experiment. The determination of all independent photofragment cross sections (state multipoles) in an experiment is equivalent to the complete quantum mechanical photodissociation experiment, which provides the researcher with all quantum mechanical amplitudes and phases that arise from theory. The terminology of the "complete experiment" was introduced by Fano and Macek[49] and is widely used in photoionization studies. Recent developments in experimental technique and theory provide, in principle, the possibility

for carrying out complete experiments in photodissociation and reaction dynamics as well.

The fragment state mutipoles with rank K in eq 3 have clear physical meaning, being proportional to the mean fragment multipole moments.[46] They are related to the known multipole parameters $A_{KQ}(\theta, \phi)$ by the transformation formulas[45]

$$A_{1Q} = \frac{1}{\sqrt{3}}\frac{[\rho_{1Q}]}{\rho_{00}} = \frac{\langle j_Q^{(1)}\rangle}{[j(j+1)]^{1/2}} \quad (5)$$

$$A_{2Q} = \left[\frac{(2j+3)(2j-1)}{5j(j+1)}\right]^{1/2}\frac{[\rho_{2Q}]}{\rho_{00}} = \sqrt{6}\frac{\langle j_Q^{(2)}\rangle}{j(j+1)} \quad (6)$$

$$A_{3Q} = \frac{[(2j+3)(2j-1)(j+2)(j-1)]^{1/2}}{2\sqrt{7}j(j+1)}\frac{[\rho_{3Q}]}{\rho_{00}} = \frac{\sqrt{10}}{2}\frac{\langle j_Q^{(3)}\rangle}{[j(j+1)]^{3/2}} \quad (7)$$

$$A_{4Q} = \frac{[(2j+5)(2j+3)(2j-1)(2j-3)(j+2)(j-1)]^{1/2}}{4\sqrt{9}[j(j+1)]^{3/2}} \times \frac{[\rho_{4Q}]}{\rho_{00}} = \frac{\sqrt{70}}{4}\frac{\langle j_Q^{(4)}\rangle}{[j(j+1)]^2} \quad (8)$$

where the $j_Q^{(K)}$ are spherical tensor operators.[45]

Note that the definitions in eqs 5–8 are generalized as compared with that in ref 45 by allowing complex values of the parameters A_{KQ}.

2.1.2. Dissociation Wave Function Expansion

The dissociation wave function $\Psi^{-(\hat{\mathbf{k}};\bar{n})}(\mathbf{R}, \mathbf{r}, E)$ in eq 1 is, in general, a complicated function of the coordinates R, $\mathbf{r}$, and the vectors $\hat{\mathbf{k}}$, $\mathbf{R}/R$. The dissociation wave function can be expanded for all recoil distances R over a set of orthogonal wave functions. This set can be presented as a product of a nuclear angular part which depends on two vectors $\hat{\mathbf{k}}$ and $\mathbf{R}/R$ and an electronic part which depends on all electron coordinates. The angular-dependent part is usually built of spherical harmonics[50–52] or Wigner D-functions.[51] The electronic part is widely adopted as a product of free-fragment *body*−frame wave functions $\Psi_{j,\Omega}^{el}(\mathbf{r})$ which are the eigenfunctions of the noninteracting internal part of the molecular Hamiltonian $H = H_{\text{int}}(\mathbf{r})$ (here $\mathbf{r}$ stands for all electronic coordinates and Ω is a component of the electronic angular momentum $\mathbf{j}$ about the recoil axis.) The orthogonal wave functions $\Psi_{j,\Omega}^{el}(\mathbf{r})$ do not depend on the internuclear separation R and form the *diabatic* basis.[51]

Another possible form of the electronic part is the *adiabatic* basis set built from the electronic molecular wave functions $\Psi_{n,\Omega}^{el}(\mathbf{r}, R) \equiv |n, \Omega\rangle$. These are the eigenfunctions of the full internal electronic molecular Hamiltonian $H = H_{\text{int}}(\mathbf{r}) + V(\mathbf{r}, R)$ (where $V(\mathbf{r}, R)$ is the interaction term including the spin−orbit interaction and n is a dissociation channel number.) For an axially symmetric parent molecule, $\Omega = \Omega_A + \Omega_B$, with Ω_A and Ω_B, the components of the electronic angular momenta of the fragments. The advantage of the *adiabatic* representation of the molecular electronic wave function is that, in the absence of nonadiabatic interactions, the quantum numbers n, Ω are preserved during dissociation.[51]

A convenient expansion of the dissociation wave function $\Psi^{-(\hat{\mathbf{k}},jm)}(\mathbf{R}, \mathbf{r}, E)$ is the adiabatic basis which was used in refs 26, 42, and 44. It can be written as

$$\Psi^{-(\hat{\mathbf{k}},jm)}(\mathbf{R}, \mathbf{r}, E) = \frac{1}{R}\sum_{JM}\sum_{\bar{n},n}\sum_{\Omega_R,\Omega}\frac{2J+1}{4\pi}(-1)^{i(\pi/2)J} \times \langle n\Omega|j\Omega\rangle D_{m\Omega}^{J*}(\phi, \theta, 0)D_{M\Omega}^{J}(\phi, \theta, 0) \times D_{M\Omega_R}^{J*}(\phi_R, \theta_R, 0)|\bar{n}\Omega_R\rangle \chi_{\bar{n}\Omega_R;n\Omega}^{J}(R) \quad (9)$$

where J is the total angular momentum of the molecule and M is its space-fixed z-component.

The body-fixed components of the total angular momentum $\mathbf{J}$ onto the recoil direction $\mathbf{k}$ and the $\mathbf{R}$-direction are denoted in eq 9 as Ω and Ω_R, respectively. The indices n and $\bar{n}$ in eq 9 are dissociation channel numbers and $\langle n\Omega|j\Omega\rangle$ are the expansion coefficients of the adiabatic molecular wave function over the free fragment wave functions in the asymptotic region.[44] The scattering function $\chi_{\bar{n}\Omega_R;n\Omega}^{J}(R)$ in eq 9 is the solution of the body-frame scattering equation.[44,51–53]

Note that because parity is not explicitly included in the expansion for the total excited-state wave function $\Psi^{-(\hat{\mathbf{k}},jm)}(\mathbf{R}, \mathbf{r}, E)$ in eq 9, these expansions are not the "proper" molecular wave functions. As these issues often lead to misunderstandings, we should clarify this point. Formally speaking, the total excited-state wave function $\Psi^{-(\hat{\mathbf{k}},jm)}(\mathbf{R}, \mathbf{r}, E)$ can be expanded in *any* set of orthogonal wave functions depending on the two vectors $\hat{\mathbf{k}}$ and $\mathbf{R}/R$ and on the electronic coordinates $\mathbf{r}$. The choice of a particular basis set is usually determined only by practical considerations. The expansion in eq 9 using the orthogonal set containing Wigner D-functions and the adiabatic electronic wave functions $|\bar{n}\Omega_R\rangle$ contains the quantum numbers $\bar{n}$ and Ω_R, which are conserved quantities in many basic photodissociation processes. It is therefore well-suited for solving the problems related to diatomic/linear molecules. For example, the quantum number $\bar{n}$ is preserved in adiabatic dissociation along a single potential curve, while the quantum number Ω_R is generally preserved in the absence of the Coriolis-type nonadiabatic interactions. The dynamical functions in eq 13, embodying the detailed dissociation dynamics, can thus generally be analyzed analytically without reference to the full close coupling equations,[8,21,26,42–44,54–57] and the incorporation of parity is not necessary. However, it may be very convenient for clarifying the problems where it plays a crucial role: for example, for examination of its impact on the angular momentum polarization of the products of photolysis of polyatomic molecules. These problems are not discussed in detail in the current review, and therefore the expansion in eq 9 is used where the parity is not incorporated.

2.1.3. Photofragment State Multipole Angular Distribution: Axial Recoil and Quasiclassical Approximations

Using eqs 1–4 and 9 and carrying out cumbersome angular momentum algebra transformations, the general expression for the angle−recoil distribution of the state multipoles $\rho_{KQ}^{j_A}$ can be presented in the form given in eq 9 of the Kuznetsov and Vasyutinskii paper.[44] Similar expressions have been reported by Roncero et al.[38] and by Mo and Suzuki[43] who used the diabatic representation for the molecular electronic wave function. These expressions are still fully quantum in nature, relying only on the assumption of an electric dipole transition; they can in principle be used for any type of photodissociation process. However it is difficult to use them

for analysis of the experimental data because of the complexity of their structure.

A significant simplification of the structure of the expressions can be achieved by isolating kinematical and dynamical terms within certain approximations. In particular, the axial recoil approximation has been used by Siebbeles et al.[8] for describing fast photodissociation and generalized by Bracker et al.[42] and by Balint−Kurti et al.[26] to the case of two open-shell photofragments. Within this approximation, the scattering wave function $\chi^{J}_{\bar{n}\Omega_R;\, n\Omega}(R)$ does not depend on J and summation over the indices J, J' can be carried out giving the expression for the fragment-state multipole, where the kinematical and dynamical terms are completely separated.[26]

Another approach, using the quasiclassical approximation in the high-J limit has been used by Kuznetsov and Vasyutinskii.[44] The quasiclassical approximation is based on the separation of the regions of the internuclear distance R, where the dissociation dynamics is mostly adiabatic, from the relatively narrow nonadiabatic interaction regions just as it is done for atomic collisions.[51] In that case, the scattering functions $\chi^{J}_{\bar{n}\Omega_R;n\Omega}(R)$ in eq 9 can be factored as:

$$\chi^{J}_{\bar{n}\Omega_R;n\Omega}(R) \approx e^{-i\delta^{J}_{n\Omega}}\tilde{\chi}^{J}_{\bar{n}\Omega_R;n\Omega}(R) \qquad (10)$$

where the elastic scattering phase factor, $e^{-i\delta^{J}_{n\Omega}}$, is a fast oscillating function of J, while the wave function $\tilde{\chi}^{J}_{\bar{n}\Omega_R;\, n\Omega}(R)$ does not depend on J within the interval $J_i - 1 \le J \le J_i + 1$.

Within the quasiclassical approach, the axial recoil approximation can be overcome by introduction of a classical angle of rotation of the molecular axis during dissociation γ. The final expression for the photofragment state multipoles can then be presented as[44]

$$\rho_{KQ}(\theta,\phi) = \frac{3}{4\pi}\left(\frac{2K+1}{2j_A+1}\right)^{1/2}\sum_{q,q',Q'}\sum_{k_d,q_d}(-1)^{K+q'}(2k_d+1)^{1/2}E_{k_dq_d}(\mathbf{e})\times \begin{pmatrix}1 & 1 & k_d\\ q' & -q & -Q'\end{pmatrix}\frac{f_K(q,q')}{f_0(0,0)+2f_0(1,1)}\times D^{K*}_{QQ'}(\phi,\theta,0)D^{k_d}_{q_dQ'}(\phi,\theta,0)d^{k_d}_{Q'Q'}(\gamma) \qquad (11)$$

where $Q' = q' - q$ and the indices q, q' denote the spherical basis[45] for the components of the molecular electronic transition moment, d_q, with respect to the molecular frame.

Equation 11 assumes that no Coriolis-type nonadiabatic interactions occur during dissociation, which is equivalent to the condition of *helicity conservation*, $\Omega = \Omega_R$. The generalization of eq 11 to the case when the Coriolis interaction is not small and can be found in refs 44 and 186.

The product of the two D-functions in eq 11 completely describes the state multipole recoil distribution in the laboratory frame, while the dynamical functions $f_K(q, q')$ contain all information about the photodissociation dynamics. The term $E_{k_dq_d}(\mathbf{e})$ in eq 11 is the irreducible polarization matrix of the incident light[45,48]

$$E_{k_dq_d}(\mathbf{e}) = [\mathbf{e}\otimes\mathbf{e}^*]_{k_dq_d} = \sum_{p,p'}e^*_p e_{p'}(-1)^{p'}\sqrt{2k_d+1}\begin{pmatrix}1 & 1 & k_d\\ p & -p' & q_d\end{pmatrix} \qquad (12)$$

with rank k_d and its projection q_d, where the rank k_d is limited to the values $k_d = 0,\ 1,\ 2$. The values of the matrices $E^k_q = [E_{kq}(\mathbf{e})]^*$ for different particular light polarizations are tabulated by Kummel and co-workers.[58] Convenient expressions for the polarization matrices $\Phi^k_q(\mathbf{e}) = (-1)^q(2k+1)^{-1/2}E_{kq}(\mathbf{e})$ and $\Phi_{kq}(\mathbf{e}) = (-1)^{k+1}E_{kq}(\mathbf{e})$ as function of the direction of the polarization vector $\mathbf{e}$ were given by Alexandrov and co-workers[59] and by Kupriyanov and Vasyutinskii,[60] respectively.

The Wigner d-functions $d^{k_d}_{Q'Q'}(\gamma)$ in eq 11 are *rotational factors* that describe the contribution from the rotation of the molecular axis to the photofragment and angular momentum distributions. If no rotation occurs ($\gamma = 0$), all rotational factors are equal to unity, $d^{k_d}_{Q'Q'}(0) = 1$, and eq 11 becomes equivalent to the corresponding expression obtained in the axial recoil approximation.[26,42]

Note that the γ-dependent *rotational factors* in eq 11 describe the rotation of the molecule resulting from the angular momentum $J \simeq J_i$, which is the only source of axis rotation when bending motion during photodissociation is not important. However, for practically important triatomic molecules, the main source of axis rotation during photodissociation is bending motion.[61] This second source of axis rotation is not included in the rotation factors in eq 11, and the corresponding rotation-dependent terms cannot in general be isolated from the dynamical functions. In this case, the expression for the photofragment state multipoles still can be written in the form in eq 11, where the dynamical functions depend on the bending dynamics.[62]

Summation over the total excited-state angular momenta J and J' including the coherent terms $J \neq J'$ has been performed in eq 11. This procedure in fact implies the formation of the *photofragment wave packet* in the molecular excited state. Therefore, eq 11 describes fast photodissociation of a rotating molecule from a certain initial state J_i when the rotational structure in the absorption spectrum is not resolved. It can also be shown that in the axial recoil approximation ($\gamma = 0$) eq 11 is valid not only in the high-J limit but for any integer or half-integer value of J_i.

2.1.4. Dynamical Functions

The dynamical functions $f_K(q, q')$ in eq 11 contain all information about the photodissociation dynamics. In case of the *adiabatic* representation of the electronic molecular wave functions, the dynamical functions can be written as

$$f_K(q,q') = \sum(-1)^{K+j_A+\Omega'_A}\begin{pmatrix}j_A & j_A & K\\ -\Omega_A & \Omega'_A & q-q'\end{pmatrix}\times (\mathscr{T}^{n\Omega}_{j_A\Omega_A j_B\Omega_B})^*\mathscr{T}^{n'\Omega'}_{j_A\Omega'_A j_B\Omega_B}(-1)^{2J_i}W(v_i,J_i)\times \langle\Psi^-_{n,\Omega}(R,\mathbf{r},E)|\hat{\mathbf{d}}_q|\Psi^{J_i}_{v_i\Omega_i}\rangle^*\langle\Psi^-_{n',\Omega'}(R,\mathbf{r},E)|\hat{\mathbf{d}}_{q'}|\Psi^{J_i}_{v_i\Omega_i}\rangle \qquad (13)$$

where the body-frame dissociative wave function

$$\Psi^-_{n,\Omega}(R,\mathbf{r},E) = \frac{1}{R}\sum_{\bar{n}}\chi^{J_i}_{n\Omega;\bar{n}\Omega}(R)\Psi^{el}_{\bar{n},\Omega}(\mathbf{r},R) \qquad (14)$$

is the product of the adiabatic electronic wave function and the scattering wave function in the outgoing channel n, Ω, and

$$\Psi^{J_i}_{v_i\Omega_i} = \chi^{J_i}_{v_i\Omega_i}(R)\Psi^{el}_{\Omega_i}(\mathbf{r},R) \qquad (15)$$

is the body-frame wave function of the initial state which is assumed to be bound, where v_i is a vibrational quantum number.

The following selection rule holds in general in eq 13: $q' - q = \Omega' - \Omega = \Omega'_A - \Omega_A$. The summation in eq 11 is

taken over all repeated indices: n, n', Ω, Ω', Ω_A, Ω'_A, j_B, Ω_B, Ω_i, J_i, v_i. The averaging over the initial state is performed in eq 13, where $W(v_i, J_i)$ is the population distribution over the initial ro-vibrational states of the parent molecule.

The matrix elements $\langle \Psi^-_{n,\Omega}(R, \mathbf{r}, E)|\hat{\mathbf{d}}_q|\Psi_{\Omega_i}\rangle$ in eqs 13 are the photofragmentation **T** matrix elements.[35,37] In general, the **T** matrix elements can be computed using the close-coupling[52] or wavepacket[63–65] formalism. The indices q, q' in eq 13 can take only the values 0 or ±1, corresponding to parallel or perpendicular electronic transitions, respectively. The diagonal elements of the dynamical functions $f_K(q, q')$ with $q = q'$ correspond to incoherent excitation of parallel or perpendicular transitions, while the off-diagonal elements with $q \neq q'$ correspond to coherent excitation of different molecular continua.

The photofragmentation **T** matrix elements can always be presented in the following simple form[26]

$$\langle \Psi^-_{n,\Omega}(R, \mathbf{r}, E)|\hat{\mathbf{d}}_q|\Psi_{\Omega_i}\rangle = r_{n,\Omega}e^{i\varphi_{n,\Omega}} \tag{16}$$

where the index n has clear physical meaning, indicating different possible dissociation channels resulting in the photofragment pairs $A(j_A) + B(j_B)$. The value $r_{n,\Omega}$ in eq 16 is the modulus of the corresponding photofragmentation **T** matrix, and $\varphi_{n,\Omega}$ is a phase shift.

Equation 16 suggests a general way of interpretation of the values of the dynamical functions/anisotropy parameters in terms of the amplitudes of the **T** matrix elements related to different dissociation channels, and the quantum mechanical phase shifts between these channels. For example, if only one of the states $|n\rangle$ can be optically excited from the initial state $|i\rangle$, all values $r^2_{n'}$ with $n' \neq n$ can be interpreted as probabilities of nonadiabatic transitions between the state n, and all others and can be directly measured in experiment, including the states having the same asymptotic energy limit.[26]

The phase difference $\varphi_{n,\Omega} - \varphi_{n'\Omega'}$ appears in the expression for the dynamical function 13 for the case of coherent excitation mechanism and it can also be determined from experiment.[27] The possibility of direct determination of all nonadiabatic probabilities and the phase shifts between different dissociation channels from experimental data is new in the field of molecular photodissociation and reaction dynamics. The coherent excitation mechanism has recently become a subject of intensive studies.[25,26,42,66,67]

The dynamical functions obey the following symmetry relations[60]

$$f_K(q, q') = (-1)^K f_K(-q, -q') = (-1)^{q-q'} f^*_K(q', q) \tag{17}$$

The components of the total angular momentum onto the molecular axis Ω_i and Ω_R in eq 13 obey the selection rule $\Omega_R = \Omega_i + q$.[68] If more than one molecular ground state $|\Psi^{J_i}_{\Omega_i}\rangle$ is initially populated, the corresponding weighting term $N_{J_i\Omega_i}$ should be added to eq 13.

2.1.5. Long-Range Coefficients $\mathcal{T}$

The coefficients $\mathcal{T}^{n\Omega}_{j_A\Omega_A j_B\Omega_B}$ in eq 13 are expansion coefficients of the adiabatic molecular electronic states over the fragment basis $|j_A\Omega_A\rangle|j_B\Omega_B\rangle$ in the asymptotic region[20,69]

$$\Psi^{el}_{n,\Omega}(\mathbf{r}, R) \xrightarrow{R\to\infty} \sum_{\Omega_A,\Omega_B} \mathcal{T}^{n\Omega}_{j_A\Omega_A j_B\Omega_B}|j_A\Omega_A\rangle|j_B\Omega_B\rangle \tag{18}$$

The expansion coefficients $\mathcal{T}^{n\Omega}_{j_A\Omega_A j_B\Omega_B}$ can be calculated with standard time-independent perturbation theory using $H_{\text{int}}(\mathbf{r})$ as an unperturbed electronic Hamiltonian of the atoms A and B and taking the perturbation term $V(\mathbf{r}, R)$ in the form of the long-range interatomic interaction.

If $\Omega = 0$, the coefficients $\mathcal{T}^{n\Omega}_{j_A\Omega_A j_B\Omega_B}$ can in general be presented as a sum of Clebsch−Gordan coefficients

$$\mathcal{T}^{n0}_{j_A\Omega_A j_B\Omega_B} = \sum_j c(j) C^{j0}_{j_A\Omega_A j_B\Omega_B} \tag{19}$$

where the indices j must be either all even or all odd, and $c(j)$ are expansion coefficients. In this case the molecular wave functions $\Psi^{el}_{n,0}(\mathbf{r}, R)$ have symmetry under reflection of all electron coordinates in the plane containing the recoil axis described by the reflection index $\sigma_v = \pm 1$. As can be shown from eqs 18 and 19, the reflection index is given by $\sigma_v = p_A p_B(-1)^j$, where p_A and p_B are the parities of the corresponding fragment states.

If $\Omega \neq 0$, then the coefficients $\mathcal{T}^{n\Omega}_{j_A\Omega_A j_B\Omega_B}$ cannot be presented as a sum of Clebsch−Gordan coefficients. In this case, the molecular wave functions $\Psi^{el}_{n,\Omega}(\mathbf{r}, R)$ have no symmetry under reflection of all electron coordinates in the plane containing the recoil axis. Instead, they transform under the reflection $\hat{\sigma}_v$ as $\hat{\sigma}_v\Psi^{el}_{n,\Omega}(\mathbf{r}, R) \to \omega\Psi^{el}_{n,-\Omega}(\mathbf{r}, R)$, where the coefficient ω is in general undefined and can be either 1 or −1. Following the choice made in ref 69, we assume that the wave functions $\Psi^{el}_{n,\Omega}(\mathbf{r}, R)$ with $\Omega \neq 0$ transform under reflection in the same way as the product of the atomic wave functions in the right side of eq 18, which results in the following symmetry rule for the expansion coefficients $\mathcal{T}^{n\Omega}_{j_A\Omega_A j_B\Omega_B}$ ($\Omega \neq 0$).

$$\mathcal{T}^{n-\Omega}_{j_A-\Omega_A j_B-\Omega_B} = \mathcal{T}^{n\Omega}_{j_A\Omega_A j_B\Omega_B} \tag{20}$$

The coefficients $\langle j\Omega|n\Omega\rangle$ in eq 9 relate to the coefficients $\mathcal{T}^{n\Omega}_{j_A\Omega_A j_B\Omega_B}$ in eq 18 as

$$\langle j\Omega|n\Omega\rangle = \sum_{\Omega_A\Omega_B} \mathrm{C}^{j\Omega}_{j_A\Omega_A j_B\Omega_B}\mathcal{T}^{n\Omega}_{j_A\Omega_A j_B\Omega_B} \tag{21}$$

Particular values of the coefficients $\mathcal{T}^{n\Omega_k}_{j_A\Omega_A j_B\Omega_B}$ corresponding to different types of the long-range interactions between two open-shell atoms are tabulated in Tables 1 and 2 below.

Table 1 presents the energy levels and the asymptotic molecular wave functions for twelve low-lying molecular states of an HX molecule (where X is a halogen atom), correlating adiabatically at large internuclear distance with two spin−orbit energy states: $H(^2S_{1/2}) + X(^2P_{3/2})$ and $H(^2S_{1/2}) + X(^2P_{1/2})$ pairs of atoms. The major contribution to the long-range interaction for both states is the van der Waals interaction, resulting in a $-C/R^6$ energy dependence, where C is a constant.[70] According to the Hund's case c classification, we denote the molecular wave functions as $|n, \Omega^\sigma\rangle$, where $\sigma = \pm$ is a reflection character for the $\Omega = 0$ energy substates and $n = \alpha$, β, or γ is an index labeling the different substates with the same $|\Omega|$ quantum number in order of increasing energy.

The $\mathcal{T}^{n\Omega}_{j_A\Omega_A j_B\Omega_B}$ matrix elements are the expansion coefficients in the third column in Table 1. As mentioned above, these expansion coefficients have been calculated within the standard time-independent perturbation theory. Note that the lines 3, 5, and 8 in Table 1, where $n = \gamma, \beta$, and α, respectively, contain only one expansion term each, which means that one of the two possible $\mathcal{T}^{n1}_{j_A\Omega_A j_B\Omega_B}$ matrix elements is equal to

Table 1. Energy Levels and Molecular Wave Functions for Van der Waals Interatomic Interaction[26]

energy	molecular state	expansion of the wave function $\|n, \Omega^{\sigma}\rangle$ over the atomic states $\|j_A\sigma_A;j_B\sigma_B\rangle$
	$\|\beta, 0^+\rangle$	$\frac{1}{\sqrt{2}}\left(\left\|\frac{1}{2}\frac{1}{2};\frac{1}{2}-\frac{1}{2}\right\rangle+\left\|\frac{1}{2}-\frac{1}{2};\frac{1}{2}\frac{1}{2}\right\rangle\right)$
$\Delta_{so}-\frac{1}{\sqrt{3}R^6}\varepsilon(0,0)$	$\|\beta, 0^-\rangle$	$\frac{1}{\sqrt{2}}\left(\left\|\frac{1}{2}\frac{1}{2};\frac{1}{2}-\frac{1}{2}\right\rangle-\left\|\frac{1}{2}-\frac{1}{2};\frac{1}{2}\frac{1}{2}\right\rangle\right)$
	$\|\gamma, 1\rangle$	$\left\|\frac{1}{2}\frac{1}{2};\frac{1}{2}\frac{1}{2}\right\rangle$
	$\|2\rangle$	$\left\|\frac{1}{2}\frac{1}{2};\frac{3}{2}\frac{3}{2}\right\rangle$
$-\frac{1}{\sqrt{3}R^6}\left[\varepsilon(0,0)-\frac{\varepsilon(0,2)}{2\sqrt{5}}\right]$	$\|\beta, 1\rangle$	$\left\|\frac{1}{2}-\frac{1}{2};\frac{3}{2}\frac{3}{2}\right\rangle$
	$\|\alpha, 0^+\rangle$	$\frac{1}{\sqrt{2}}\left(\left\|\frac{1}{2}\frac{1}{2};\frac{3}{2}-\frac{1}{2}\right\rangle-\left\|\frac{1}{2}-\frac{1}{2};\frac{3}{2}\frac{1}{2}\right\rangle\right)$
$-\frac{1}{\sqrt{3}R^6}\left[\varepsilon(0,0)+\frac{\varepsilon(0,2)}{2\sqrt{5}}\right]$	$\|\alpha, 0^-\rangle$	$\frac{1}{\sqrt{2}}\left(\left\|\frac{1}{2}\frac{1}{2};\frac{3}{2}-\frac{1}{2}\right\rangle+\left\|\frac{1}{2}-\frac{1}{2};\frac{3}{2}\frac{1}{2}\right\rangle\right)$
	$\|\alpha, 1\rangle$	$\left\|\frac{1}{2}\frac{1}{2};\frac{3}{2}\frac{1}{2}\right\rangle$

Table 2. Energy Levels and Molecular Wave Functions for Quadrupole−quadrupole Interatomic Interaction[60]

energy	molecular state	expansion of the molecular wave function $\|n, \Omega^{\sigma}\rangle$ over the atomic states $\|j_A\Omega_A;j_B\Omega_B\rangle$
$\frac{2}{5}U(R)$	$\|B, 0^+\rangle$	$\frac{1}{2}\left(\left\|\frac{3}{2}\frac{3}{2};\frac{3}{2}-\frac{3}{2}\right\rangle+\left\|\frac{3}{2}\frac{1}{2};\frac{3}{2}-\frac{1}{2}\right\rangle-\left\|\frac{3}{2}-\frac{3}{2};\frac{3}{2}\frac{3}{2}\right\rangle-\left\|\frac{3}{2}-\frac{1}{2};\frac{3}{2}\frac{1}{2}\right\rangle\right)$
$\frac{1}{5}U(R)$	$\|C, 1\rangle$	$\left\|\frac{3}{2}\frac{1}{2};\frac{3}{2}\frac{1}{2}\right\rangle$
0	$\|X, 0^+\rangle$	$\frac{1}{2}\left(\left\|\frac{3}{2}\frac{3}{2};\frac{3}{2}-\frac{3}{2}\right\rangle-\left\|\frac{3}{2}\frac{1}{2};\frac{3}{2}-\frac{1}{2}\right\rangle-\left\|\frac{3}{2}-\frac{3}{2};\frac{3}{2}\frac{3}{2}\right\rangle+\left\|\frac{3}{2}-\frac{1}{2};\frac{3}{2}\frac{1}{2}\right\rangle\right)$
$-\frac{2}{15}U(R)$	$\|A, 1\rangle$	$\frac{1}{\sqrt{2}}\left(\left\|\frac{3}{2}\frac{3}{2};\frac{3}{2}-\frac{1}{2}\right\rangle+\left\|\frac{3}{2}-\frac{1}{2};\frac{3}{2}\frac{3}{2}\right\rangle\right)$
$-\frac{4}{15}U(R)$	$\|D, 1\rangle$	$\frac{1}{\sqrt{2}}\left(\left\|\frac{3}{2}\frac{3}{2};\frac{3}{2}-\frac{1}{2}\right\rangle-\left\|\frac{3}{2}-\frac{1}{2};\frac{3}{2}\frac{3}{2}\right\rangle\right)$

unity and the other is equal to zero. These values are approximate ones: the exact form of expansion in all these cases can be written in the form: $|n, 1\rangle = c_1|j_A\Omega_A;\ j_B\Omega_B\rangle + c_2|j_A\Omega'_A; j_B\Omega_B\rangle$, where $|c_1| \gg |c_2|$ and $\Omega_A + \Omega_B = \Omega'_A + \Omega_B = 1$. The value Δ_{so} in the first column of Table 1 is the spin−orbit energy splitting in the halogen atom, and the values $\varepsilon(0, 0)$ and $\varepsilon(0, 2)$ are defined in the Nikitin and Umansky monograph.[51]

Table 2 presents long-range energy states and molecular wave functions for ten low-lying states of a heteronuclear halogen molecule *XY* correlating adiabatically at large internuclear distance with a pair of ground-state halogen atoms $X(^2P_{3/2}) + Y(^2P_{3/2})$. The major contribution to the long-range interaction for this case is the quadrupole−quadrupole interaction, which is proportional to $1/R^5$. Only the molecular

states that can contribute to the photodissociation process are shown in the table. These are three $\Omega = 1$ states and two $\Omega = 0^+$ states. The function $U(R)$ in Table 2 is as follows

$$U(R) = \frac{1}{R^5}\langle L_1||Q_X^2||L_1\rangle \langle L_2||Q_Y^2||L_2\rangle \qquad (22)$$

where $\langle L_1||Q_X^2||L_1\rangle$ and $\langle L_2||Q_Y^2||L_2\rangle$ are reduced matrix elements of the quadrupole momentum operators for X and Y atoms, respectively and $L_X = 1$, $L_Y = 1$ are the corresponding orbital momenta. The matrices $\mathcal{T}^{n\Omega}_{j_A\Omega_A j_B\Omega_B}$ are the expansion coefficients in the third column in Table 2.

Note that the order of the molecular energy states in Table 2 is opposite to that presented in Table 1 of ref 60. The reason is that Table 1 in ref 60 represents the case of opposite signs of the photofragment quadrupole momenta (TlBr molecule), resulting in the *negative* value of the function $U(R)$. However, for an interhalogen molecule case considered in Table 2, the photofragments have the same sign of their quadrupole momenta, resulting in the *positive* value of the function $U(R)$.

For a homonuclear halogen molecule X_2, the values of the matrices $\mathcal{T}^{n\Omega}_{j_A\Omega_A j_B\Omega_B}$ still can be taken from Table 2; however the number of states which can be involved in photolysis reaction decreases because the ground-state molecule $X^1\Sigma_g$ which is of *gerade* symmetry can optically interact only with *underade* states.[70] These are the $|A, 1\rangle$ and $|C, 1\rangle$ states in Table 2. The effect of long-range interaction in ICl on the photofragment angular momentum polarization has been theoretically investigated by Alexander and Rakitzis.[187] The long-range coefficients $\mathcal{T}$ for many particular values of the angular momenta j_A and j_B under condition of the quadrupole–quadrupole interatomic interaction have been tabulated by Alexander.[188] Detailed description of long-range interactions and correlation diagrams for halogen molecules can be found in refs 71 and 72.

2.1.6. Rotational Factors

The rotation factors $d^{k_d}_{Q'Q'}(\gamma)$ in eq 11 depend on the rank of the dissociation photon polarization matrix k_d, on the index Q' describing coherent and incoherent excitation of the molecule, and on the classical angle of rotation of the molecular axis γ. The rotation factors describe the reduction of the photofragment anisotropy resulting from the rotation of the molecular recoil axis. All possible rotation factors in eq 11 are collected in Table 3 and plotted as a function of γ in Figure 1. The γ-dependence of each anisotropy parameter in Table 3 clarifies the mechanism of production of the fragment angular momentum polarization in a corresponding reaction channel, which is also described in more detail in section 2.1.7.

Table 3. All Possible Rotational Factors with Their Rank k_d = 0,..., 2 and Projections Q'

	$k_d = 0$	$k_d = 1$	$k_d = 2$
$Q' = 0$	1	$\cos\gamma$	$P_2(\cos\gamma)$
$Q' = 1$		$\frac{1+\cos\gamma}{2}$	$\frac{2\cos^2\gamma+\cos\gamma-1}{2}$
$Q' = 2$			$\frac{(1+\cos\gamma)^2}{4}$

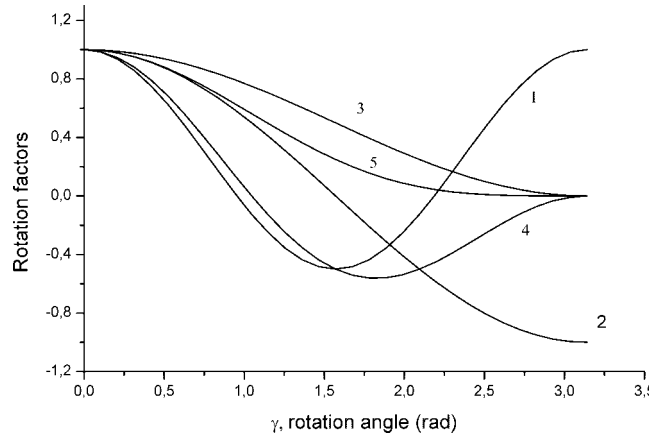

Figure 1. Rotation factors $d^{k_d}_{Q'Q'}(\gamma)$ as function of the classical rotation angle γ: (1) $d^2_{00}(\gamma) = P_2(\cos\gamma)$; (2) $d^1_{00}(\gamma) = \cos\gamma$; (3) $d^1_{11}(\gamma) = (1 + \cos\gamma)/2$; (4) $d^2_{11}(\gamma) = (2\cos^2\gamma + \cos\gamma - 1)/2$; (5) $d^2_{22}(\gamma) = [(1 + \cos\gamma)^2]/4$.

The rotational factor $P_2(\cos\gamma)$ with the indices values $k_d = 2$, $Q' = 0$ describes the decrease of the parameter β because of the rotation of the molecular axis. The rotational factors with the rank $k_d = 1$ relate to the multipole angular momentum polarization resulting from the incident photon *helicity*. These dissociation mechanisms can be initiated only with circularly polarized light. The rotational factors with the rank $k_d = 2$ relate to the multipole angular momentum polarization arising from *alignment* of the light polarization vector **e**. These dissociation mechanisms can be induced by any light polarization.

The rotational factors with the $Q' = 0$ value are related to the incoherent excitation of a single excited molecular state and those with the $Q' = 1$ value are related to the coherent excitation of a parallel and a perpendicular transition. Finally, the rotational factors with the $Q' = 2$ value are related to the coherent excitation of two perpendicular transitions. The negative values of the index Q'' are not shown in Table 3 because the corresponding rotation factors can be found from the relationship $d^{k_d}_{-Q'-Q'}(\gamma) = d^{k_d}_{Q'Q'}(\gamma)$.[47]

2.1.7. Multipole Angular Distributions: Laboratory Frame

Using eq 11, one can obtain expressions for the specific differential photofragment state multipoles of certain ranks and experimental geometries. Normalized combinations of the dynamical functions in eq 11, *anisotropy parameters*, have been defined that contain all information about the dissociation dynamics and that can be directly determined from experiment.[33] We now consider different particular cases.

For $K = Q = 0$, eq 11 describes the angular distributions of the photofragment population $N(\theta, \phi) = (2j_A + 1)^{1/2}\rho_{00}(\theta, \phi)$. If the light is linearly polarized where Θ is the angle between the light polarization vector **e** and the recoil vector **k**, eq 11 results in the following well-known expression:[45,73]

$$N(\Theta) = \frac{1}{4\pi}[1 + \beta P_2(\cos\Theta)], \qquad (23)$$

which depends on the anisotropy parameter β. In our general treatment, β can be treated as a *zeroth-rank* anisotropy parameter.

The anisotropy parameter β in eq 23 can be written as

$$\beta = 2P_2(\cos\gamma)P_2(\cos\gamma^{(0)}) \tag{24}$$

where $P_2(\cos\gamma)$ is the second order Legendre polynomial describing the rotation of the recoil axis around the total angular momentum vector $\mathbf{J}_i$ and $P_2(\cos\gamma^{(0)})$ is the Legendre polynomial characterizing the internal molecular anisotropy. For a diatomic molecule, $\gamma^{(0)}$ in eq 24 is the angle between the initial direction of the molecular axis and the transition dipole moment μ, which can be written in terms of zeroth-order dynamical functions[44]

$$\cos^2\gamma^{(0)} = \frac{f_0(0,0)}{f_0(0,0)+2f_0(1,1)} = \frac{I_{||}}{I_{||}+I_{\perp}} \tag{25}$$

where $I_{||} = f_0(0,0)$ and $I_{||} = 2f_0(1,1)$ are the intensities of the parallel and perpendicular transitions, respectively. The last term in eq 24 can be written in the form

$$P_2(\cos\gamma^{(0)}) = \frac{\beta^{(0)}}{2} = \frac{f_0(0,0)-f_0(1,\ 1)}{f_0(0,0)+2f_0(1,1)} \tag{26}$$

where $\beta^{(0)}$ is the anisotropy parameter obtained in the axial recoil approximation.[8]

If a triatomic molecule is optically excited via a parallel $A' \leftarrow A'$ transition, a useful expression for the parameter β can be obtained for the important case when the molecule undergoes strong bending motion by an angle χ. In this case, the parameter β can still be be written in the form in eq 24 where the angle $\gamma^{(0)}$ is replaced by the angle χ. Equations 24 and 25, obtained on the basis of the full quantum mechanical approach,[44,62] are in perfect agreement with the results obtained by classical and semiclassical methods.[61,74–76]

For a $A'' \leftarrow A'$ transition in a bending triatomic molecule, when the transition dipole moment is perpendicular to the molecular plane, the parameter β does not depend on the bending angle χ and is always given by $\beta = -P_2(\cos\gamma)$.

As shown in eqs 5–8, all rank $K > 0$ state multipoles describe the angular distributions of the photofragment angular momenta. In general, they can be defined either in the laboratory or in the body frame. In this section, we consider the laboratory frame set of the anisotropy parameters of the rank $K = 1-4$.

The anisotropy parameters are important because they are phenomenological coefficients representing different kinematical (recoil-angle dependent) components of the state multipoles in eq 13. Within first-order time-dependent perturbation theory, these kinematical components have the same universal form for *any* photodissociation process, including photodissociation of any diatomic or polyatomic molecule, and for any photodissociation mechanism.[186] These anisotropy parameters are quantum mechanical variables which can be isolated from each other and determined from experimental data in any photolysis reaction, without any assumptions concerning the photolysis mechanism. However, the interpretation of these parameters and the underlying dynamical functions will depend on the particular photolysis mechanism.

It is convenient to define the odd rank, $K = 1, 3$, anisotropy parameters as follows:

$$\alpha_K = \alpha_K^{(0)} d^1_{00}(\gamma), \quad \alpha_K^{(0)} = V_K^{-1}(j)\frac{f_K(1,1)}{f_0(0,0)+2f_0(1,1)}$$

$$\gamma_K = \gamma_K^{(0)} d^1_{11}(\gamma), \quad \gamma_K^{(0)} = V_K^{-1}(j)\frac{2\,Re[f_K(1,0)]}{f_0(0,0)+2f_0(1,1)}$$

$$\gamma'_K = \gamma_K^{(0)'} d^2_{11}(\gamma), \quad \gamma_K^{(0)'} = V_K^{-1}(j)\frac{2\,Im[f_K(1,0)]}{f_0(0,0)+2f_0(1,1)} \tag{27}$$

$$\eta_3 = \eta_3^{(0)} d^2_{22}(\gamma), \quad \eta_3^{(0)} = -\frac{\sqrt{5}}{2}V_3^{-1}(j)\frac{Im[f_3(1,-1)]}{f_0(0,0)+2f_0(1,1)}\delta_{K,3}$$

where $V_1(j) = 1$ and $V_3(j) = j(j+1)/[(j-1)(j+2)(2j-1)(2j+3)]^{1/2}$ and the d-functions are rotational factors.

Here $\alpha_K^{(0)}$, $\gamma_K^{(0)}$, $\gamma_K^{(0)'}$, and $n_3^{(0)}$, $K = 1, 3$ are the corresponding "axial recoil" anisotropy parameters. As shown in eq 27, there are three first-rank anisotropy parameters, α_1, γ_1, and γ'_1, and four third-rank anisotropy parameters, α_3, γ_3, γ'_3, and η_3. Each of them can, in general, be independent from the others.

These parameters have the following clear physical meaning: they represent contributions to photofragment orientation from different underlying dissociation mechanisms. Specifically, the parameter α_K represents contribution to the photofragment orientation from incoherent excitation ($q = q'$, $\Omega = \Omega'$) via a perpendicular ($\Delta\Omega = \pm 1$) transition [pure parallel excitation does not result in any fragment orientation in the absence of the Coriolis interaction],[69] while the parameter γ_K represents contribution from coherent excitation of a parallel ($\Delta\Omega = 0$) and a perpendicular ($\Delta\Omega = \pm 1$) transition. It is related to the *helicity* of the photolysis photons. The parameter γ'_K also describes the coherent excitation of a parallel and a perpendicular transition but of different type, which is related to the *alignment* of the photolysis photons. Finally, the parameter η_3 describes contribution from the coherent superposition of two perpendicular transitions, and its definition follows from the fact that the dynamical function $f_3(1,-1)$ is purely imaginary.

The ranges of these parameters are listed in Table 4; they were calculated assuming maximum possible orientation of the atomic fragment in the molecular frame. They do not depend on the specifics of the molecule (which can be either diatomic or polyatomic) and have the advantage that for any type of reaction the parameters cannot be outside the ranges.

The anisotropy parameters of the first rank are directly related to the mean value of the photofragment orientation. As can be shown by integration of the fragment $K = 1$ state, the multipole angular distribution in eq 11 over all recoil angles, parameters α_1 and γ_1 fulfill the condition

$$\alpha_1 + \gamma_1 = \langle A_{10}\rangle \tag{28}$$

Here, $\langle A_{10}\rangle$ is the **z** component of the photofragment orientation (5) in a reference frame with **z** parallel to the photolysis laser propagation direction averaged over the recoil angles. The contribution from the γ'_1 parameter, as well as the contribution from all $K = 3$ parameters, vanishes after averaging over all recoil angles.

The angular distributions of the state multipoles of the first rank, $\rho_{1Q}(\theta, \phi)$, for different dissociation geometries are tabulated in the earlier review paper.[21] The angular distribution of the state multipoles with $K = 1, 3$ and $Q = -K,..., K$ for the two most important experimental geometries can be written as one of the following:[77]

(1) The photolysis light is circularly polarized and propagates along the **z** axis

$$\rho_{KQ}(\theta,\phi)=\frac{3\sqrt{2K+1}V_K(j_A)e^{iQ\phi}}{4\pi\sqrt{2j_A+1}}\times \left\{\sigma\alpha_K d^K_{Q0}(\theta)\cos\theta+\frac{\sigma\gamma_K}{2\sqrt{2}}\sin\theta[d^K_{Q1}(\theta)-d^K_{Q-1}(\theta)]+ i\left[\frac{\gamma'_K}{2\sqrt{2}}\sin\theta\cos\theta[d^K_{Q1}(\theta)+d^K_{Q-1}(\theta)]- \frac{\eta_3\delta_{K,3}}{2\sqrt{5}}\sin^2\theta[d^K_{Q2}(\theta)-d^K_{Q-2}(\theta)]\right]\right\} \quad (29)$$

where θ and ϕ are polar angles that indicate the fragment recoil direction and the index σ is equal to $+1$ for right circularly polarized (CP) light and -1 for left CP light.

(2) The photolysis light is linearly polarized in the **xy** plane, 45° to the **x** axis, and propagates along the **z** axis

$$\rho_{KQ}(\theta,\phi)=\frac{3\sqrt{2K+1}V_K(j_A)e^{iQ\phi}}{4\pi\sqrt{2j_A+1}}\left\{\frac{\gamma'_K}{2\sqrt{2}}\sin\theta\times [-\cos 2\phi[d^K_{Q1}(\theta)-d^K_{Q-1}(\theta)]+i\cos\theta(\sin 2\phi+1)\times [d^K_{Q1}(\theta)+d^K_{Q-1}(\theta)]]-\frac{\eta_3\delta_{K,3}}{2\sqrt{5}}[i(\sin^2\theta-(1+\cos^2\theta)\sin 2\phi)[d^K_{Q2}(\theta)-d^K_{Q-2}(\theta)]+ 2\cos\theta\cos 2\phi[d^K_{Q2}(\theta)+d^K_{Q-2}(\theta)]]\right\} \quad (30)$$

It is seen from eq 29 that the $K = 1$ state multipole depends in general on three anisotropy parameters of the first rank, and the $K = 3$ state multipole depends on four third-rank anisotropy parameters. However, for the $Q = 0$ component that is usually detected in experiments, the third and fourth lines in eq 29 is equal to zero, and thus, only four of the anisotropy parameters, α_1, γ_1, α_3, and γ_3, can usually be determined. Therefore, the experimental geometries with circularly and linearly polarized photolysis light in eqs 29 and 30 are complementary to each other, and together they allow determination all odd-rank $K = 1$, 3 anisotropy parameters.

Both experimental geometries using circularly and linearly polarized photolysis light have widely been used for investigation of the angular momentum distribution of oriented $K = 1$ or 3 atomic photofragments (see refs 34, 57, 62, 77–81, and 189 and refs 25 and 82–84, respectively.)

The even-rank, $K = 2, 4$, anisotropy parameters are defined as

$$s_K=s_K^{(0)}=V_K(j_A)^{-1}\frac{f_K(0,0)+2f_K(1,1)}{f_0(0,0)+2f_0(1,1)} \quad (31)$$

$$\alpha_K=\alpha_K^{(0)}d^2_{00}(\gamma),\quad \alpha_K^{(0)}=V_K(j_A)^{-1}\frac{f_K(1,1)-f_K(0,0)}{f_0(0,0)+2f_0(1,1)}$$

$$\gamma_K=\gamma_K^{(0)}d^2_{11}(\gamma),\quad \gamma_K^{(0)}=2\sqrt{3}V_K(j_A)^{-1}\frac{Re[f_K(1,0)]}{f_0(0,0)+2f_0(1,1)}$$

$$\gamma'_K=\gamma_K^{(0)'}d^1_{11}(\gamma),\quad \gamma_K^{(0)'}=2\sqrt{3}V_K(j_A)^{-1}\frac{Im[f_K(1,0)]}{f_0(0,0)+2f_0(1,1)}$$

$$\eta_K=\eta_K^{(0)}d^2_{22}(\gamma),\quad \eta_K^{(0)}=\sqrt{6}V_K(j_A)^{-1}\frac{f_K(1,-1)}{f_0(0,0)+2f_0(1,1)}$$

where $V_2(j)=5\{j(j+1)/[(2j+3)(2j-1)]\}^{1/2}$ and $V_4(j)=9[j(j+1)]^{3/2}/[(j-1)(j+2)(2j-3)(2j-1)(2j+3)(2j+5)]^{1/2}$.

Here again, $\alpha_K^{(0)}$, $\gamma_K^{(0)'}$, $\gamma_K^{(0)}$, and $\eta_K^{(0)}$, $K = 2$, 4, are corresponding axial recoil anisotropy parameters. There are four rank $K = 2$ and four rank $K = 4$ anisotropy parameters which, in general, can all be independent from each other. The parameters α_K and s_K in eq 31 describe the total alignment caused by incoherent excitation ($q = q'$) via parallel and perpendicular transitions. As can be seen from eq 31, in the limit of a pure perpendicular transition, $2\alpha_K = s_K d^2_{00}(\gamma)$, while in the limit of a pure parallel transition, $\alpha_K = -s_K d^2_{00}(\gamma)$. The γ_K parameters describe the photofragment alignment produced via a coherent superposition of parallel and perpendicular excitation. These parameters are important when two excited electronic states with Ω equal to ±1 and 0 have comparable excitation probabilities. The η_K parameters arise from a coherent superposition of two perpendicular transitions. This may occur for two states separated in energy as in the parallel/perpendicular case or for simultaneous excitation of the degenerate $\Omega = \pm1$ "lambda doublet" components of an $|\Omega| = 1$ state because both states automatically have equal excitation probabilities. The ranges of all even-rank anisotropy parameters are listed in Tables 5 and 6.

Table 4. Physical Ranges of the Rank $K = 1$, 3 Anisotropy Parameters[a]

parameter	extrema
α_1	$\pm\frac{2-\beta}{6}\left[\frac{j}{j+1}\right]^{\frac{1}{2}}$
γ_1	$\pm\frac{2}{3}\left[\frac{j(1+\beta)(2-\beta)}{2(j+1)}\right]^{\frac{1}{2}}$
γ'_1	$\pm\frac{2}{3}\left[\frac{j(1+\beta)(2-\beta)}{2(j+1)}\right]^{\frac{1}{2}}$
α_3	$\pm\frac{(2-\beta)(j-1)(2j-1)}{6(j+1)\sqrt{j(j+1)}}C(j)$
γ_3	$\pm\frac{8(j-1)(2j-1)}{9\sqrt{5}(j+1)}\left[\frac{(1+\beta)(2-\beta)}{j(j+1)}\right]^{\frac{1}{2}}C(j)$
γ'_3	$\pm\frac{8(j-1)(2j-1)}{9\sqrt{5}(j+1)}\left[\frac{(1+\beta)(2-\beta)}{j(j+1)}\right]^{\frac{1}{2}}C(j)$
η_3	$\pm\frac{\sqrt{50}(2-\beta)(j-1)(2j-1)}{36(j+1)\sqrt{j(j+1)}}C(j)$

[a] The coefficient $C(j)$ is equal to $C(j) = (6 - j)/j$, if $j \le 3$ and $C(j) = 1$ if $j > 3$.

Table 5. Range of the Rank $K = 2$ Anisotropy Parameters

	range
α_2	$-\frac{2j+\beta(j-1)}{10(j+1)} \cdots \frac{2j+\beta}{10(j+1)}$ if j is an integer
	$-\frac{(2j-1)[2(2j+1)+\beta(2j-1)]}{40j(j+1)} \cdots \frac{(2j-1)(2j+\beta+1)}{20j(j+1)}$ if j is a half-integer
s_2	$-\frac{1}{5} \cdots \frac{2j-1}{5(j+1)}$ if j is an integer
	$-\frac{(2j-1)(2j+3)}{20j(j+1)} \cdots \frac{(2j-1)}{5(j+1)}$ if j is a half-integer
γ_2	$-\frac{1}{5}\left[\frac{(1+\beta)(2-\beta)}{2}\right]^{1/2} \cdots \frac{1}{5}\left[\frac{(1+\beta)(2-\beta)}{2}\right]^{1/2}$ if $j=1$
	$-\frac{2j-1}{5(j+1)}\left[\frac{(1+\beta)(2-\beta)}{2}\right]^{1/2} \cdots \frac{2j-1}{5(j+1)}\left[\frac{(1+\beta)(2-\beta)}{2}\right]^{1/2}$ if $j>1$
γ'_2	$-\frac{1}{5}\left[\frac{(1+\beta)(2-\beta)}{2}\right]^{1/2} \cdots \frac{1}{5}\left[\frac{(1+\beta)(2-\beta)}{2}\right]^{1/2}$ if $j=1$
	$-\frac{2j-1}{5(j+1)}\left[\frac{(1+\beta)(2-\beta)}{2}\right]^{1/2} \cdots \frac{2j-1}{5(j+1)}\left[\frac{(1+\beta)(2-\beta)}{2}\right]^{1/2}$ if $j>1$
η_2	$-\frac{(2-\beta)}{10} \cdots \frac{(2-\beta)}{10}$ if $j=1$
	$-\frac{(2j-1)(2-\beta)}{10(j+1)} \cdots \frac{(2j-1)(2-\beta)}{10(j+1)}$ if $j>1$

The anisotropy parameters of the second rank directly relate to the mean value of the photofragment alignment. As can be shown by integration of the fragment $K = 2$ state multipole in eq. (11) over all recoil angles, the parameters α_2, γ_2, and η_2 fulfill the condition:

$$\langle A_{20} \rangle = -2(\alpha_2 + \gamma_2 + \eta_2) \quad (32)$$

Here, $\langle A_{20} \rangle$ is the **z** component of the photofragment alignment (eq 6) averaged over the recoil angles for dissociation by linearly polarized light in a reference frame with **z** parallel to the photolysis light polarization vector **e**. The contribution from the γ'_2 parameter, as well as the contribution from all $K = 4$ parameters, vanish after averaging over all recoil angles.

Table 6. Range of the Rank $K = 4$ Anisotropy Parameters for $j_A = 2$

	range
α_4	$-\frac{5+2\beta}{81} \cdots \frac{1+\beta}{162}$
s_4	$-\frac{2}{27} \cdots \frac{1}{9}$
γ_4	$-\frac{2\sqrt{(2-\beta)(1+\beta)}}{15\sqrt{3}} \cdots \frac{2\sqrt{(2-\beta)(1+\beta)}}{15\sqrt{3}}$
γ'_4	$-\frac{2\sqrt{(2-\beta)(1+\beta)}}{15\sqrt{3}} \cdots \frac{2\sqrt{(2-\beta)(1+\beta)}}{15\sqrt{3}}$
η_4	$-\frac{\sqrt{15}(2-\beta)}{84} \cdots \frac{\sqrt{15}(2-\beta)}{108}$

Using eq 11 for fragment state multipoles with ranks $K = 2, 4$, $|Q| \le K$, and the definition of the even rank anisotropy parameters eq 31, the general expressions for specific photofragment state multipoles for two practically important experimental geometries can be written as one of the following:[85]

(1) geometry I where the dissociation light is linearly polarized along the **z** axis

$$\rho_{KQ}(\theta,\phi) = \frac{\sqrt{2K+1}V_K(j_A)\, e^{iQ\phi}}{4\pi\sqrt{2j_A+1}}\Big\{ d^K_{Q0}(\theta)(s_K - 2\alpha_K P_2(\cos\theta)) - \frac{\sqrt{6}}{2}\gamma_K[d^K_{Q1}(\theta) - d^K_{Q-1}(\theta)]\sin\theta\cos\theta - \frac{\sqrt{6}}{4}\eta_K[d^K_{Q2}(\theta) + d^K_{Q-2}(\theta)]\sin^2\theta\Big\} \quad (33)$$

or

(2) geometry II where dissociation light is linearly polarized along the **y** axis

$$\rho_{KQ}(\theta,\phi) = \frac{\sqrt{2K+1}V_K(j_A)e^{iQ\phi}}{4\pi\sqrt{2j_A+1}} \times \Big\{ d^K_{Q0}(\theta)(s_K + \alpha_K[P_2(\cos\theta)(1-\cos 2\phi) + \cos 2\phi]) + \frac{\sqrt{6}}{4}\gamma_K \sin\theta([d^K_{Q1}(\theta) - d^K_{Q-1}(\theta)]\cos\theta(1-\cos 2\phi) + i[d^K_{Q1}(\theta) + d^K_{Q-1}(\theta)]\sin 2\phi) + \frac{\sqrt{6}}{8}\eta_K([d^K_{Q2}(\theta) + d^K_{Q-2}(\theta)](\sin^2\theta + (1+\cos^2\theta)\cos 2\phi) - i[d^K_{Q2}(\theta) - d^K_{Q-2}(\theta)]2\cos\theta\sin 2\phi)\Big\} \quad (34)$$

As shown in section 2.2.3, linearly polarized probe light is sensitive only to the even-rank anisotropy parameters. Therefore, as many as nine independent anisotropy parameters, β, α_2, s_2, γ_2, η_2, α_4, s_4, γ_4, and η_4 can be extracted in general from experiment using linearly polarized light both

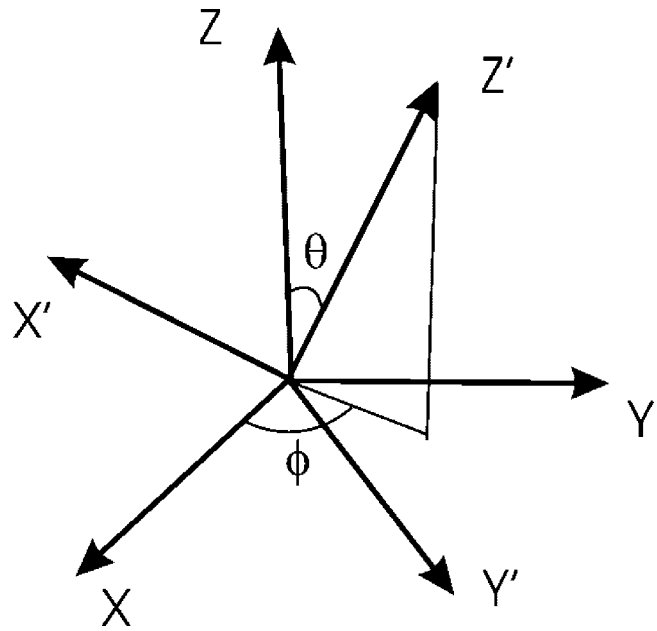

Figure 2. Laboratory and molecule reference frames.

in the dissociation and the probe channels using a 2 + 1 REMPI detection scheme.

The angular distribution of atomic photofragment alignment resulting from linearly polarized dissociation light has been the subject of dozens of publications since the mid-1990s (see, e.g., refs 22–24, 54, 56, 76, and 86–90). However, only a few results have been reported so far on determination of the high rank $K = 4$ fragment state multipoles.[62,85,91,92] The anisotropy parameters of the rank K ranging from $K = 0$ to $2j_A$ represent a total set of quantum mechanical variables that can be determined from photodissociation of randomly oriented parent molecules and contains all information about the dissociation dynamics.

This set is an alternative to Dixon's widely used bipolar moments,[5,93–95] having the advantage of giving more direct insight into the dissociation mechanisms, especially for low j values. The relationship between the laboratory frame anisotropy parameters and the bipolar moments of the rank $K = 2$ was given by Picheyev and co-workers,[33] and the expressions for the bipolar moments of the rank $K = 1$ and $K = 2$ in terms of the dynamical functions have recently been tabulated by Costen and Hall.[95]

2.1.8. Molecular Frame State Multipoles and Polarization Parameters

The power of ion imaging and other techniques that are used to measure the angular distribution of angular momentum polarization is that they readily lead to an understanding of the dynamics in the frame of the molecule. The laboratory and molecule reference frames are shown in Figure 2. The Z' axis of the molecular frame is parallel to the recoil direction $k(\theta, \phi)$. The transformation from the laboratory-frame state multipoles $\rho_{KQ}(\theta, \phi)$ to the body-frame state multipoles $\rho^{\mathrm{mol}}_{KQ'}$ can be written as

$$\rho_{KQ}(\theta,\phi) = (2j_A+1)^{1/2}\rho_{00}(\theta,\phi)\sum_{Q'} D^{K*}_{QQ'}(\phi,\theta,0)(\rho^{\mathrm{mol}}_{KQ'}) \tag{35}$$

where the index Q' is a component of multipole rank K along the recoil axis Z'. It is limited to the values $Q' = \pm 2, \pm 1$, and 0, see eq 11.

The body-frame state multipoles $\rho^{\mathrm{mol}}_{KQ'}$ in eq 35 obey the standard normalization condition:[45,46,48] $\rho^{\mathrm{mol}}_{00} = (2j_A + 1)^{-1/2}$. The inverse relationship is given by:

$$\rho^{\mathrm{mol}}_{KQ'} = [(2j_A+1)^{1/2}\rho_{00}(\theta,\ \phi)]^{-1}\times \sum_{Q}\rho_{KQ}(\theta,\ \phi)D^{K}_{QQ'}(\phi,\ \theta,\ 0) \tag{36}$$

By comparison of eqs 11 and 35, the body-frame state multipole can in general be presented as

$$\rho^{\mathrm{mol}}_{KQ'}(\theta) = \frac{3}{4\pi}\frac{\sqrt{2K+1}}{(2j_A+1)\rho_{00}(\theta)}\sum_{k_d}\sum_{q,q'}(-1)^{K+q'}\times (2k_d+1)^{1/2}E_{k_dQ'}(\mathbf{e})\times \begin{pmatrix} 1 & 1 & k_d \\ q' & -q & -Q' \end{pmatrix}\frac{f_K(q,q')}{f_0(0,0)+2f_0(1,1)}d^{k_d}_{Q'Q'}(\gamma) \tag{37}$$

where $E_{k_dQ'}(\mathbf{e})$ is a component of the light polarization matrix onto the recoil direction $\mathbf{k}$.

If the light is linearly polarized, the angle θ in eq 37 specifies the direction of the light polarization vector $\mathbf{e}$ with regard to the direction $\mathbf{k}$, while if the light is circularly polarized, this angle specifies the direction of the light propagation with regard to the direction $\mathbf{k}$.

In particular, if the photolysis light is linearly polarized, the molecular frame state multipoles are given by

(A) $K = 1, 3$

$$\rho^{\mathrm{mol}}_{K0}(\theta) = 0 \tag{38}$$

$$\rho^{\mathrm{mol}}_{K1}(\theta) = -\frac{3i}{\sqrt{2}}\frac{\sqrt{2K+1}\gamma'_k V_K(j_A)\sin\theta\cos\theta}{\sqrt{2j_A+1}[1+\beta P_2(\cos\theta)]} \tag{39}$$

$$\rho^{\mathrm{mol}}_{32}(\theta) = \frac{3}{\sqrt{5}}\frac{\sqrt{2K+1}\eta_K V_K(j_A)\sin^2\theta}{\sqrt{2j_A+1}[1+\beta P_2(\cos\theta)]} \tag{40}$$

and (B) $K = 2, 4$

$$\rho^{\mathrm{mol}}_{K0}(\theta) = \frac{\sqrt{2K+1}V_K(j_A)[s_K - 2\alpha_K P_2(\cos\theta)]}{\sqrt{2j_A+1}[1+\beta P_2(\cos\theta)]} \tag{41}$$

$$\rho^{\mathrm{mol}}_{K1}(\theta) = -\frac{\sqrt{6}}{2}\frac{\sqrt{2K+1}V_K(j_A)\gamma_K\sin\theta\cos\theta}{\sqrt{2j_A+1}[1+\beta P_2(\cos\theta)]} \tag{42}$$

$$\rho^{\mathrm{mol}}_{K2}(\theta) = -\frac{\sqrt{6}}{4}\frac{\sqrt{2K+1}V_K(j_A)\eta_K\sin^2\theta}{\sqrt{2j_A+1}[1+\beta P_2(\cos\theta)]} \tag{43}$$

$$\rho_{K-Q'}(\theta) = (-1)^{Q'}\rho^{*}_{KQ'}(\theta)$$

where θ is the angle between the light polarization vector $\mathbf{e}$ and the recoil axis.

According to eqs 38–40, linearly polarized light does not produce the component of the odd-rank polarization which is parallel to the recoil axis (with $Q' = 0$) but can produce the components with $Q' = 1, 2$ that break the axial symmetry, see eqs 5 and 7 and ref 21. Production of the transverse orientation component ρ^{mol}_{11} by linearly polarized photolysis and its subsequent detection by circularly polarized probe light is now widely used in experiment, for example, see refs 25, 57, 82–84, and 94.

As seen from eqs 38–43, in general, the body-frame state multipoles are a function of the angle θ, the parameter β, and the angle of rotation of the molecular axis γ. However, under certain conditions some of them do not depend on θ. In particular, in the limit of a pure parallel ($\beta^{(0)} = 2$) or a pure perpendicular ($\beta^{(0)} = -1$) transition, the state multipoles with $K = 2, 4$ and $Q' = 0$ in eq 41 do not depend on θ. In addition, if the rotation of the molecular axis can be neglected ($\gamma = 0$), the state multipoles with $K = 2, 3, 4$ and $Q' = 2$ for pure perpendicular transitions in eqs 40 and 43 do not depend on θ.

If the photolysis light is circularly polarized, the molecular frame state multipoles $\rho^{\mathrm{mol}}_{KQ'}$ are given by

(A) $K = 1, 3$

$$\rho_{K0}^{\mathrm{mol}}(\theta) = \sigma \frac{3\sqrt{2K+1}\alpha_K V_K(j)\cos\theta}{\sqrt{2j_A+1}\left[1-\frac{1}{2}\beta P_2(\cos\theta)\right]} \quad (44)$$

$$\rho_{K1}^{\mathrm{mol}}(\theta) = \sigma \frac{3\sqrt{2K+1}\gamma_K V_K(j)\sin\theta}{2\sqrt{2}\sqrt{2j_A+1}\left[1-\frac{1}{2}\beta P_2(\cos\theta)\right]} + \frac{3i\sqrt{2K+1}\gamma'_K V_K(j)\sin\theta\cos\theta}{2\sqrt{2}\sqrt{2j_A+1}\left[1-\frac{1}{2}\beta P_2(\cos\theta)\right]} \quad (45)$$

$$\rho_{K2}^{\mathrm{mol}}(\theta) = \frac{3}{\sqrt{5}} \frac{\sqrt{2K+1}\eta_K V_K(j)\sin^2\theta}{\sqrt{2j_A+1}\left[1-\frac{1}{2}\beta P_2(\cos\theta)\right]} \quad (46)$$

and (B) $K = 2, 4$

$$\rho_{K0}^{\mathrm{mol}}(\theta) = \frac{\sqrt{2K+1}V_K(j)[s_K + \alpha_K P_2(\cos\theta)]}{\sqrt{2j_A+1}\left[1-\frac{1}{2}\beta P_2(\cos\theta)\right]} \quad (47)$$

$$\rho_{K1}^{\mathrm{mol}}(\theta) = \frac{\sqrt{6}}{4} \frac{\sqrt{2K+1}V_K(j)\gamma_K \sin\theta\cos\theta}{\sqrt{2j_A+1}\left[1-\frac{1}{2}\beta P_2(\cos\theta)\right]} + \sigma\frac{\sqrt{6}i}{4} \frac{\sqrt{2K+1}V_K(j)\gamma'_K \sin\theta}{\sqrt{2j_A+1}\left[1-\frac{1}{2}\beta P_2(\cos\theta)\right]} \quad (48)$$

$$\rho_{K2}^{\mathrm{mol}}(\theta) = \frac{\sqrt{6}}{8} \frac{\sqrt{2K+1}V_K(j)\eta_K \sin^2\theta}{\sqrt{2j_A+1}\left[1-\frac{1}{2}\beta P_2(\cos\theta)\right]} \quad (49)$$

where θ is the angle between the direction of light propagation and the recoil axis. The value of the index $\sigma = +1$ and -1 correspond to the right and left light circular polarization, respectively.

The corresponding angular dependence of the molecular frame orientation and alignment parameters $\rho_{KQ'}^{\mathrm{mol}}$ can readily be obtained from eqs 38–49 using eqs 5–8.

Three possible dissociation mechanisms giving rise to fragment orientation, corresponding to three components of the rank 1 state multipole $\rho_{1Q'}^{\mathrm{mol}}(\theta)$, where $Q' = 0, \pm 1$, can be described by a simple vector model in terms of the components of the fragment electronic angular momentum onto the body frame axes.[21] The rank $K > 1$ state multipoles do not allow such simple physical modeling. However, in all cases the $Q' = 0$ matrix element of the body-frame state multipole is related to an incoherent parallel or perpendicular optical excitation of the parent molecule; the $Q' = \pm 1$ matrix elements are related to the coherent optical excitation of a parallel and a perpendicular transition, and the $Q' = \pm 2$ matrix elements are related to the coherent optical excitation of two perpendicular transitions.

Equations 38–49 can be used for definition of the set of *polarization* parameters $\mathbf{a}_Q^{(K)}(p)$ that are expressed in the molecular frame and contain all information about the dissociation dynamics. The symbol (p) denotes (||), ($\perp$), (||, $\perp$), or ($\perp$, $\perp$) and describes the excitation symmetry. This set of parameters has been introduced by Rakitzis and Zare.[55,96] The set of *polarization* parameters $\mathbf{a}_Q^{(K)}(p)$ is an alternative to the set of the *anisotropy* parameters described above and contain the same dynamical information. Each set of parameters is characteristic of the intrinsic dynamics of the dissociation process and therefore does not depend on the recoil angle θ.

The parameters $\mathbf{a}_Q^{(K)}(p)$ are expressed in the molecular frame and have an advantage for interpreting the experimental data because they are directly related to the particular values of the molecular frame-state multipoles as shown in Table 7. However, application of the polarization parameters $\mathbf{a}_Q^{(K)}(p)$ is limited to the case of fast photolysis in the axial recoil approximation, while the anisotropy parameters can be determined from experiment without any reference to the photolysis mechanism.[186] Moreover, often the spatial modulations in an ion image arising from orientation and alignment effects in the photofragmentation process constitute only a small fraction of the total signal. As shown in section 2.2.3, linear combinations of experimental images corresponding to different experimental geometries (light polarizations) may be used to isolate the laboratory-frame anisotropy parameters from the total signal and thereby increase the accuracy of the parameter values so determined.[21,77,85]

The relationship between the *anisotropy*[33] and *polarization*[96] parameters of the ranks $K = 1-4$ within the axial recoil approximation are presented in Table 7. The symbols c and l in the third column in Table 7 indicate that the corresponding "physical meaning" expression is given for right circular and linear photolysis light polarization, respectively. The constants V_2, V_3, and V_4 in the second column are given in eqs 27 and 31.

Table 7 is similar to the forms that have recently been published by Alexander[190] and by Costen and Hall,[95] generalized, however, to include ranks $K = 3, 4$. In addition, the definitions of some of the parameters in Table 7 are slightly modified to give them the physical meaning shown in the third column. In particular, the definition of all $\mathbf{a}_1^{(K)}(p)$ "coherent" polarization parameters have been modified in the way used by Costen and Hall[95] by explicit inclusion of the factor $[(1+\beta)(2-\beta)]^{1/2}$ and using the relationship

$$\frac{\sqrt{2f_0(0,0)f_0(1,1)}}{f_0(0,0)+2f_0(1,1)} = \frac{1}{3}\sqrt{(2-\beta)(1+\beta)} \quad (50)$$

The above results are important not only for investigation of photodissociation dynamics but also for reaction dynamics because the non-zero rank $K = 2$ and 4 state multipoles affect the shape of the electron cloud in the recoiling atom.[21] This is illustrated in Figure 3 for O(^{1}D) from ozone photodissociation at 266 nm.[80] In this case, it is the electron−hole distribution, which is the deviation of the charge cloud from a purely isotropic form, shown explicitly as a function of recoil angle. The $K = 0, 2$ contributions to the O atom density matrix[80,98] are also shown.

It should also be emphasized that the rank $K = 1$ and 3 state multipoles have no influence on the shape of the electron cloud in the recoiling atom. That is, purely oriented photofragments preserve the spherical symmetry of the angular distribution of the electron cloud. Tensors with odd rank are proportional to the corresponding magnetic multipoles and describe the distribution of electric currents within the atoms.[46]

Table 7. Relationship between the Anisotropy and the Polarization Parameters of Rank $K = 1-4$ (in the Axial Recoil Approximation)

polarization parameter	dynamical function expression	physical meaning	anisotropy parameter expression
$\mathbf{a}_0^{(1)}(\perp)$	$\frac{f_1(1,1)}{f_0(1,1)}$	$A_{10}^{\mathrm{mol}}(\theta = 0),\ c$	$\frac{6}{2-\beta}\alpha_1$
$Re[\mathbf{a}_1^{(1)}(\parallel,\perp)]$	$\frac{Re[f_1(1,0)]}{[2f_0(1,1)f_0(0,0)]^{1/2}}$	$Re[A_{11}^{\mathrm{mol}}(\theta = \pi/2,\ \beta = 0)],\ c$	$\frac{3}{2[(2-\beta)(1+\beta)]^{1/2}}\gamma_1$
$Im[\mathbf{a}_1^{(1)}(\parallel,\perp)]$	$\frac{Im[f_1(1,0)]}{[2f_0(1,1)f_0(0,0)]^{1/2}}$	$Im[A_{11}^{\mathrm{mol}}(\theta = \pi/4,\ \beta = 0)],\ l$	$-\frac{3}{2[(2-\beta)(1+\beta)]^{1/2}}\gamma'_1$
$\mathbf{a}_0^{(2)}(\perp)$	$\frac{5}{V_2}\frac{f_2(1,1)}{f_0(1,1)}$	$A_{20}^{\mathrm{mol}}(\beta = -1),\ l$	$\frac{10}{2-\beta}(\alpha_2 + s_2)$
$\mathbf{a}_0^{(2)}(\parallel)$	$\frac{5}{V_2}\frac{f_2(0,0)}{f_0(0,0)}$	$A_{20}^{\mathrm{mol}}(\beta = 2),\ l$	$\frac{5}{1+\beta}(s_2 - 2\alpha_2)$
$Re[\mathbf{a}_1^{(2)}(\parallel,\perp)]$	$-\frac{5}{V_2}\frac{Re[f_2(1,0)]}{[2f_0(1,1)f_0(0,0)]^{1/2}}$	$Re[A_{21}^{\mathrm{mol}}(\theta = \pi/4,\ \beta = 0)],\ l$	$-\frac{5\sqrt{3}}{2[(2-\beta)(1+\beta)]^{1/2}}\gamma_2$
$Im[\mathbf{a}_1^{(2)}(\parallel,\perp)]$	$-\frac{5}{V_2}\frac{Im[f_2(1,0)]}{[2f_0(1,1)f_0(0,0)]^{1/2}}$	$Im[A_{21}^{\mathrm{mol}}(\theta = \pi/2,\ \beta = 0)],\ c$	$-\frac{5\sqrt{3}}{2[(2-\beta)(1+\beta)]^{1/2}}\gamma'_2$
$\mathbf{a}_2^{(2)}(\perp)$	$-\frac{5V_2^{-1}}{2}\frac{f_2(1,-1)}{f_0(1,1)}$	$A_{22}^{\mathrm{mol}}(\beta = -1),\ l$	$-\frac{5}{\sqrt{6}}\frac{3}{2-\beta}\eta_2$
$\mathbf{a}_0^{(3)}(\perp)$	$\frac{V_3^{-1}}{2}\frac{f_3(1,1)}{f_0(1,1)}$	$A_{30}^{\mathrm{mol}}(\theta = 0),\ c$	$\frac{3}{2-\beta}\alpha_3$
$Re[\mathbf{a}_1^{(3)}(\parallel,\perp)]$	$\frac{V_3^{-1}}{2}\frac{Re[f_3(1,0)]}{[2f_0(00)f_0(1,1)]^{1/2}}$	$Re[A_{31}^{\mathrm{mol}}(\theta = \pi/2,\ \beta = 0)],\ c$	$\frac{3}{4[(2-\beta)(1+\beta)]^{1/2}}\gamma_3$
$Im[\mathbf{a}_1^{(3)}(\parallel,\perp)]$	$\frac{V_3^{-1}}{2}\frac{Im[f_3(1,0)]}{[2f_0(00)f_0(1,1)]^{1/2}}$	$Im[A_{31}^{\mathrm{mol}}(\theta = \pi/4,\ \beta = 0)],\ l$	$-\frac{3}{4[(2-\beta)(1+\beta)]^{1/2}}\gamma'_3$
$\mathbf{a}_2^{(3)}(\perp)$	$-\frac{V_3^{-1}}{4}\frac{Im[f_3(1,-1)]}{f_0(1,1)}$	$A_{32}^{\mathrm{mol}}(\beta = -1),\ l$	$\frac{3}{\sqrt{5}(2-\beta)}\eta_3$
$\mathbf{a}_0^{(4)}(\perp)$	$\frac{9V_4^{-1}}{4}\frac{f_4(1,1)}{f_0(1,1)}$	$A_{40}^{\mathrm{mol}}(\beta = -1),\ I$	$\frac{18}{2-\beta}(\alpha_4 + s_4)$
$\mathbf{a}_0^{(4)}(\parallel)$	$\frac{9V_4^{-1}}{4}\frac{f_4(0,0)}{f_0(0,0)}$	$A_{40}^{\mathrm{mol}}(\beta = 2),\ l$	$\frac{9}{1+\beta}(s_4 + 2\alpha_4)$
$Re[\mathbf{a}_1^{(4)}(\parallel,\perp)]$	$-\frac{9V_4^{-1}}{4}\frac{Re[f_4(1,0)]}{[2f_0(00)f_0(1,1)]^{1/2}}$	$Re[A_{41}^{\mathrm{mol}}(\theta = \pi/4,\ \beta = 0)],\ l$	$-\frac{9\sqrt{3}}{8[(2-\beta)(1+\beta)]^{1/2}}\gamma_4$
$Im[\mathbf{a}_1^{(4)}(\parallel,\perp)]$	$-\frac{9V_4^{-1}}{4}\frac{Im[f_4(1,0)]}{[2f_0(00)f_0(1,1)]^{1/2}}$	$Im[A_{41}^{\mathrm{mol}}(\theta = \pi/2,\ \beta = 0)],\ c$	$-\frac{9\sqrt{3}}{8[(2-\beta)(1+\beta)]^{1/2}}\gamma'_4$
$\mathbf{a}_2^{(4)}(\perp)$	$-\frac{9V_4^{-1}}{8}\frac{f_4(1,-1)}{f_0(1,1)}$	$A_{42}^{\mathrm{mol}}(\beta = -1),\ l$	$-\frac{9}{4\sqrt{6}}\frac{3}{2-\beta}\eta_4$

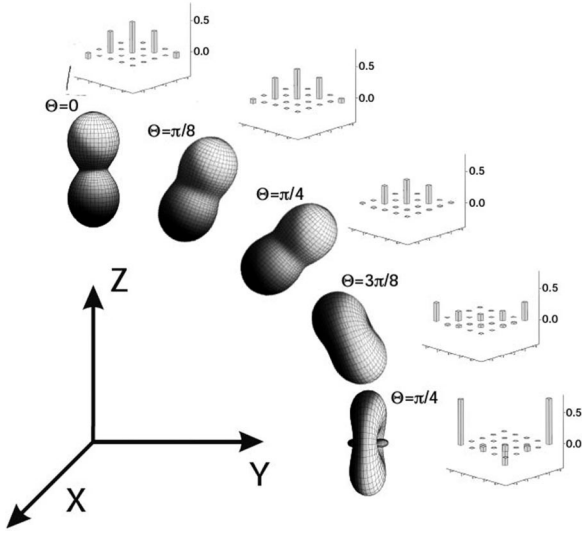

Figure 3. Angle-dependent O(^1D) charge cloud anisotropy and $K = 0, 2$ density matrices for 266 nm dissociation of ozone.

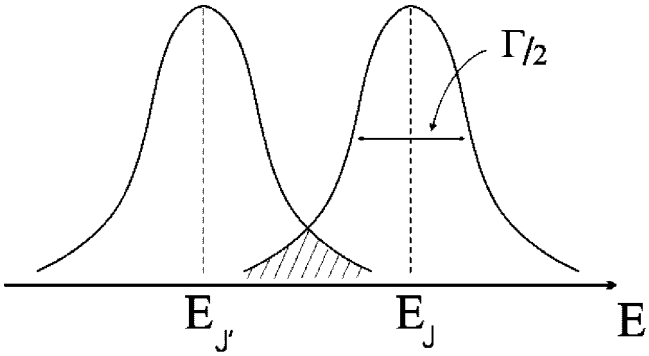

Figure 4. Typical excited-state rotational structure for intermediate case.

2.1.9. Role of J, J′ Coherence in Molecular Photodissociation

Kuznetsov and Vasyutinskii[53] have examined the role of the J, J' coherence in molecular photodissociation by exploring several different methods of taking the summation over the indices J and J' in the expression for the polarization cross section in eq 1. Their approach explored different regimes depending of the ratio between the energy difference of the neighboring rotation level structure $E_{Je}-E_{J'e}$ and the level width $\Gamma_e/2$.

2.1.9.1. Fast Predissociation $\Gamma_e/2 \gg (E_{Je}-E_{J'e})$. In this case, the scattering wave function $\chi^J_{\bar{n}\Omega_R;n\Omega}(R)$ in eq 9 can be presented in the form (eq 10) where, in the quasiclassical approximation, only the phase $\delta^J_{n\Omega_k}$ depends on J and the summation over J, J' must be undertaken in eq 1, including the *interference terms* $J \neq J'$, a quantum effect that results in the production of a rotational wave packet in the molecular excited-state and impacts the spatial and spin anisotropy of the photofragments. The angular distribution of the photofragment orbital polarization in this limit describes the direct photodissociation, which is discussed in detail in sections 2.1.3−2.1.8 (see also the review paper by Gordon and Hall.[61])

2.1.9.2. Intermediate Case $\Gamma_e/2 \simeq (E_{Je}-E_{J'e})$. For the situation in which the width of the rotational energy levels is comparable to their separation, we have the intermediate case. The typical rotational structure of the molecular excited state is given in Figure 4. Here, the rotational quasibound energy levels partially overlap with each other in the region between the rotational lines but have practically no overlap at the line centers. J, J' coherence can therefore be neglected for the photon energies in the vicinity of the line centers but must be accounted for in the overlapping areas. This is the most complicated case that can be treated strictly with pure quantum mechanical methods. Although the scattering wave function can still be developed in form 10, in general both the phase $\delta^J_{n\Omega}$ and the amplitude $\tilde{\chi}^J_{\bar{n}\Omega_R;n\Omega}(R)$ strongly depend on the angular momentum J and must be determined numerically. This can only be achieved for a few molecules because the excited-state potential energy surfaces are usually not known. As shown by Siebbeles and co-workers[99–102] in their analysis of H_2 predissociation and also by Kim and co-workers,[103] the β parameter dramatically changes with photon energy throughout the absorption profile. It can thus achieve classically forbidden values in the overlapping region where the contribution from the J, J' coherence must be accounted for in the calculation.

2.1.9.3. Slow Predissociation $\Gamma_e/2 \ll (E_{Je}-E_{J'e})$. The slow predissociation limit occurs when the molecular lifetime is much longer than the rotational period and the photofragment angular distribution has cylindrical symmetry with respect to the total angular momentum J. Coherent excitations from the initial rotational level J_i to different rotational levels of the excited state J, J' by monochromatic light can be neglected, so only the terms with $J = J'$ (describing the incoherent excitation of single rotational states) need be taken into account in eq 1. In general, the J, J' coherence *can* be excited in the slow predissociation case by laser pulses in the picosecond or femtosecond time domain. These effects are out of the scope of this review.

2.1.10. Photofragment State Multipole Angular Distribution: Slow Predissociation

The photofragment state multipole angular distributions for the case of slow predissociation has recently been analyzed by Kuznetsov and Vasyutinskii.[53] In this case, the expression for the differential polarization cross section can be obtained by substituting $J = J'$ to the general form of the cross section in eq 1.

For slow predissociation via a single rotational branch, the zero-rank state multipole can still be written in the form in eq 23, where the parameter β can be written as[53]

$$\beta = \sqrt{30}(-1)^{J+J_i}\sqrt{2J+1}\,C^{J\Omega}_{J\Omega 20}\begin{Bmatrix} J & J & 2 \\ 1 & 1 & J_i \end{Bmatrix} \qquad (51)$$

which is valid for arbitrary values of the initial angular momentum J_i.

As can be seen from eq 51, the parameter β is a function of the total angular momenta J, J_i involved in the photoprocess and of the symmetry of the molecular electronic excited state Ω but not of the symmetry of the initial state Ω_i.

In the high-J limit $J_i, J \gg 1$, the parameter β of an isolated rotational branch in eq 51 does not depend on the symmetry of both electronic molecular states and has asymptotic values of $\beta(Q) = -1$, $\beta(P) = \beta(R) = 1/2$, in agreement with previous results reported by Zare[104] and Liyanage and Gordon.[105]

For slow predissociation via the broadband incoherent excitation of P, R, and Q rotational branches in the high-J limit, the anisotropy parameter β is given by[53]

$$\beta = \frac{1}{4}\beta^{(0)} \tag{52}$$

where $\beta^{(0)}$ is the axial recoil anisotropy parameter in eq 26, and the zero-rank dynamical functions $f_0(q, q)$ have the same form as in the fast dissociation case (eq 13). However, they should be calculated using appropriate predissociative scattering functions $\chi^{J_i}_{n\Omega;\tilde{n}\Omega}(R)$ in eq 14. The expression in eq 52, which is a result of the full quantum mechanical treatment, is in perfect agreement with previous classical and semiclassical treatments.[74,106]

For slow predissociation via broadband incoherent excitation, the arbitrary rank photofragment state multipole $\rho_{KQ}(\theta, \varphi)$ can be presented in the same form as in eqs 29, 30, 33, and 34 if each anisotropy parameter is written as a product of a corresponding axial recoil anisotropy parameter in eqs 27 and 31 and a reduction factor $[d^{k_d}_{Q'0}(\pi/2)]^2$, which is equal to the rotation factor $d^{k_d}_{Q'Q'}(\gamma)$ in Table 3 averaged over the rotation angle γ

$$[d^{k_d}_{Q'0}(\pi/2)]^2 = \langle d^{k_d}_{Q'Q'}(\gamma)\rangle = \frac{1}{2\pi}\int_0^{2\pi} d^{k_d}_{Q'Q'}(\gamma)\, \mathrm{d}\gamma \tag{53}$$

All possible rank $K = 0,..., 4$ anisotropy parameters that can be produced in slow predissociation are collected in Table 8. As shown there, the reduction factors depend on the dissociation mechanism: for example, the anisotropy parameters α_1, α_3, γ_2, γ_4, γ'_1, and γ'_3 are zero for slow predissociation implying that the corresponding dissociation mechanisms give no contribution to the product polarization. This prediction is also consonant with recent experimental results of Brouard and co-workers[107,108] who reported very small values of the parameter γ_2 in predissociation of N_2O and SO_2.

For the anisotropy parameters s_2 and s_4, the reduction factor is equal to unity, while for all other anisotropy parameters, the reduction factors are less than unity. Specifically, the parameters β, α_2, and γ_2 are reduced by a factor of 4 compared to the axial recoil values. For the $_2$ parameter, this prediction qualitatively agrees with the experimental result of Brouard and co-workers[108] on SO_2. However, for the N_2O case the parameters α_2 and s_2 are on the same order of magnitude.[107] This may be because the predissociation effects are larger for SO_2, which has a highly structured absorption spectrum compared with N_2O. The parameters for N_2O do seem to be consistent with a shorter lifetime.

2.2. Detection of the Photofragment Polarization Using 2 + 1 REMPI

2.2.1. General Expressions for the 2 + 1 REMPI Signal

Multiphoton absorption of polarized probe light by photofragments is now widely used for investigation of orbital orientation and alignment in imaging experiments. Here we consider the most popular experimental scheme of two-photon absorption of the probe light to a resonant photofragment excited-state followed by ionization of the photofragment with the third photon (2 + 1 REMPI scheme). The equation of the density matrix of the resonant state $|r\rangle$ after the two-photon absorption from the initial state $|i\rangle$ can be written as

$$\frac{\mathrm{d}\rho_{r'r}}{\mathrm{d}t} = F_{r'r} - \frac{1}{\tau}\rho_{r'r} \tag{54}$$

where r is the set of quantum numbers of the resonant state, τ is the resonant state lifetime, and $F_{r'r}$ is the excitation matrix, given by the second order perturbation theory expression:

$$F_{r'r} = F_0 \sum_{i,i',e,e'} \frac{\hat{V}^*_{re}\hat{V}^*_{ei}\hat{V}_{r'e'}\hat{V}_{e'i'}}{\left(\omega_{ei} - \omega + i\frac{\Gamma_e}{2}\right)\left(\omega_{e'i'} - \omega - i\frac{\Gamma_{e'}}{2}\right)}\rho_{i'i} \tag{55}$$

Here F_0 is a constant which is proportional to the square of the light intensity, $\hat{V}$ is the standard interaction operator $\hat{V} = \mathbf{d}\cdot\mathbf{e}$, $\mathbf{d}$ is a photofragment electronic dipole moment, $\mathbf{e}$ is the probe light polarization vector, and $\rho_{i'i}$ is the initial state photofragment density matrix. The summation in eq 55 is performed over all quantum numbers of the initial (i, i') and intermediate (e, e') states. For a diatomic molecule, the initial state wave function can be written as $|i\rangle \equiv |n_i, \Omega_i, \upsilon_i, J_i, M_i\rangle$, where J_i is a total angular momentum, M_i and Ω_i are projections of J_i onto the laboratory and internuclear axes, respectively, υ_i is a vibrational quantum number, and n_i is a set of additional quantum numbers which depends on the details of the angular momentum coupling. For an atom, the initial state wave function in the $L-S$ coupling scheme can be written as $|i\rangle \equiv |n_i, L_i, S_i, j_i, m_i\rangle$, where L_i, S_i, and j_i are fragment orbital, spin, and total angular momentum, respectively, m_i is the projection of j_i onto the laboratory Z axis, and n_i is a general quantum number. Similar expressions stand for the wave functions of intermediate $|e\rangle$ and resonant $|r\rangle$ states.

In the steady state regime, the density matrix of the resonant state $|r\rangle$ is proportional to the excitation matrix

$$\rho_{r'r} = \tau F_{r'r} \tag{56}$$

If all resonant state m-substates are equally populated, only the intensity of the two-photon transition is important

$$I = Tr[\rho_{r'r}] \tag{57}$$

and the last ionization transition may not be accounted for in the calculation.[109] Detection by 2 + 1 REMPI is widely used for investigation of vector correlations in chemical reaction products.[21,58,109,110] However, in general, the resonant state m-substates are not equally populated after a two-photon transition that can affect the initial state polarization detection accuracy because the intensity of the ionization transition can also be m-dependent.[111,112]

A method for extraction of orientation and alignment information from (2 + 1 REMPI) measurements has been developed by Kummel and co-workers.[58,109] A convenient modification of this method that adapts the approach of Kummel and co-workers to the case of atoms and provides complete separation between the scalar and the tensor quantities in the expression for two-photon light absorption by the photofragments has been suggested by Bracker et al.[42] According to ref 42, the general expression describing the

Table 8. Rank $K = 0,..., 4$ Laboratory Frame Anisotropy Parameters for Slow Predissociation of Molecules after Summation over P, R, and Q Rotational Branches in the High J Limit

K	0	1	2	3	4
β	$^1/_4\beta^{(0)}$	–	–	–	–
α_K	–	0	$^1/_4\alpha_2^{(0)}$	0	$^1/_4\alpha_4^{(0)}$
s_K	–	–	$s_2^{(0)}$	–	$s_4^{(0)}$
γ_K	–	$^1/_2\gamma_1^{(0)}$	0	$^1/_2\gamma_3^{(0)}$	0
γ'_K	–	0	$^1/_2\gamma_2^{(0)'}$	0	$^1/_2\gamma_4^{(0)'}$
η_K	–	–	$^3/_8\eta_3^{(0)}$	$^3/_8\eta_3^{(0)}$	$^3/_8\eta_4^{(0)}$

intensity of absorption of the probe light by the fragments in the state multipole representation can be written as

$$I = C \sum_{K_i k_1 k_2} S^{k_2}_{K_i k_1} [(\rho_{K_i} \otimes E_{k_1})_{k_2} \cdot E_{k_2}] \quad (58)$$

where the tensor product is calculated according to

$$[(\rho_{K_i} \otimes E_{k_1})_{k_2} \cdot E_{k_2}] = \sum_{Q_i, q_1, q_2} (-1)^{K_i - k_1} \sqrt{2k_2 + 1} \times \begin{pmatrix} K_i & k_1 & k_2 \\ Q_i & q_1 & -q_2 \end{pmatrix} E_{k_1 q_1} \rho_{K_i Q_i} E_{k_2 - q_2} \quad (59)$$

Here $\rho_{K_i Q_i} \equiv \rho_{K_i Q_i}(\theta, \phi)$ are the components of the fragment state multipole described earlier, and $E_{k_1 q_1}$ and $E_{k_2 - q_2}$ are polarization matrices with ranks k_1 and k_2 that describe the polarization of the first and second photons, respectively.[45] The ranks k_1 and k_2 are limited to the values $k_1, k_2 = 0, 2$ in case of linearly polarized light and to the values $k_1, k_2 = 0, 1, 2$ in case of circularly polarized light.

The scalar factor $S^{k_2}_{K_i k_1}$ in eq 58 depends on all quantum numbers of the initial, intermediate, and resonant states involved in the two-photon process but not on the projections of any tensor, and C is the proportionality constant, which depends on the intensity of the probe light. The multipole rank $K = 4$ in eq 58 corresponds to the maximum possible rank that can be measured with a two-photon detection technique. The details of specific expressions for the (2 + 1) resonance-enhanced multiphoton ionization (2 + 1 REMPI) signal for several most frequently used experimental geometries can be found in the review paper.[21]

Equation 58 can be simplified if the first and second photons are identical to each other and if the probe light polarization is either linear or circular (not elliptical). In this case, the intensity of absorption of the probe light by the fragments for any direction of the probe light polarization can be written as[85,111]

$$I = C \sum_{K_i} \sqrt{\frac{4\pi}{2K_i + 1}} (\rho_{K_i} \cdot Y_{K_i}(\mathbf{n})) P_{K_i} \quad (60)$$

where the rank K_i is limited to the values $K_i = 0, 2, 4$ if the light is linearly polarized and to the values $K_i = 0, 1, 2, 3, 4$ if the light is circularly polarized. $Y_{K_i Q_i}(\mathbf{n})$ in eq 60 is a spherical harmonic and $(\rho_{K_i} \cdot Y_{K_i}(\mathbf{n}))$ is a tensor scalar product which is calculated according to

$$(\rho_{K_i} \cdot Y_{K_i}(\mathbf{n})) = \sum_{Q_i} (-1)^{Q_i} \rho_{K_i Q_i} Y_{K_i - Q_i}(\mathbf{n}) \quad (61)$$

The vector $\mathbf{n} = (\vartheta, \varphi)$ is parallel to the probe light polarization **e** if the light is linearly polarized and is parallel to the direction of the light propagation if the light is circularly polarized. The fragment state multipoles ρ_{KQ} in eqs 60 and 61 are assumed to be a function of the recoil angles θ, ϕ. For linearly polarized light, the scalar factors P_K in eq 60 are known two-photon linestrength factors.[21,113] For circularly polarized probe light, the linear linestrength factors P_K in eq 60 should be replaced by the circular linestrength factors σP^c_K defined in ref 21 where $\sigma = \pm 1$ for right and left circular light polarization, respectively. Generalization of eq 60 to the case of n-photon absorption was reported by Shternin and co-workers.[112]

For three experimental geometries, corresponding to the linear probe laser polarization along the axes X, Y, and Z, the angles ϑ, φ stand for $\vartheta = \pi/2, \varphi = 0$, $\vartheta = \pi/2, \varphi = \pi/2$, and $\vartheta = 0, \varphi = 0$, respectively. For linearly polarized light propagating along the Y axis, the angle φ is equal to zero and the angle ϑ is in the XZ plane. The expression for the two-photon REMPI absorption signal for this case was first given by Meyer.[114] For linearly polarized light propagating along the X axis, the angle φ is equal to $\pi/2$, and the angle ϑ is in the YZ plane. For linearly polarized light propagating along the Z axis, the angle ϑ is equal to $\pi/2$, and the angle φ is in the XY plane.

2.2.2. Isolation of a Particular Rank State Multipole

The absorption signal in eq 60 can contain in general up to sixteen unknown anisotropy parameters β, s_K, α_K, γ_K, and η_K, which should be determined from the experimental images by a fitting procedure. For increasing the accuracy of the experiment and for reduction of the number of parameters, it is useful to isolate some of them by using appropriate experimental geometries. In particular, for determination of the alignment-free anisotropy parameter β, it is important to isolate the term $\rho_{00}(\theta, \phi)$ which is proportional to the number of the photofragments only. This can be done by taking linear combinations of the signal from different geometries. One of these combinations is

$$\frac{1}{3}[I_X(\theta, \phi) + I_Y(\theta, \phi) + I_Z(\theta, \phi)] = CP_0 \rho_{00}(\theta, \phi) \quad (62)$$

where I_X, I_Y, and I_Z are the 2 + 1 resonance-enhanced multiphoton ionization (2 + 1 REMPI) signals for the experimental geometries corresponding to the linear probe laser polarization along the axes X, Y, and Z, respectively.

The *lhs* of expression 62 does not contain the terms of the rank $K = 1, 2, 3$, while the terms of the rank $K = 4$ are neglected compared with the rank $K = 0$ term.

Note that even if the photolysis light is axially symmetric over the Z axis, the ionization signals I_X and I_Y in eq 62 are in general not the same but depend on the detection details. However, they are the same if the total ionization intensity is measured by averaging over all recoil directions. Then, eq 62 can be simplified as follows

$$\frac{1}{3}[\langle I_Z(\theta, \phi) \rangle + 2\langle I_Y(\theta, \phi) \rangle] = \frac{CP_0}{\sqrt{2j + 1}} \quad (63)$$

where the angular brackets mean averaging and the known normalization condition for the zeroth-rank state multipole $\rho_{00} = 1/\sqrt{(2j + 1)}$ has been used. The expression in eq 63 is useful for normalization of the orientation and alignment signals (see, e.g., ref 42 and 115) because the experiment can be carried out by changing only the probe laser polarization, without moving the laser beam direction.

Another important form of the rank $K = 1, 2, 3$ independent expression is[21]

$$I_X(\theta, \phi) + I_Y(\theta, \phi) - \frac{1}{3}[I^z_R(\theta, \phi) + I^z_L(\theta, \phi)] = CP_0 \rho_{00}(\theta, \phi) \quad (64)$$

where I^z_R and I^z_L are the 2 + 1 resonance-enhanced multiphoton ionization (2 + 1 REMPI) signals for the experimental geometries, corresponding to right and left circularly polarized probe light propagating along the Z axis. In this case, we again neglect the terms of rank $K = 4$ in the *lhs* compared to those of rank $K = 0$. Although eq 64 is strictly valid only for $j_i \neq j_f$, or $L_i \neq L_f$, it has an advantage compared to eq 62: Determination of fragment population for any fragment angular distribution can be achieved by changing only the probe laser polarization, without changing the laser

beam direction. Because the value in the right part of eq 64 is scalar, the expression is essentially unchanged for any propagation direction of the probe light (i.e., with only appropriate change of the X, Y, and Z sub- and superscript indices).

The combination in eq 63 has been used for normalization of the orientation/alignment signals,[23,42,62,88,116,117] and the combination in eq. 64 was used for determination of the alignment-free value of the β parameter from experiment.[116]

As mentioned earlier, it is often useful to isolate the polarization contribution by taking linear combinations of the signal from different geometries in such a way that the population term $\rho_{00}(\theta, \phi)$ cancels. The appropriate expressions are[21]

$$\frac{I_Z(\theta,\phi) - I_{X,Y}(\theta,\phi)}{\langle I_X\rangle + \langle I_Y\rangle + \langle I_Z\rangle} = \frac{\sqrt{2j_A+1}}{2P_0} \times \left[P_2\left(\rho_{20}(\theta,\phi) \mp \frac{\sqrt{6}}{3}\, Re[\rho_{22}(\theta,\phi)]\right) + \frac{P_4}{12}(5\rho_{40}(\theta,\phi) \pm 2\sqrt{10}\, Re[\rho_{42}(\theta,\phi)] - \sqrt{70}\, Re[\rho_{44}(\theta,\phi)])\right] \quad (65)$$

$$\frac{I_X(\theta,\phi) - I_Y(\theta,\phi)}{\langle I_X\rangle + \langle I_Y\rangle + \langle I_Z\rangle} = \frac{\sqrt{(2j_A+1)}}{3P_0}\left[\sqrt{6}P_2\, Re[\rho_{22}(\theta,\phi)] - \frac{\sqrt{10}P_4}{2}\, Re[\rho_{42}(\theta,\phi)]\right] \quad (66)$$

$$\frac{I_R^z(\theta,\phi) - I_L^z(\theta,\phi)}{\langle I_X\rangle + \langle I_Y\rangle + \langle I_Z\rangle} = \frac{2\sqrt{(2j_A+1)}}{3P_0}[P_1^c[\rho_{10}(\theta,\phi)] + P_3^c[\rho_{30}(\theta,\phi)]] \quad (67)$$

In the derivation of expressions 65–67, the terms of rank $K = 4$ have been neglected in all denominators. The combinations in eqs 65 and 66 are sensitive only for determination of the even rank ($K = 2, 4$) state multipoles, while the combination in eq 67 is sensitive for determination of the odd rank ($K = 1, 3$) state multipoles only.

The absorption signal detected with linearly polarized probe light in eqs 65 and 67 can still contain up to eight unknown anisotropy parameters that must be determined from the experimental images. However, the determination of all eight rank 2 and 4 alignment anisotropy parameters from these expressions has certain disadvantages because it requires a sophisticated fitting procedure.[85] It is also difficult to imagine an accurate modification of this method that would take into consideration the parameter speed dependence.

Fortunately, the expression in eq 60 provides a useful combination of the REMPI absorption signals that isolates rank 4 state multipoles from all others and thus can simplify the subsequent analysis:

$$I_{\left(\frac{\pi}{2},\frac{\pi}{2}\right)}(\theta,\phi) + I_{\left(0,\frac{\pi}{2}\right)}(\theta,\phi) - I_{\left(\frac{\pi}{4},\frac{\pi}{2}\right)}(\theta,\phi) - I_{\left(-\frac{\pi}{4},\frac{\pi}{2}\right)}(\theta,\phi) = \frac{CP_4}{16}[35\rho_{40}(\theta,\phi) + 14\sqrt{10}\ Re[\rho_{42}(\theta,\phi)] + \sqrt{70}\, Re[\rho_{44}(\theta,\phi)]] \quad (68)$$

where the probe light is linearly polarized and the values of the polar angles (ϑ, φ) of the probe light polarization vector **e** are shown as subscript indices. The probe light is assumed to propagate along the X axis. Equation 68 is valid for any polarization of the photolysis light. Useful particular cases of eq 68 for geometries I and II (see eqs 33 and 34) are given by Smolin and co-workers.[85]

2.2.3. Determination of the Anisotropy Parameters from 2-Dimensional Velocity Images

Several approaches have been used by investigators to obtain recoil energy and angular distributions from ion imaging data. The original approach uses an inverse Abel transform to directly invert the images to obtain the original three-dimensional ion spatial distribution.[118,119] A widely used modification of this method has been recently suggested by Dribinski and co-workers,[120] which is based on expanding the image in a basis set of Gaussian-like functions. The inversion approach is ideally suited to studies of simple photolysis systems with no product angular momentum alignment; however, it can only be used if the image is a projection of a cylindrically symmetric distribution, where the symmetry axis lies parallel to the two-dimensional image. This experimental geometry followed by the inverse Abel transform was successfully used by several groups also for investigation of the photofragment angular momentum distributions.[56,79,87,91,92,121] However, if many anisotropy parameters must be simultaneously determined, this approach requires uncommon experimental geometries and a sophisticated fitting procedure[91] that can dramatically reduce the accuracy of the experimental data.

Another approach involves forward convolution fitting of the image, whereby images are simulated based on a scattering distribution and compared with the experimental data.[21,42,85,86,93,120] In general, the forward convolution approach is not limited to cylindrically symmetric distributions and may be used to analyze images from different experimental geometries. It has been successfully applied for the photodissociation of many molecular systems. The forward convolution scheme involves projection of the three-dimensional intensity distribution $I(\theta, \phi, r)$ onto the detector plane. Calculating the images corresponding to certain dissociation mechanisms, one can obtain a set of the *basis images*, which are then used for determination of the anisotropy parameters through some fitting procedure.[21,42] By way of example, we illustrate the $K = 2$ basis images for both experimental geometries in Figure 5. In principle, all even ($K = 2, 4$) and odd ($K = 1, 3$) rank anisotropy parameters can be accurately determined following this procedure, which sometimes needs a sophisticated mathematical manipulation.[77,85] Most analysis of $\mathbf{v}-\mathbf{J}$ correlation data assumed a separability $I(\theta, \phi, r) = f(\theta, \phi)g(r)$, where the function $g(r)$ describes the radial dependence of the three-dimensional distribution and r is the length of the photofragment radius vector, $r = v\tau$, where v is the photofragment velocity and τ is the flight time of the ions. However, in general, each of the anisotropy parameters will depend on recoil speed, so that such a separation will not be valid. An important modification of this approach has been recently suggested by Bass and co-workers[115] that involves analysis of the Fourier moments of images measured in different experimental geometries.

Very promising experimental procedures are now emerging that allow a 2D slice through the three-dimensional distribution to be obtained directly.[122–124] In this method, only the photofragments initially recoiling in the plane

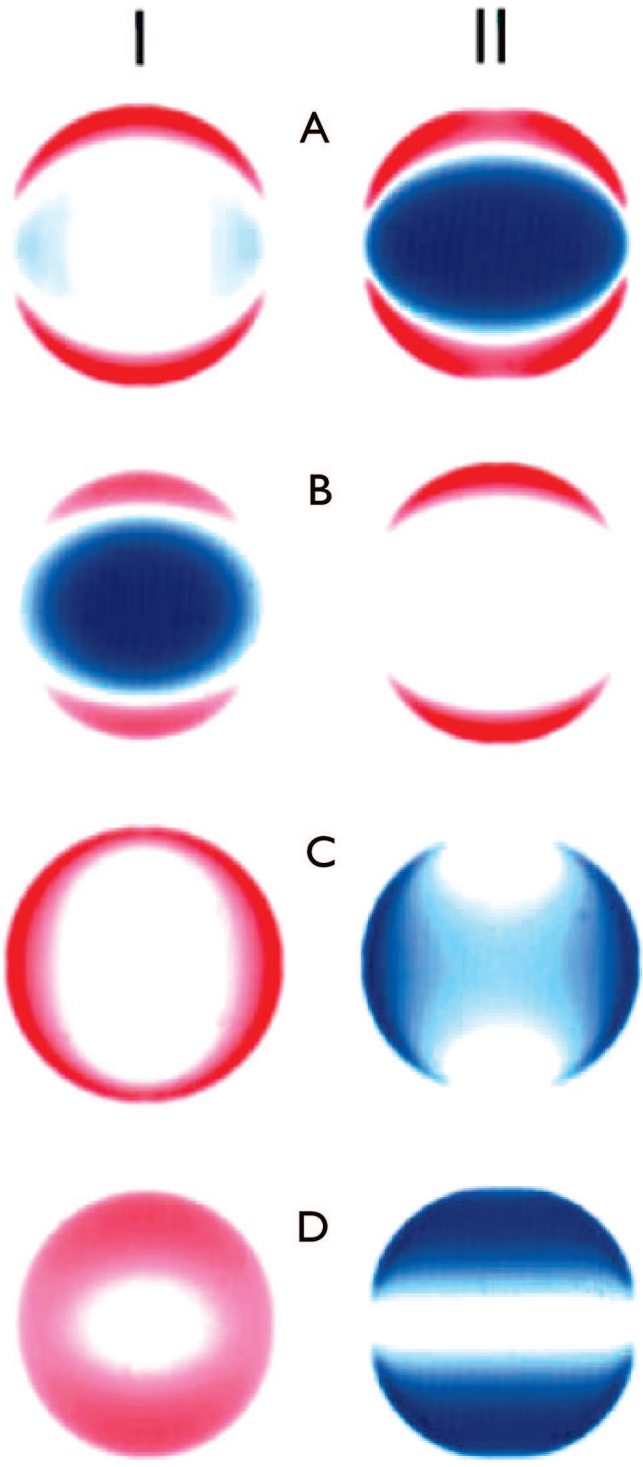

Figure 5. Alignment basis images adapted from ref 42: (A) incoherent perpendicular, (B) incoherent parallel, (C) coherent perpendicular, and (D) coherent parallel/perpendicular.

parallel to the imaging detector are detected. The 2D slice imaging does not need the convolution scheme, and therefore, it is more suitable for extracting the speed-dependent angular momentum polarization as described in the following section.[117]

2.2.4. 2D Slice Image Basis Functions

For the 2D slice imaging method, the experimental signals can be obtained from the general expressions in eq 60 with $\theta = {}^{\pi}/_{2}$, corresponding to the fragment moving in the plane parallel to the imaging detector. It is convenient to normalize the velocity-dependent experimental image over the total number of a certain velocity fragments in the slice, which can be obtained by integration of the expression in eq 64 over the azimuthal angle ϕ. In this case, the normalization factor N can be written as

$$N = \int_0^{2\pi} I_X\left(\frac{\pi}{2},\phi\right) + I_Y\left(\frac{\pi}{2},\phi\right) - \frac{1}{3}\left[I_R^z\left(\frac{\pi}{2},\phi\right) + I_L^z\left(\frac{\pi}{2},\phi\right)\right] d\phi = CP_0\int_0^{2\pi}\rho_{00}\left(\frac{\pi}{2},\phi\right) d\phi \quad (69)$$

which depends on the photolysis light polarization and on the parameter β.

With substitution of the state multipoles for the case of sliced images into eq 60, the explicit expressions for the image basis functions that can be used for determination of the anisotropy parameters from experimental images are given by the functions discussed in the following sections.[62]

2.2.4.1. Alignment. *Geometry I.* The photolysis light is linearly polarized along the Z axis

$$\frac{I_Z\left(\frac{\pi}{2},\phi\right) - I_Y\left(\frac{\pi}{2},\phi\right)}{\left\langle I_X\left(\frac{\pi}{2},\phi\right)\right\rangle + \left\langle I_Y\left(\frac{\pi}{2},\phi\right)\right\rangle + \left\langle I_Z\left(\frac{\pi}{2},\phi\right)\right\rangle} = \frac{1}{(1-\beta/2)}\left[\frac{C'P_2}{2P_0}\times\left\{(s_2+\alpha_2)(\cos 2\phi - 1) - \frac{1}{2}\eta_2(3+\cos 2\phi)\right\} + \frac{C''P_4}{12P_0}\{5(s_4+\alpha_4)(3+4\cos 2\phi - 7\cos 4\phi) + \sqrt{15}\eta_4(5+4\cos 2\phi + 7\cos 4\phi)\}\right] \quad (70)$$

Geometry II. The photolysis light is linearly polarized along the Y axis

$$\frac{I_Z\left(\frac{\pi}{2},\phi\right) - I_Y\left(\frac{\pi}{2},\phi\right)}{\left\langle I_X\left(\frac{\pi}{2},\phi\right)\right\rangle + \left\langle I_Y\left(\frac{\pi}{2},\phi\right)\right\rangle + \left\langle I_Z\left(\frac{\pi}{2},\phi\right)\right\rangle} = \frac{1}{(1+\beta/4)}\times\left[\frac{C'P_2}{2P_0}\left\{s_2(\cos 2\phi - 1) + \frac{\alpha_2}{2}(3\cos^2 2\phi - 4\cos 2\phi + 1) + \gamma_2 \sin^2 2\phi + \frac{\eta_2}{4}(\cos^2 2\phi + 4\cos 2\phi + 3)\right\} + \frac{C''P_4}{12P_0}\left\{\frac{5}{2}(3+4\cos 2\phi - 7\cos 4\phi)(2s_4 + (3\cos 2\phi - 1)\alpha_4) - 2\sqrt{30}\gamma_4(5+12\cos 2\phi + 7\cos 4\phi)\sin^2\phi - \frac{\sqrt{15}}{4}\eta_4(14+25\cos 2\phi + 18\cos 4\phi + 7\cos 6\phi)\right\}\right] \quad (71)$$

where $C' = \sqrt{5}V_2(j)/4\pi$, $C'' = 3V_4(j)/32\pi$, while the terms $V_2(j)$ and $V_4(j)$ are defined after eq 8.

2.2.4.2. Orientation. *Geometry III.* The photolysis (right circularly polarized) and probe light (right or left circularly polarized) propagate along the X and $-X$ axes, respectively

$$\frac{I_R^X\left(\frac{\pi}{2},\phi\right)-I_L^X\left(\frac{\pi}{2},\phi\right)}{\left\langle I_Z\left(\frac{\pi}{2},\phi\right)\right\rangle+\left\langle I_Y\left(\frac{\pi}{2},\phi\right)\right\rangle-\frac{1}{3}\left[\left\langle I_R^X\left(\frac{\pi}{2},\phi\right)\right\rangle+\left\langle I_L^X\left(\frac{\pi}{2},\phi\right)\right\rangle\right]}=$$

$$-\frac{3\sqrt{3}}{(1-\beta/8)\pi}\left[\frac{P_1^c}{P_0}\left\{\alpha_1\cos^2\phi+\frac{\gamma_1}{2}\sin^2\phi\right\}+\frac{P_3^c}{P_0}\frac{\sqrt{7}V_3(j)}{2\sqrt{3}}\times\right.$$

$$\left.\left\{\alpha_3\cos^2\phi(5\cos^2\phi-3)+\gamma_3\frac{\sqrt{6}}{4}\sin^2\phi(5\cos^2\phi-1)\right\}\right] \quad (72)$$

Geometry IV. The photolysis and probe light couterpropagate along the *X* axis with the photolysis light linearly polarized at 45° to the detector plane and the probe light circularly polarized

$$\frac{I_R^X\left(\frac{\pi}{2},\phi\right)-I_L^X\left(\frac{\pi}{2},\phi\right)}{\left\langle I_Z\left(\frac{\pi}{2},\phi\right)\right\rangle+\left\langle I_Y\left(\frac{\pi}{2},\phi\right)\right\rangle-\frac{1}{3}\left[\left\langle I_R^X\left(\frac{\pi}{2},\phi\right)\right\rangle+\left\langle I_L^X\left(\frac{\pi}{2},\phi\right)\right\rangle\right]}=$$

$$-\frac{3\sqrt{3}}{(1-\beta/8)\pi}\frac{\sin^2\phi}{2}\left[\frac{P_1^c}{P_0}\gamma'_1+\frac{P_3^c}{P_0}\sqrt{14}V_3(j)\times\right.$$

$$\left.\left\{\frac{\gamma'_3}{4}(5\cos^2\phi-1)+\eta_3\cos^2\phi\right\}\right] \quad (73)$$

where the term $V_3(j)$ is given after eq 8.

3. Experiment: Imaging Probes of Orbital Polarization

3.1. Experimental Approach

Although many variations of the imaging approach have been developed over the years, the essential features, summarized in Figure 6, are largely unchanged from the original report from Chandler and Houston.[7] A pulsed molecular beam is skimmed and enters into an interaction chamber where it is crossed by photolysis and probe lasers. Usually the molecular beam is directed along the axis of the TOF mass spectrometer toward a position-sensitive microchannelplate (MCP) detector coupled to a phosphor screen. Neutral products produced by the photolysis laser are promptly ionized by an appropriate REMPI excitation scheme, and the ions are accelerated down the flight tube to strike the detector. The detector is gated using a high-voltage pulse so that it only responds to the mass of interest. The ion impacts generate fluorescent spots on the phosphor screen, and these are viewed by a CCD camera and sent to a computer for digitization and integration.

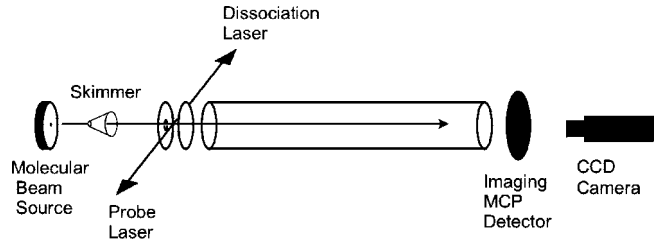

Figure 6. Schematic configuration for a typical ion imaging experiment.

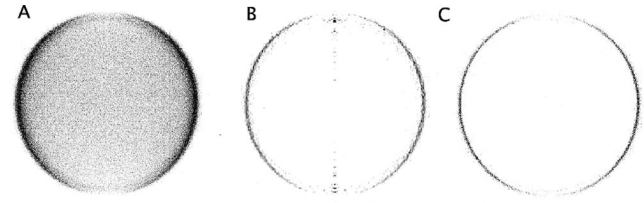

Figure 7. (A) Two-dimensional projected image of Cl from Cl_2 dissociation. (B) Reconstructed slice from inverse Abel transform of image in A. (C) DC sliced image analogous to B directly obtained in experiment.

Two significant advances in imaging methods have taken place in the past decade. The first of these, "velocity map imaging", was introduced by Eppink and Parker in 1997.[125,126] In this approach, the grids of the traditional Wiley−McLaren TOF mass spectrometer are replaced by ion lenses. By adjustment of the potentials, a condition is readily found that achieves a high degree of pure velocity focusing, that is, ions are focused onto a point on the detector that depends only on their velocity in the plane parallel to the detector and is largely independent of their birth position. This approach led immediately to a 5-fold improvement in velocity resolution because the finite size of the interaction volume relative to the detector had limited the velocity resolution to 10% or so.

The second significant advance was the development of "slicing" techniques mentioned in section 2.2.4.[122−124] As seen in Figure 7A, in traditional imaging experiments, the detected image actually represents the 2-D projection of the 3-D fragment distribution. For experiments with cylindrical symmetry, the 3-D distribution may be recovered using a tomographic algorithm; the inverse Abel transform is one commonly used approach. However, this inversion can reduce the signal-to-noise and, in many cases, compromise the velocity resolution. Furthermore, for the vector correlation studies presented here, one often employs geometries lacking an axis of symmetry. For these experiments, reconstruction techniques are not suitable, and forward convolution methods have been employed in the past. However, these are of limited use in the analysis of complex velocity-dependent signals in projected images resulting from polyatomic dissociation. Slicing approaches clearly provide the solution. By using delayed extraction or very low initial acceleration fields to stretch the ion cloud along the TOF axis (see Figure 8C and D), the detector may be gated to select only the central slice of the image, that is, only those fragments with no velocity component along the flight axis. For the case of cylindrical symmetery, this is equivalent to measuring the Abel-tranformed image directly.

For crossed-laser polarization geometries, slicing represents a powerful means of revealing the speed-dependent polarization. This is illustrated in Figure 9 for ozone photodissociation at 248 nm. Figure 9A shows the difference image for the traditional projected (i.e., unsliced) case, while Figure 9C shows the equivalent sliced image. The unsliced basis image representing the coherent γ'_1 contribution for a single recoil speed is shown in Figure 9B for comparison. The speed-dependent structure and, in particular, the change of sign in the inner ring could easily be lost in any attempt to analyze the unsliced image.

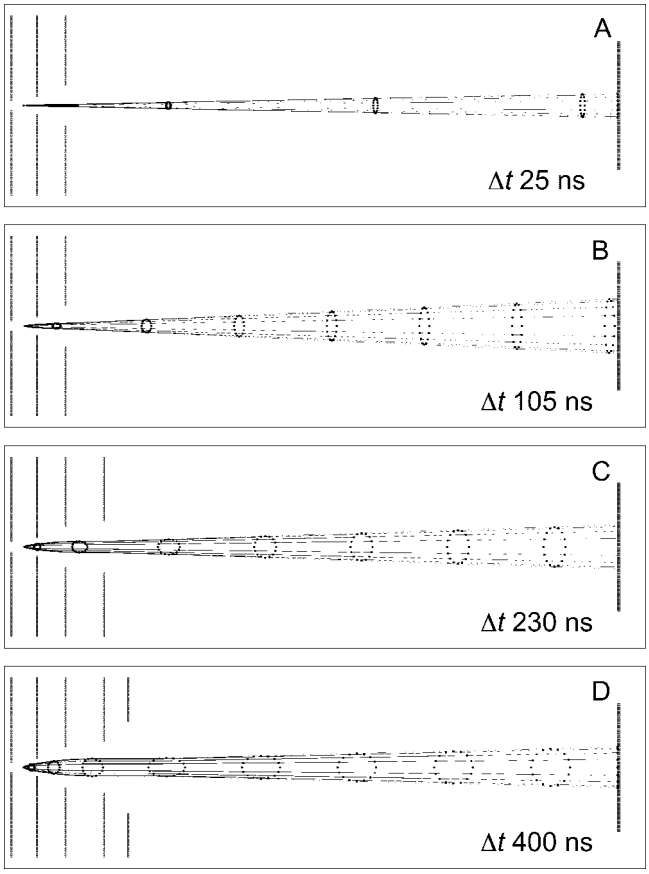

Figure 8. Ion optics configurations and ion trajectories showing sample ion clouds at 1 μs intervals. (A) Normal velocity mapping with high (2.5 kV) repeller potential. (B) Normal velocity mapping with low (0.5 kV) repeller potential. (C) 3-lens DC slicing with 0.5 kV repeller potential. (D) 4-lens DC slicing with 0.5 kV repeller potential. Temporal stretching of ion cloud is indicated for each condition.

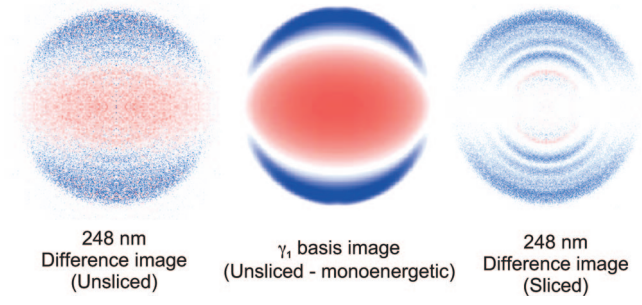

Figure 9. Orientation difference images for O(^1D) from ozone dissociation at 248 nm: (A) unsliced, (B) relevant basis image for single recoil speed, and (C) DC sliced image analogous to A.

The probe of angular momentum polarization relies heavily on the use of a variety of polarization configurations. In effect, one must control arbitrary polarization of both photolysis and probe lasers, and the nature of the anisotropy parameter to be measured (or underlying dynamics of interest) will determine the choice of experimental geometry and polarization of photolysis and probe lasers. With the use of coaxial or orthogonal photolysis and probe laser beams propagating perpendicular to the flight axis, along with sliced imaging, nearly all parameters and their recoil speed dependence may be measured in isolation from other interfering signals.

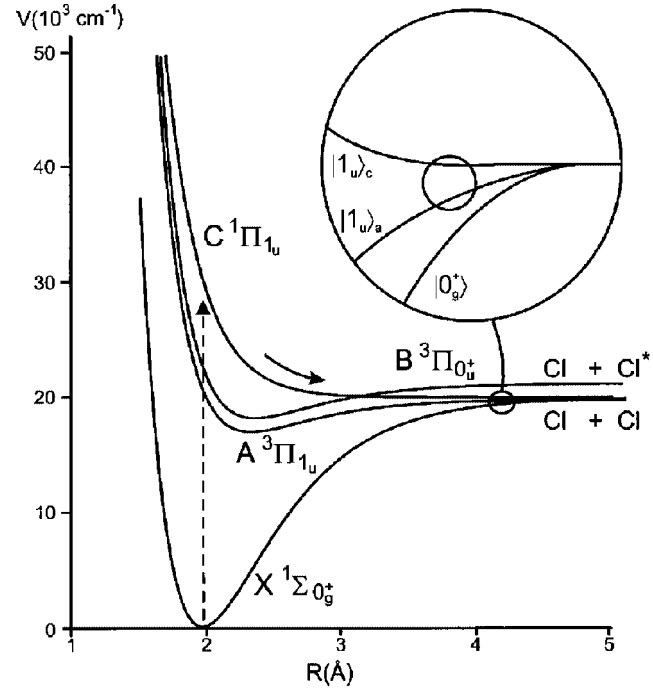

Figure 10. Schematic potential energy curves for Cl_2.

We now turn to an overview of experiments probing atomic angular momentum polarization in photodissociation. The focus will be on ion imaging experiments, but results obtained using other techniques will be considered when relevant to the discussion.

3.2. Applications: Diatomics

3.2.1. Dihalogens

3.2.1.1. Cl_2. Photofragment orbital polarization in molecular chlorine photodissociation is perhaps the most thoroughly characterized of any molecule. It has been examined by numerous groups, with detection of both orientation and alignment, at a range of wavelengths and using a variety of techniques. Furthermore, it was the first system in which the coherent contribution to the photofragment angular momentum polarization was identified and isolated from incoherent contributions.[22] It was used[42] as the prototype for application of the analysis using the laboratory frame anisotropy parameters introduced by Picheyev et al.[33] and was among the first systems investigated by Zare, Rakitzis, and co-workers,[55,82] using ion time-of-flight, to obtain molecular frame alignment measurements.

In the near-ultraviolet, Cl_2 may be excited from the ground $X(^1\Sigma_g^+)$ state to the B ($^3\Pi_{0+u}$) state via a parallel transition or to the C($^1\Pi_u$) state via a perpendicular transition (see Figure 10). The latter state correlates asymptotically to two ground-state Cl($^2P_{3/2}$) chlorine atoms (Cl), while the former correlates to production of one ground-state atom and one spin−orbit excited Cl($^2P_{1/2}$) atom (Cl*). Alignment in the Cl atom was initially reported by Qian and co-workers[54] in one of the first studies to describe **v**−**j** correlation in atomic photofragments.[54] Their study of Cl_2 photodissociation at 355 nm, where the C state excitation dominates, relied on the sensitivity of ion time-of-flight profiles to probe laser polarization. The results were accompanied by an analysis that assumed purely adiabatic dissociation and neglected

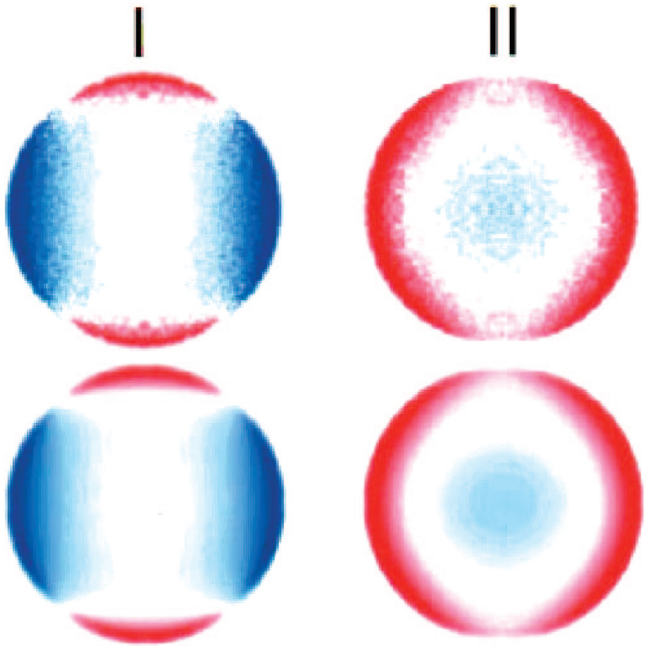

Figure 11. Cl alignment difference images obtained from dissociation of Cl_2 at 355 nm for the geometry (I or II) indicated. Top images: Experiment. Bottom images: Simulation. Reused with permission from A. S. Bracker et al. *J. Chem. Phys.*, **110**, 6749 (1999). Copyright 1999, American Institute of Physics.

coherent contributions. Although constrained by these assumptions, their results are broadly consistent with many subsequent measurements.

The first treatment of orbital polarization in Cl_2 photodissociation based upon the quantum mechanical formalism of Siebbeles et al. was reported by Bracker et al. using the anisotropy parameters introduced by Picheyev and co-workers.[22,42] Using ion imaging, they measured the alignment of the Cl atom, also following excitation to the C state at 355 nm, by means of two distinct probe transitions. Their results, shown in Figure 11, were obtained using the forward convolution approach discussed in section 2.2.3 to fit the difference image with the four basis images in Figure 5. They determined the contributions of the four anisotropy parameters to the alignment and identified both incoherent perpendicular and coherent perpendicular contributions to the alignment. For the case of a pure perpendicular transition these can be readily expressed in terms of the anisotropy parameters and the underlying dynamical functions

$$A_{20}^{\mathrm{mol}} = 10\alpha_2 = \mathbf{a}_0^2(\perp) = \frac{4}{\sqrt{5}}\frac{f_2(1,1)}{f_0(1,1)} \qquad (74)$$

$$A_{22}^{\mathrm{mol}} = -\frac{5\eta_2}{\sqrt{6}} = \mathbf{a}_2^2(\perp) = -\frac{2}{\sqrt{5}}\frac{f_2(1,-1)}{f_0(1,1)}$$

where α_2 and η_2 are the anisotropy parameters, A_{20}^{mol} and A_{22}^{mol} are molecular frame state multipoles, and $\mathbf{a}_0^2(\perp)$ and $\mathbf{a}_2^2(\perp)$ are the corresponding molecular frame polarization parameters described in section 2.1.8. It was shown in ref 42 that adiabatic dissociation from the *C* state should give rise to a contribution to the Cl atom alignment corresponding to *incoherent* excitation of $\Omega = \pm 1$ components of the *C* state but not to any coherent contribution. This is seen by calculation of the values of the corresponding dynamical functions with eq 11 using the coefficients $\mathcal{T}^{n\Omega}_{j_A\Omega_A j_B\Omega_B}$ of the two lowest molecular states of 1_u symmetry corresponding to the quadrupole−quadrupole interaction between the fragments.[42] This yields

$$f_0(1,1) = \frac{1}{2}, \quad f_2(1,1) = -\frac{(1-w)}{2\sqrt{5}}, \quad f_2(1,-1) = -\frac{\sqrt{w(1-w)}\cos\Delta\varphi}{\sqrt{5}} \qquad (75)$$

Here, the term *w* is simply the probability of possible nonadiabatic transitions between the $C^1\Pi_{1u}$ and $A^3\Pi_{1u}$ states. In the absence of nonadiabatic transitions, $w = 0$ and the coherent $f_2(1, -1)$ dynamical function vanishes. The incoherent alignment is proportional to the probability of following the adiabatic path. The non-zero value of the coherent perpendicular alignment provides direct insight into the nature of the nonadiabatic dynamics. In this case, $w = r_A^2$, that is, the square of the *A* state **T** matrix element amplitude. The coherent contribution can be seen as an interference between the *A* and *C* state paths resulting from a nonadiabatic transition, so the coherent alignment reflects both the amplitudes of the *C* and *A* state **T** matrix elements (proportional to $\sqrt{w}$ and $\sqrt{(1-w)}$) and the phase difference, $\Delta\varphi = \varphi_C - \varphi_A$, between them.

Results for Cl alignment obtained by different groups[42,82,115,127] over a range of wavelengths are compiled in Table 9. Experimental values for the molecular frame alignment components A_{20}^{mol} and A_{22}^{mol} are shown, along with the nonadiabatic transition probability, *w*, and the phase difference, $\Delta\varphi$. The qualitative agreement is quite good; in particular, the ratio of the incoherent to coherent contributions is fairly consistent across all measurements. The range of experimental approaches likely precludes a close comparison across wavelengths; certainly no strong wavelength dependence is suggested in these studies. The importance of nonadiabatic transitions following excitation to the *C* state is now widely recognized despite diverging interpretations in the earlier reports.

Alexander et al.[57] have measured orientation of the Cl and Cl* product, following photodissociation of Cl_2 at 310 and 330 nm using circularly polarized light. They observed substantial incoherent orientation of the Cl atom and no coherent contribution, and this was simply associated with adiabatic dissociation via the *C* state. The results for the Cl* product were quite distinct. Production of spin−orbit excited Cl* atoms in this wavelength region is a minor process (0.01) but shows complex dynamics: the β parameter value of −0.12 implies a mixed transition of nearly equal parallel and perpendicular composition. The most significant observation for Cl* was incoherent orientation of opposite sign to that of the Cl product, implying helicity opposite to the sense of the photolysis photon. Simple theoretical considerations show that direct *B* state excitation would not result in orientation in either Cl or Cl* products, so nonadiabatic coupling to higher states of 1_u symmetry must be invoked. Correlation arguments indicate that only the $1_u^{(3)}$ state will give rise to incoherent orientation of the correct sign, so nonadiabatic transition from the *C* state to the $1_u^{(3)}$ state was inferred to account for the incoherent orientation. Furthermore, the deviation of the observed orientation from the limiting value predicted for dissociation via the $1_u^{(3)}$ state led Alexander et al. to attribute an additional fraction to subsequent nonadiabatic transition from the $1_u^{(3)}$ state to $1_u^{(4)}$. The effect of this is to cancel a fraction of the observed orientation, as the latter is expected to have the opposite sign. These arguments were reinforced by theoretical calculations

Table 9. Alignment Parameters, A_{20}^{mol} and A_{22}^{mol}, Probability of Nonadiabatic Transition w between the $C^1\Pi_{1u}$ and $A^3\Pi_{1u}$ States in Molecular Chlorine, and the Corresponding Phase Difference $\Delta\theta$[a]

	Bracker et al.[42]	Kitsopoulos et al.[127]	Rakitzis et al.[55]	Bass et al.[115]
	355 nm	355 nm	320 nm	308 nm
A_{20}^{mol}	−0.35(4)	−0.50(10)	−0.50(10)	−0.62(9)
A_{22}^{mol}	−0.15(4)	−0.30(10)	−0.32(6)	−0.26(7)
w	0.56(5)	0.38(13)	0.38(13)	0.23(11)
$\Delta\theta$	112°	141°	145°	141°

[a] The values w and $\Delta\theta$ have been determined from the experimental data of Bracker et al.,[42] Rakitzis et al.,[55] Rakitzis and Kitsopoulos,[127] and Bass et al.[115] using eqs 74 and 75. Adapted from ref 27.

of the nonadiabatic couplings among all relevant surfaces obtained using a Rosen−Zener−Demkov noncrossing model; only radial derivative coupling was found to be important. The results were consistent with the measured orientation values, as well as with the original alignment studies showing substantial nonadiabatic coupling from the C state to the A state.

3.2.1.2. Br_2 and I_2. Photofragment orbital polarization in molecular bromine photodissociation was studied by Rakitzis and Kitsopoulos[127] with slicing imaging at 355 nm. Contrary to the case of molecular chlorine, they reported adiabatic dissociation of Br_2 through the single $C^1\Pi_{1u}$ state.

An experimental study of photofragment orbital polarization in molecular iodine has recently been reported by Chestakov et al.[128] who used a combination of velocity map imaging and slicing techniques. Chestakov et al. measured the product recoil anisotropy and angular momentum polarization for the photodissociation processes $I_2 + h\nu \rightarrow I(^2P_{3/2}) + I(^2P_{3/2})$ and $I_2 + h\nu \rightarrow I(^2P_{3/2}) + I(^2P_{1/2})$ in the 450−510 nm laser wavelength region using linearly polarized photolysis and probe laser light. The former channel is produced predominantly via perpendicular excitation to the $^1\Pi_u$ state, and the latter is predominantly parallel, via the $B^3\Pi(0_u)^+$ state. In both cases, mostly adiabatic dissociation has been observed, which produces electronically aligned iodine atoms in the $m = {}^1/_2$ states with respect to the recoil direction.

This result is similar to the Br_2 case, where mainly adiabatic dissociation has also been observed,[127] but differs from the Cl_2 case where large nonadiabatic transition probabilities have been determined by several groups.[42,82,115,127] The theoretical analysis of the nonadiabatic interactions in halogen molecules has recently been reported by Asano and Yabushita[129] using a semiclassical method. According to their analysis, the probability of nonadiabatic transitions is influenced mainly by the size of the atomic orbitals and the relative nuclear velocity. They concluded that the heavier dihalogens with larger spin−orbit splitting show more adiabatic behavior, consistent with the experimental results for the sequence Cl_2, Br_2, and I_2.

3.2.2. Interhalogens XY

3.2.2.1. ICl. Orbital polarization in ICl photodissociation deserves special mention and is highlighted here even though the results have all been obtained with nonimaging methods. In compelling studies, Zare and co-workers used an ion time-of-flight technique to measure the orientation of the Cl atom following photolysis of ICl with linearly polarized light at a range of visible wavelengths.[24,25,82] These measurements are sensitive to a single parameter, $\mathrm{Im}[\mathbf{a}_1^1]$ in the Rakitzis-Zare notation (which is related to the γ_1' anisotropy parameter). This parameter reflects coherent excitation of parallel and perpendicular transitions induced by linearly polarized light.

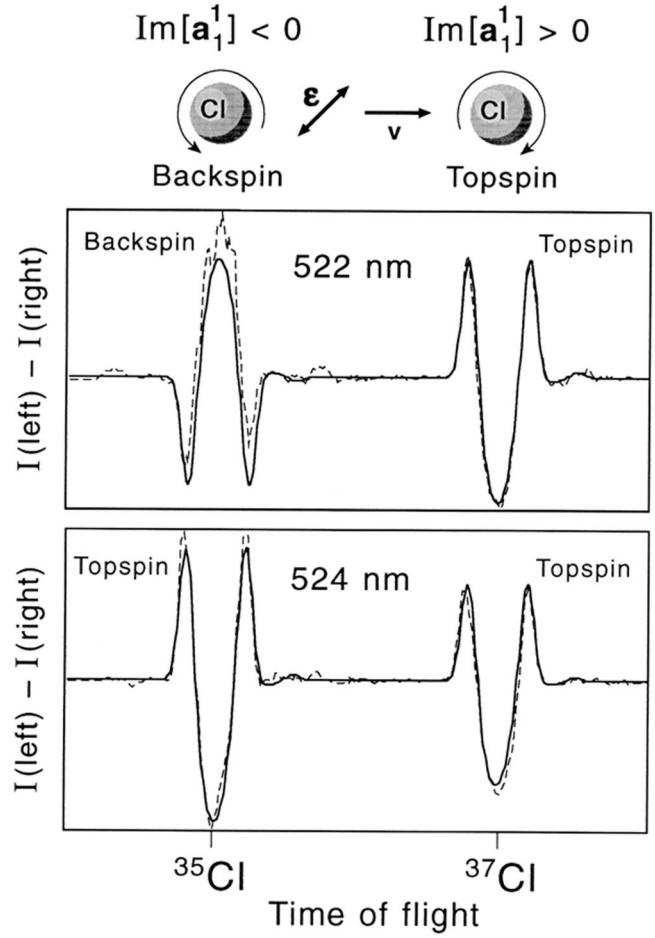

Figure 12. Core-sampled ion time-of-flight difference spectra for Cl product of ICl photodissociation at the indicated wavelength. The experiment probes the molecular frame $Im[\mathbf{a}_1^1]$ parameter. From Rakitzis et al., *Science* 281:1346 (1998). Reprinted with permission from AAAS.

Time-of-flight difference profiles are shown in Figure 12 for both ^{35}Cl and ^{37}Cl at two photolysis wavelengths. The terms backspin and topspin refer to the direction of the angular momentum vector relative to the plane containing the photolysis laser polarization direction and the time-of-flight (internuclear axis) direction. These spectra are quite revealing: Clearly, the difference profiles change dramatically with a small change in wavelength. Even more remarkable is the strong dependence on the particular Cl isotope detected, seen clearly in the 522 nm TOF profile. By making analogous measurements from 480 to 560 nm for both ^{35}Cl and ^{37}Cl, the spectra in Figure 13 are obtained. Oscillations in the $Im[\mathbf{a}_1^1]$ parameter are observed, and these are shifted in wavelength for the mass 37 isotope relative to that of mass 35.[25]

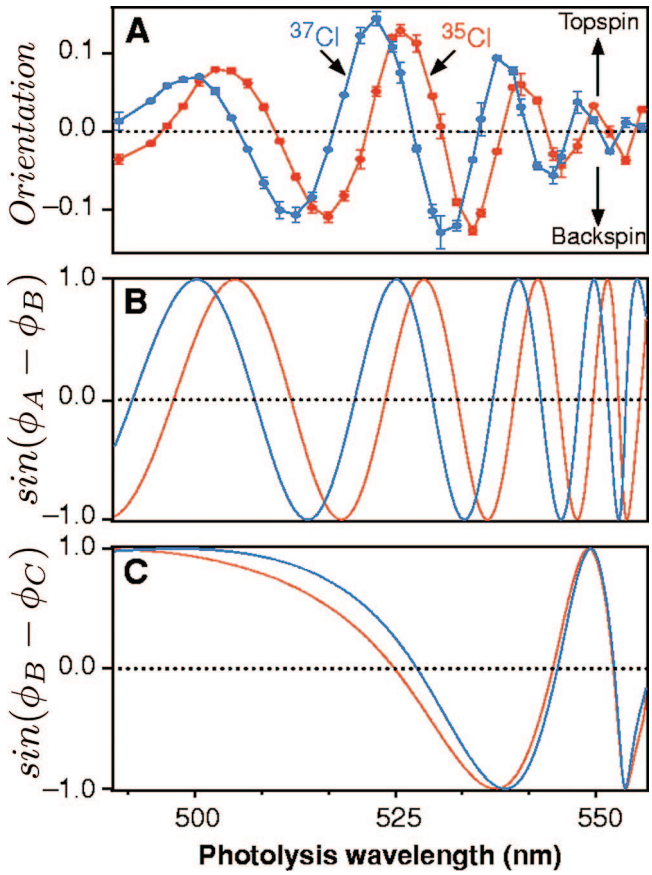

Figure 13. Orientation for ^{35,37}Cl from ICl photodissociation by linearly polarized light at a range of wavelengths: (a) experimental results, (b) theoretical model calculations based on phase difference between *A* and *B* potential curves, and (c) theoretical model calculations based on phase difference between C and B potential curves. From Rakitzis et al., *Science* 281:1346 (1998). Reprinted with permission from AAAS.

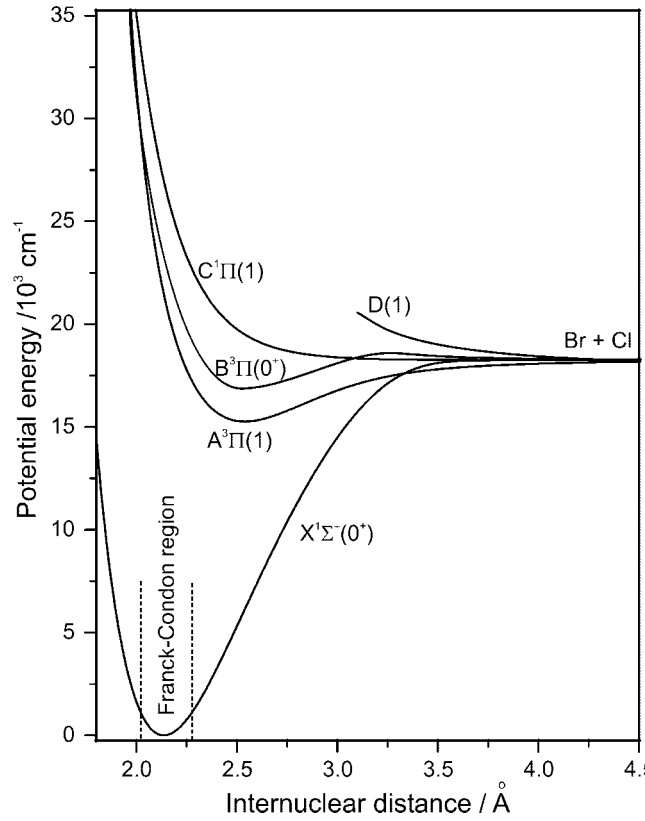

Figure 14. Potential energy curves for the five lowest electronic states involved in the production of Cl($^2P_{3/2}$) atoms from the photodissociation of BrCl (from ref 132) The curves for the *X*, *A*, *B*, and *C* states are based on the accurate empirical curves of Beckert et al.;[131] the *D*-state curve is schematic. Reproduced with permission from *Mol. Phys.* (2007) **105** 885. Copyright 2007, Taylor and Francis.

These observations have been rationalized in terms of an asymptotic difference in the scattering phase arising from coherent dissociation on two distinct potentials. The instantaneous de Broglie wavelength is inversely proportional to the photofragment linear momentum, $\lambda = h/p$, and the phase difference for dissociation along the two curves reflects the accumulation of this difference. Simply stated, the different potentials exhibit different characteristic scattering wave functions with different asymptotic phase shifts. A coherent sum of the amplitudes along the two trajectories will show interference varying as the sine of the phase difference for the two trajectories. Furthermore, for the two different isotopes, the relative momenta scale as the square root of the ratio of the reduced masses in the dissociation event, yielding roughly a 2% higher frequency for the ^{37}Cl wave function, and a corresponding change in the phase difference for the heavier isotope.

The results have been modeled assuming dissociation via the *A* and *B* or the *B* and *C* excited states of ICl (Figure 13B and C, respectively) for both isotopes. Simulated spectra obtained from the model are shown, along with the overall wavelength dependence of the orientation. The results obtained assuming coherent dissociation via the *A* and B states show a nice agreement with the experiment, and the isotope dependence is well reproduced. The wavelength dependence of the $Im[\mathbf{a}_1^{(1)}]$ parameter is quite sensitive to the two potentials, just as quantum interference effects in scattering have been used to probe details of the potentials for many years.

In addition to the $K = 1$ parameter measured for ICl discussed above, Rakitzis et al. have measured the recoil anisotropy (β) and alignment at a range of visible wavelengths.[82] The β parameter varied monotonically from near-limiting perpendicular at long wavelength (560 nm) to near-limiting parallel at short wavelength (490 nm). The rank $K = 2$ alignment was measured over a narrower range from 500 to 535 nm. They found incoherent contributions to the alignment that were largely independent of photolysis wavelength. However, the coherent $Re[\mathbf{a}_1^{(2)}(\parallel,\perp)]$ contribution showed oscillations with photolysis wavelength reminiscent of that seen for the $Im[\mathbf{a}_1^{(2)}(\parallel,\perp)]$ parameter, and a similar dependence on Cl isotope was also observed. Rakitzis et al. argued that the β value reflected the changing contributions of the perpendicular *A* state (long wavelength) and parallel *B* state (short wavelength), while the incoherent alignment revealed that the dynamics within each band was wavelength invariant. The coherent alignment fluctuates significantly with photolysis wavelength, but this is a manifestation of interference rather than changing dynamics.

3.2.2.2. BrCl. The photodissociation dynamics of BrCl at a variety of visible and near-UV wavelengths have been the subject of extensive study in the Bristol laboratory using a high resolution photofragment velocity map imaging spectrometer.[77,116,130,131] Figure 14 shows the ground $X^1\Sigma^+_{0+}$ state potential and a several excited-state potentials $A^3\Pi_1$, $B^3\Pi_{0+}$, $C^1\Pi_1$, and $D(1)$ that are all involved in the photolysis resulting in the ground-state chlorine and bromine photofragments.

Wavepacket calculations of the dissociation dynamics, following photoexcitation to the $A^3\Pi_1$, $B^3\Pi_{0+}$, and $C^1\Pi_1$ states, with allowance for nonadiabatic dynamics at the avoided crossing between the $B^3\Pi_{0+}$ state and a further $\Omega = 0^+$ state, were used to optimize the shapes of the potential energy curves[131] and successfully reproduced all wavelength-dependent measurements of branching ratios and photofragment translational anisotropies. The broad absorption spectrum of BrCl in the visible region of the spectrum was deconvoluted into overlapping regions of excitation to these three dissociating states.

Detailed alignment measurements have also been reported by Wouters and co-workers[116] at four different wavelengths in the range 425−485 nm using linear photolysis laser polarizations. Non-zero values of all alignment anisotropy parameters were reported, allowing quantification of the angular momentum orientation and alignment of the Cl ($^2P^0_{3/2}$) fragments. The parameter values were found to vary significantly as the photolysis wavelength. The alignment-free recoil anisotropy parameter β (see eq 64) was determined as a function of parent excitation wavelength. This is of practical importance because the Cl fragment angular distributions show little anisotropy ($\beta \approx 0$) for photolysis in the range $450 < \lambda_{phot} < 550$ nm, and its experimentally measured value is masked by the alignment effects. Later, Smolin and co-workers[77] reported determination of the complete set of the orientation parameters ($K = 1, 3$) at 467 nm using linear and circular photolysis light polarization. Both incoherent and coherent contributions to the orientation and alignment are identified, with both simultaneous parallel and perpendicular excitations to the $B^3\Pi_{0+}$ and $C^1\Pi_1$ states and excitations to the $\Omega = \pm 1$ components of the C state contributing to the latter.

The interpretation in BrCl is much more complex than in Cl_2 because of different adiabatic correlations of the heteronuclear molecule. Pure adiabatic dissociation via either the B or C state is expected to give no alignment, so nonadiabatic transitions must be invoked to account for the observations. A number of possible mechanisms were identified that could contribute to the observed orientation and alignment. These include incoherent excitation of the B and C states, followed by nonadiabatic transitions to the X and A or D states, respectively. The coherent parallel/perpendicular contribution could arise from coherent excitation of the B and C states, followed by nonadiabatic transition of the former to the X state or the latter to the D state. Finally, the coherent perpendicular contribution could be associated with coherent excitation of the two components of the C state, followed by nonadiabatic transition to the A or D states.

The non-zero values of the anisotropy parameters are indicative of nonadiabatic dissociation dynamics. These values also depend on asymptotic radial phase shifts between dissociative fluxes on the PE curves correlating to the same atomic limits and thus, in principle, provide a means of determining *all* transition amplitudes and phases. However, the total number of the experimentally determined parameters in case of BrCl is large (13), which makes the inversion problem quite cumbersome. This problem has recently been solved by Smolin and co-workers[132] who demonstrated how the anisotropy parameters are intimately connected to the **T**-matrix amplitudes and phases via expressions that are generally applicable to diatomic interhalogen molecules and carried out the inversion of the experimentally measured anisotropy parameters for BrCl at 467 nm. The amplitudes and phases derived from the analysis are listed in Table 10. These values were verified by using them to recalculate the experimental anisotropy parameters.[132] The measured values of the anisotropy parameters obtained from the fitted **T**-matrix element amplitudes and phases agreed reasonably well with the experimental measurements.

Table 10. Amplitudes and Phases of the Nuclear Wavefunctions on the $X^1\Sigma^+_{0+}$, $A^3\Pi_1$, $B^3\Pi_{0+}$, $C^1\Pi_1$, and $D(1)$ States for 467 nm Photodissociation of BrCl to Form Cl($^2P^0_{3/2}$) Atoms[a]

state (n)	r_n	$\varphi_n - \varphi_X$ (radians)
$X^1\Sigma^+_{0+}$	0.395	0
$A^3\Pi_1$	0.325	−2.64
$B^3\Pi_{0+}$	0.0120	−0.224
$C^1\Pi_1$	0.082	0.789
$D(1)$	0.201	2.49
Br + Cl*	0.820	

[a] The last line represents the experimental value of the amplitude corresponding to population of the Br + Cl* channel.[131] Adapted from ref 132.

The data in Table 10 contain important new information about the photodissociation dynamics of BrCl which has not been considered previously. These results yielded quantitative information on all amplitudes and phases involved in the photolysis. In particular, there is substantial accumulation of dissociative flux on the $X^1\Sigma^+_{0+}$ and $D(1)$ states because of nonadiabatic dynamics. The fluxes on the B and C states, which are strongly excited at 467 nm, are significantly depleted by transfer to the X and A, D states, respectively. All the scattering phase differences in Table 10 are large in magnitude. If interpreted in the quasiclassical approximation,[51] these phases in general contain two contributions. One of these contributions is related to the coherence between states of different symmetry ($\Delta\Omega = \pm 1$). The associated phase shift is mostly caused by the nuclear motion on PE curves of different shapes in the adiabatic region and can be associated with the elastic scattering phase shift. The other contribution is a dynamical phase shift between states of the same symmetry and is the result of electronic and nuclear motion in the vicinity of the nonadiabatic interaction regions that occur in the locality of quasi (i.e., partially avoided) crossings and at large internuclear separations. Both contributions to the phases are important for BrCl at wavelengths in the visible and near-UV regions of the spectrum. These results illustrate the idea of the complete experiment for a relatively complicated diatomic molecule. Note that although high-quality diabatic potentials for BrCl are available,[131] the couplings between the potentials are not known, and thus wavepacket propagation methods cannot yet be used to compute either the anisotropy parameters or full **T**-matrix elements incorporating nonadiabatic dissociation dynamics for direct comparison with experimental results.

3.2.3. HX

3.2.3.1. HF. The hydrogen halides likewise represent an important class of molecules in the study of angular momentum polarization in photodissociation. A theoretical study of polarization in hydrogen fluoride photodissociation by Balint-Kurti and co-workers was the first case in which experimentally measurable anisotropy parameters (in principle) were directly related to photofragment **T**-matrix elements that were calculated rigorously from a pure quantum mechanical theory.[26] The general form of the photofragmentation **T**-matrix elements in terms of their amplitudes for different dissociation channels and the quantum mechan-

ical phase shifts between these channels is given in eq 16. In case of HX, the relationship between the dynamical functions describing the production of the halogen ground state $^2P_{3/2}$ photofragments with angular momentum polarizations of the ranks $K = 0,..., 3$ and the amplitudes and phase shifts is as follows

$$f_0(1,1) = \frac{1}{2}(1 - p_2) \tag{76}$$

$$f_1(1,1) = \frac{1}{2\sqrt{15}}(3 - 2p_1 - 3p_2)$$

$$f_2(1,1) = \frac{1}{2\sqrt{5}}(1 - 2p_1 - p_2)$$

$$f_3(1,1) = \frac{1}{2\sqrt{35}}(1 - 4p_1 - p_2)$$

$$f_2(1,-1) = \frac{\sqrt{2}}{\sqrt{5}}\sqrt{(1 - p_1 - p_2)p_1}\cos\Delta\varphi$$

$$f_3(1,-1) = -i\frac{\sqrt{2}}{\sqrt{7}}\sqrt{(1 - p_1 - p_2)p_1}\sin\Delta\varphi$$

where p_2 is the branching fraction for producing the excited halogen ($^2P_{1/2}$) state, p_1 is the probability of nonadiabatic transitions from the singlet $^1\Pi_1$ to the triplet $^3\Pi_1$ molecular excited state, and $\Delta\varphi$ is the phase shift between the photofragmentation **T**-matrix elements for the $^3\Pi_1$ and the $^1\Pi_1$ states. Equation 76 is written with the assumption that only the singlet $^1\Pi_1$ molecular state can be optically excited from the ground electronic state $X^1\Sigma^+$. The relationships in eq 76 were later used in most of the studies on the photofragment angular momentum polarization in HCl, HBr, and HI photodissociation for determination of the transition probabilities and the phase shift from the anisotropy parameter values.

3.2.3.2. HCl. Shortly after the theory for HF was developed, experimental studies of orientation and alignment of the ground and spin−orbit excited states of chlorine fragments in HCl photodissociation at 193 nm were reported by Rakitzis and co-workers who also suggested that its dissociation must yield spin-polarized hydrogen atoms.[78,133,191] This effort included quantum mechanical calculations that could be directly compared to experiment. The theoretical investigation, by Brown and co-workers,[134] was subsequently extended to cover a broad wavelength region. This strong theoretical foundation justifies an in-depth look at the HCl system.

Relevant adiabatic potential curves of the HCl molecule adapted from ref 134 are shown in Figure 15 to guide discussion. The initial excitations all have their origin in the perpendicular diabatic spin-allowed $A^1\Pi \leftarrow X^1\Sigma$ transition, which, through spin−orbit mixing with other underlying diabatic states, gives intensity to the nominally spin-forbidden $a^3\Pi_1 \leftarrow X^1\Sigma_{0^+}$ and $t^3\Sigma_1 \leftarrow X^1\Sigma_{0^+}$ transitions. In addition, there is a minor parallel component, $a^3\Pi_{0^+} \leftarrow X^1\Sigma_{0^+}$, found to be necessary for a complete description of the observed orientation. At 193 nm, the experimentally measured β parameters are -0.97 ± 0.03 and -0.87 ± 0.03 for Cl and Cl*, respectively, while the branching favors Cl formation over Cl* 59−41%.

Rakitzis et al. reported slice imaging measurements of alignment and orientation in Cl and Cl*, following photodissociation of HCl by linearly and circularly polarized 193 nm light.[78,133] The Cl* result could be analyzed directly using the expression $I(\theta) = I_0[1 + \beta_2(P_2(\cos\theta)]$ because there is only a rank $K = 1$ contribution to the polarization in this case. In this expression, $P_2(\cos\theta)$ is the second Legendre polynomial, I_0 is the total image intensity, and β_2 is a parameter (distinct from β) that characterizes the spatial anisotropy apparent in the image. I_0 and β_2 can be expressed in terms of the photofragment anisotropy β and the molecular frame orientation anisotropy parameters $Re[a_1^{(1)}(\parallel,\perp)]$ and $a_0^{(1)}(\perp)$, and these were fitted to experimental images obtained in two different probe laser polarizations to yield the orientation parameters. The analysis for Cl, with contributions up to rank $K = 3$ possible, involved simultaneous fitting of additional parameters. In case of circularly polarized photolysis light, the experimental images showed profound changes in the apparent angular distributions with reversal of the probe helicity, clearly indicating substantial photofragment orientation.[78]

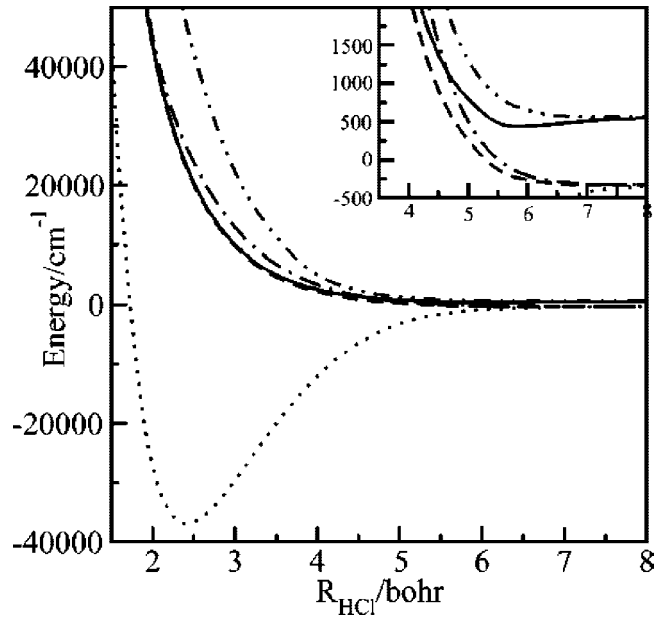

Figure 15. Fully adiabatic potential curves for HCl. The potentials, in order of increasing energy in the asymptotic region (inset), are $X^1\Sigma_0^+$(dotted line), $a^3\Pi_1$ (dashed-dotted line), $A^1|\Pi_1$ (dashed line), $a^3\Pi_0^+$ (solid line), and $t^3\Sigma_1$ (dot-dot-dashed line). Reproduced with permission from *J. Phys. Chem A* **2004**, *108*, 7790. Copyright 2004, American Chemical Society.

On the basis of the observed Cl orientation, conservation of angular momentum was invoked to infer the spin orientation in the undetected H atom product, in effect equal to the total chlorine atom orientation. For H atoms formed in conjunction with Cl and recoiling along the photolysis propagation direction, the inferred electron spin polarization is 52%, while that formed with Cl* is 100% polarized. The spin polarization averaged over all recoil directions is half-this limiting value. Although the H atom has not been directly measured in these experiments, the results for the cofragment Cl and Cl* clearly imply significant electron spin polarization. Coupling of the electron spin with the proton spin in the H atom will lead to oscillations with a period of 0.7 ns. For longer times or broader dissociation laser pulse durations, 50% depolarization of the electron spin will occur. After averaging over the electron spin corresponding to Cl and Cl* coproduction, and hyperfine depolarization, 36% spin polarized H atoms are expected along the photolysis laser propagation direction.

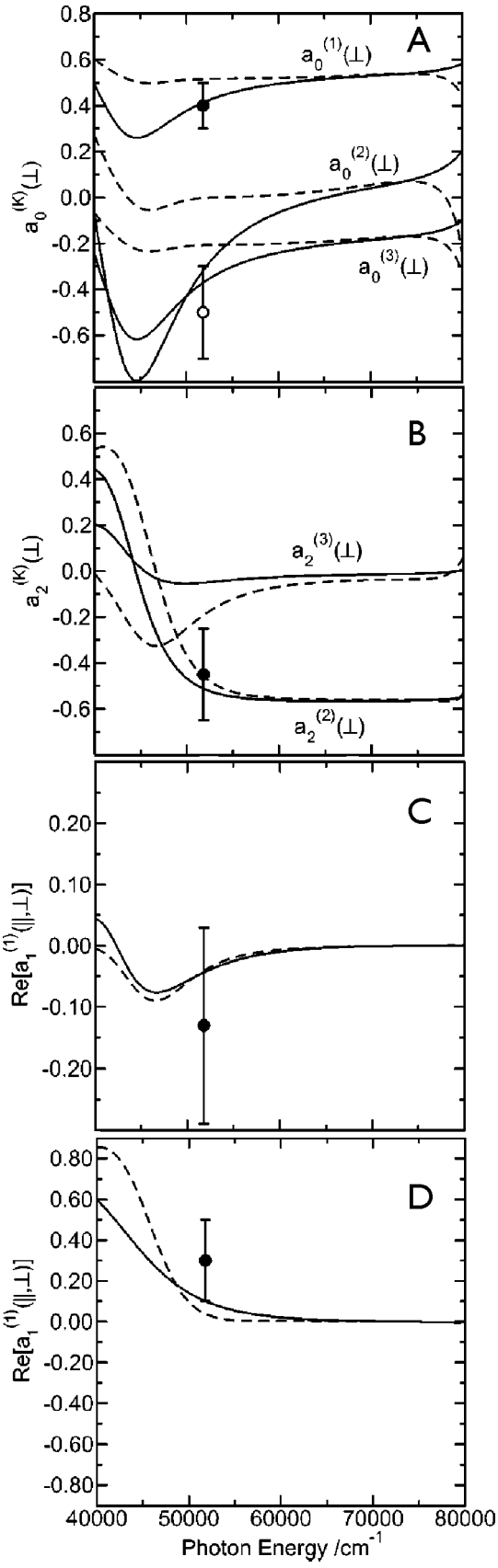

Figure 16. Indicated Cl anisotropy parameters from theory (lines) and experiments of Rakitzis et al.[78,133] at 193 nm: (solid lines) HCl and (dashed lines) DCl. Panels A−C refer to ground-state Cl, while D is for spin−orbit excited Cl*. Reproduced with permission from *J. Phys. Chem. A* **2004**, *108*, 7790. Copyright 2004, American Chemical Society.

As mentioned above, Brown and co-workers reported a detailed theoretical study of the complete angular momentum polarization distributions for HCl and DCl photodissociation at a range of photolysis energies,[134] building upon extensive ab initio calculations by Alexander et al.[135] A time-dependent wave packet approach was used to generate the photofragmentation **T**-matrix elements. From these, the dynamical functions could be calculated, ultimately yielding the molecular frame polarization parameters. Results for Cl from HCl and DCl dissociation are shown in Figure 16. The polarization parameters in general show a significant variation with wavelength, in particular manifesting a large fluctuation at lower energies. It is notable that this wavelength dependence is strongly damped for DCl compared to HCl. Furthermore, for DCl, the incoherent alignment in the ground-state Cl atom is negligible regardless of wavelength.

As shown in Figure 16, the agreement of the experimental values of the parameters $a_0^{(1)}(\perp)$, $a_0^{(2)}(\perp)$, $a_2^{(2)}(\perp)$, and $Re[a_1^{(1)}(||,\perp)]$ with theory is quite satisfactory. The $a_2^{(K)}(\perp)$ parameters (Figure 16B) arise from coherent perpendicular excitation of the $a^3\Pi_1$ and $A^1\Pi$ states.Again, there is significant variation with photolysis energy especially in the low-energy region. The single experimental measurement for a $a_2^{(2)}(\perp)$ in HCl dissociation agrees quite well with the theoretical calculation. Results for the $Re[a_1^{(1)}(||,\perp)]$ parameter are shown in Figure 16C. Here, the deviation from zero is small, and again occurs only at the low energy where the parallel contribution is not negligible. The parameter reflects interference between the parallel component, arising from nonadiabatic coupling of the $a^3\Pi_{0+}$ state to the ground state and the dominant perpendicular contribution. It is a direct measure of this interference, and thus the parallel contribution. The theoretical prediction at 193 nm falls within the rather large uncertainty of the experimental measurement.

For the Cl* product, $K = 1$ orientation is the only polarization possible, and the coherent a $[a_1^{(1)}(||,\perp)]$ parameter is shown in Figure 16D. The effect is significant only at the lowest energy, and the agreement with the experimental measurement is not particularly good. The incoherent orientation parameter a $a_0^{(1)}(\perp)$, not plotted, is reported to be constant at its limiting value of 0.577 at all photolysis energies, both for HCl and DCl photodissociation. This is so because, depending on the helicity of the dissociation light, only a single state, $^3\Sigma_{\Omega=\pm1}$ contributes to the incoherent orientation. This is in fair agreement with the experimental measurement of 0.6 ± 0.14.

Direct determination of the hydrogen atom spin polarization has recently been demonstrated by Sofikitis et al.[192] by means of detection of polarized fluorescence at 121.6 nm. The polarization may be calculated in the molecular frame as follows:

$$P_e = \frac{j_z(\theta_c)}{j} = 2\sqrt{\frac{j+1}{j}}\,\frac{\mathbf{a}_0^{(1)}(\perp)\cos\theta_c}{1+\cos^2\theta_c} \qquad (77)$$

where j_z is the expectation value of the component of the electron spin along the recoil direction, θ_c is the recoil angle, and $j = {}^1/_2$ is the total electron spin of the hydrogen atom. As shown in eq 77, the spin polarization P_e has its maximum value $P_e^{\max} = \sqrt{[(j+1)/j]}\mathbf{a}_0^{(1)}(\perp)$ for atoms moving parallel to the photolysis beam propagation at $\theta_c = 0$ and has zero value for atoms moving in the perpendicular direction at $\theta_c = {}^\pi/_2$.

Equation 77 does not take into account the hyperfine depolarization in the H-atom, which gives a factor of ${}^1/_2$.

According to the recent suggestion by Rakitzis, the effect of hyperfine depolarization can be significantly suppressed by creating large nuclear polarization in the parent molecules via the coherent excitation to selected rotational states $|JM_J\rangle$ before the photolysis.[136,191] This is important because the method suggested may be used to reduce the effect of hyperfine depolarization.

Balint-Kurti and co-workers[134] have also presented a discussion of various dynamical models for the dissociation of hydrogen halides. These are (1) adiabatic, (2) diabatic or sudden, (3) quasiclassical, using analytical expressions for the probability of a nonadiabatic transition between two interacting states, and (4) statistical or strong coupling. The adiabatic model assumes that reaction occurs on a single adiabatic electronic state. Because the adiabatic model would result in a branching fraction Cl*/Cl of zero value, in contradiction to the experimental results, it is clearly incorrect. In the diabatic picture, the atoms are assumed to separate so rapidly that there is no time for electronic rearrangement to follow the changing nuclear configuration, and the nonadiabatic transitions occur in a narrow, well-defined region. Although the low reduced mass and large recoil velocity might lead one to suppose that hydrogen halides should fit the diabatic model well, the model in this case predicts no net spin polarization in the H atom, in contradiction to experiment. This is a consequence of the failure of the second condition above, namely, the requirement for a narrow region of nonadiabaticity. Examination of the wavepackets show two rather broad regions of rearrangement that have little overlap. In the first region, from 3.5 to 5.5 bohr, nonadiabatic transitions occur between the $A^1\Pi_1$ and the $t^3\Sigma_1$ states, while in the second region, from 5 to 8 bohr, transitions occur between the $A^1\Pi_1$ and $a^3\Pi_1$ states.

Although these transitions do not occur at localized internuclear distances, the fact that the couplings occur in distinct pairs allows for application of separated two-state models to represent the dynamics. The separate nonadiabatic area model qualitatively correctly predicts high polarization of the H fragments in the entire energy range and the polarization decrease at low energy. However, this model does not predict quantitatively the high- and low-energy behavior of the fragment polarization indicating that the nonadiabatic interaction in HCl involves three states one and occur for wide range of internuclear distances.

Finally, a statistical model assumes all states are fully coupled and thus that all accessible states are equally populated. This would yield branching of $^1/_3$ each to $A^1\Pi_1$ and $a^3\Pi_1$ (giving Cl) and $^1/_3$ to $t^3\Sigma_1$ giving Cl*. The predicted H atom spin polarization is also $^1/_3$. None of these models affords a satisfactory prediction over the full energy range of the calculations. At low energy, the wavepacket calculation results for HCl are near the adiabatic limit, while at high energy, they approach the statistical prediction. For DCl, the calculations are near the statistical limit over the entire energy range.

We suspect the reason why all simple dynamical models considered above fail to reproduce the result of the exact calculation for the dissociation of hydrogen halides as a function of excitation energy is based mainly on the high recoil energy of the hydrogen atom. According to the Rosen−Zener−Demkov−Nikitin nonadiabatic dynamical models,[51] nonadiabatic interaction between the adiabatic potential curves increases exponentially with the recoil velocity. In principle, all models which assume the "visualization" of the movement of atomic nuclei along the potential curves can be used only if the nonadiabatic interactions between the potential curves are localized in the relatively narrow areas of the internuclear distance R. For the fast moving hydrogen photofragment, this is probably not the case because the nonadiabatic interactions occur in the wide range of the internuclear distances. Therefore, only a complete quantum mechanical treatment will satisfactorily describe the hydrogen halide photodissociation dynamics.

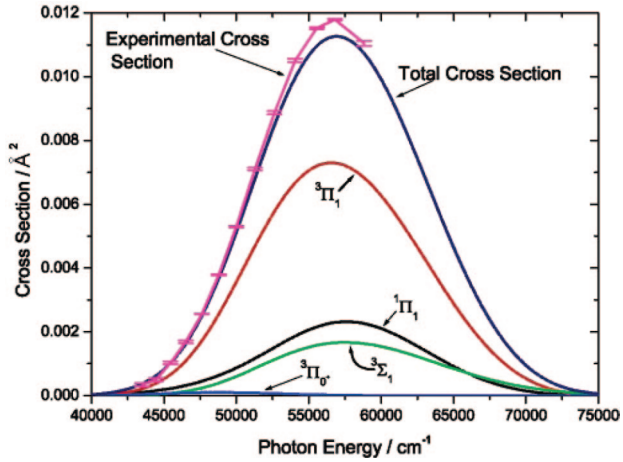

Figure 17. Total and partial cross-sections for the photodissociation of HBr from the ground vibrational state with experimental results from ref 138. Reproduced with permission from *J. Phys. Chem A* **2006**, *110*, 5371. Copyright 2006, American Chemical Society.

3.2.3.3. HBr. Angular momentum polarization in the photodissociation of hydrogen bromide was studied experimentally by Rakitzis and co-workers using slice imaging at 193 nm.[79,133] They used linearly and circularly polarized photolysis light for production of Br($^2P_{3/2}$) and Br($^2P_{1/2}$) photofragments and reported the values of a large number of the polarization parameters. These are parameter β, orientation parameters $\mathbf{a}_0^{(1)}(\perp)$, $Re[\mathbf{a}_1^{(1)}(\parallel,\perp)]$, and $Re[\mathbf{a}_1^{(3)}(\parallel,\perp)]$, and alignment parameters $\mathbf{a}_0^{(2)}(\perp)$ and $\mathbf{a}_2^{(2)}(\perp)$. Calculation of the H($^2S_{1/2}$) cofragment electron spin polarization using the conservation of angular momentum has shown that for the atoms recoiling along the $\theta_c = 0$ direction, see eq 77, it is very high [about 100% for the Br($^2P_{1/2}$) channel and 86% for the Br($^2P_{3/2}$) channel (neglecting the hyperfine depolarization)].

Ab initio potential energy curves, transition dipole moments, and spin−orbit coupling matrix elements were computed for HBr by Smolin and co-workers.[137] Unlike HF[26] and HCl[134] where the initial excitation is dominated by the $A^1\Pi_1 \leftarrow X^1\Sigma_{0^+}$ transition, see Figure 16, in HBr all optically allowed transitions can contribute. However, the parallel component is still much smaller than the perpendicular one and is highly sensitive to the finer details of the electronic structure calculations. Time-dependent quantum-mechanical wavepacket calculations have been performed to study the photodissociation dynamics of the molecule. Total and partial integral cross sections, the branching fraction for the formation of excited-state bromine atoms Br($^2P_{1/2}$), and the lowest-order anisotropy parameters, β, for both ground and excited-state bromine have been calculated as a function of photolysis energy and compared to experimental and theoretical data determined previously.

In particular, Figure 17 shows the total integral cross sections computed for the photodissociation of HBr from its ground vibrational state.[137] The figure also shows the

experimentally measured cross section of Huebert and Martin.[138] It is seen that the total integral cross section calculated by Smolin and co-workers[137] compares quite well to the one measured experimentally. The figure also shows the partial cross-sections. Surprisingly, the $a^3\Pi_1$ partial cross section, which arises from an electronically nonadiabatic transition from the $A^1\Pi_1$ state, makes the largest contribution to the total cross section, while both the $A^1\Pi_1$ and $t^3\Sigma_1$ partial cross sections make substantial contributions.

Nearly all calculated values of the anisotropy parameters $\mathbf{a}_Q^{(K)}$ were found to be in good agreement with the experimental results of Rakitzis et al.[79,133] within the experimental error. Insight is obtained into the nonadiabatic dynamics by comparison of the results of diabatic and fully adiabatic calculations. The calculation showed that most of the angular momentum orientation is produced because of an incoherent photodissociation mechanism and that the value of the corresponding anisotropy parameter $\mathbf{a}_0^{(1)}$ for $Br(^2P_{3/2})$ has a shallow maximum in the high photon energy side.

3.2.3.4. HI. Similar calculations for HI, based on both empirical and ab initio electronic structure data, have been performed by Brown[139] and Jodoin and Brown.[140] Jodoin and Brown have performed quantum mechanical time-dependent wave packet calculation based on the empirical adiabatic potential energy curves reported earlier by LeRoy et al.[141] and the transition dipole moments calculated ab initio by Alekseyev et al.[142] In their theory, Jodoin and Brown used an approach that completely ignores coupling between the adiabatic electronic states because of the kinetic energy operator. They computed a wide range of scalar and vector properties of the photodissociation as a function of photolysis energy: the total and partial cross sections, parameter β, and the full set of the body frame polarization parameters $\mathbf{a}_Q^{(K)}$ up to the rank $K = 3$. To the best of our knowledge, no experimental results have been reported so far on this system.

3.2.4. O_2

Angular momentum polarization in the photodissociation of molecular oxygen has been examined in the full range of energies from 4 to 10 eV. This spans three distinct regions: (1) the Herzberg bands and continuum from 4 to 6 eV, (2) the Schumann−Runge band and continuum, 6−8 eV, and (3) transitions through the $E(^3\Sigma_u^-)$ state from 8−10 eV.[143] We begin the discussion with the earliest such report, by Eppink et al. in 1997.[87] They used a two-step excitation via the $b(^1\Sigma_g^+)$ state to access the $B(^3\Sigma_u^-)$ state at a total energy of 7.71 eV in the region of the Schumann−Runge continuum. The B state correlates directly to $O(^3P) + O(^1D)$ products, and in their imaging study they used 2 + 1 REMPI through the $(^1F_3)$ level to probe the latter product. Because all the states involved have Σ character, only parallel contributions are expected and no perpendicular components were included in the analysis (and hence no coherences). From this diagonal treatment, they inferred m_J populations for the $O(^1D)$ product of 0.93:0.07 for $|m_j| = 0{:}1{:}2$, respectively. The $O(^1D)$ product is nearly completely aligned in $m_J = 0$, that is, a d_{z^2} orbital. Correlation arguments indicate that this result is expected for pure adiabatic dissociation. In this experiment, the correlated fine structure distribution for the $O(^3P)$ coproduct has not been resolved, but Huang and Gordon[144] had reported overall branching fractions of 0.93:0.07:0 for $O(^3P)$ $J = 2{:}1{:}0$, respectively, in the Schumann−Runge continuum. The observation that the fine structure distribution is dominated by the ground-state $O(^3P_2)$ product is consistent with adiabatic behavior. However, because there are a number of states that correlate to $O(^3P_2)$, this result is a necessary but not sufficient condition for adiabaticity. The alignment measurements are unambiguous evidence in support of predominantly adiabatic behavior. The observation of 7% $O(^3P_1)$ yield reported by Huang and Gordon[144] clearly indicates some level of nonadiabaticity; however, there is insufficient evidence to associate this with product with the $m_J = 2$ contribution to the alignment in the $O(^1D)$.

Recently, the Houston group at Cornell has reported a detailed study of O_2 photodissociation at a range of wavelengths in the VUV.[145] They examined the region from 120−133 nm, which is dominated by transitions to the lowest vibrational levels of the $E(^3\Sigma_u^-)$ state. At 130−133 nm they found both $O(^3P) + O(^1D)$ and $O(^3P) + O(^3P)$ channels contributing, while at shorter wavelengths, only the former process was observed. The β parameter was found to vary from 1.5 in the wings of the E state absorption to 0.5 in the center of the band around 124 nm. Although the transitions are, again, exclusively parallel in character, in this case excitation of a range of rotational levels, combined with long predissociation lifetimes, leads to a significant breakdown of the axial recoil approximation. Alignment in both $O(^1D)$ and $O(^3P_2)$ products was measured using the parallel/diagonal approach just as in the study of Parker and co-workers mentioned above. In addition, the $1 + 1'$ probe employed for the $O(^3P_2)$ detection was not sensitive to $m_J = 2$, and for $O(^1D)$, the $m_J = 2$ population was found to be negligible. They observed substantial alignment in the $O(^1D)$ product, reported as ratios of population in $|m_J| = 1$ to $m_J = 0$. This ratio ranged in value from 0.08 to 0.12, while an unaligned sample would have the value 2.

The Herzberg continuum is an electronically complex region of the oxygen absorption just above the lowest dissociation limit.[143] It consists of a series of electric dipole forbidden transitions, $A(^3\Sigma_u^+)$, $c(^1\Sigma_g^-)$, and $A'^3\Delta_u$), representing the Herzberg I, II, and III transitions. These borrow intensity from allowed transitions through complex spin−orbit and orbit−rotation interactions. The Herzberg I continuum includes a mixture of parallel and perpendicular character, while the II and III transitions are purely perpendicular. Buijsse and co-workers studied the angular distributions for all spin−orbit states of the product $O(^3P_J)$ atoms in this region to explore the detailed character of these excitations.[146] Their work inspired a thorough ab initio investigation of the electronic states in the Herzberg continuum by van Vroonhoven and Groenenboom, including predicted angular distributions, fine structure branching fractions, and photofragment polarization.[147] Although the latter measurements were never made by the Nijmegen group, Zare and co-workers recently reported results for $O(^3P_{1,2})$ molecular-frame orientation and alignment at a range of wavelengths in the Herzberg continuum.[97] They used a velocity-selective TOF technique in conjunction with the 2 + 1 REMPI probe of the O atom near 226 nm. They obtained results for the alignment parameters at 222 and 237 nm, showing both incoherent and coherent contributions. These results were compared with predictions for the incoherent polarization based on the semiclassical calculations of van Vroonhoven and Groenenboom. In combination with angular distribution measurements, these measurements allowed for decomposition of the transitions in terms of their parallel and perpendicular character and their relative contributions to the

incoherent alignment. Reasonable agreement was found with the semiclassical predictions, especially for the $J = 2$ case.

The orientation measurements reported by Alexander et al. consisted only of results for the coherent $Im[a_1^{(1)}]$ parameter resulting from dissociation via linearly polarized light. In this case, for the simple interference between one perpendicular and one parallel transition, the orientation parameter is proportional to $\sin(\Delta\varphi) = \sin(\varphi_\perp - \varphi_\parallel)$, where $\Delta\varphi$ is the asymptotic phase difference between the radial parts of the dissociative wave functions for the two states, as discussed above for ICl. Because this elastic scattering phase difference is expected to vary with excitation energy, Zare and co-workers measured the parameter at a series of dissociation wavelengths throughout the Herzberg continuum. The results were compared with predictions from the semiclassical treatment of van Vroonhoven and Groenenboom. Although the theory assumes only a single pair of interfering states, the magnitude of the orientation was reproduced satisfactorily. More recently, Brouard and co-workers reported a study of $K = 1, 2$ polarization in the $O(^3P_J)$ product of O_2 dissociation with broadband 193 nm excitation.[148] They attributed their results exclusively to dissociation via the Herzberg continuum owing to use of a cold molecular beam, although there are transitions from high ground-state rotational levels directly to the B state in this region. They combined their measurements with calculations based on the van Vroonhoven and Groenenboom calculations and found qualitative agreement with the incoherent contributions. They modeled the coherent contributions by estimating phase differences for dissociation by the different interfering paths and could account both for large coherent alignment contributions, as well as small coherent orientation as seen in the experiments.

3.2.5. RbI

The experimental study of the angular distribution of spin-oriented Rb ground-state photofragments produced in photolysis of RbI has been reported by Korovin and co-workers.[34,81,149] They used circularly polarized photolysis light at 266 nm to access the second excited continuum of the molecule, which correlates directly to the ground-state ($5^2S_{1/2}$) rubidium atom and the spin−orbit excited-state ($5^2P_{1/2}$) iodine atom. The continuum consists of three spectrally unresolvable states of the 1, 0^+, and 0^- symmetry (with respect to the Hund's case c coupling scheme).[150] The first two of these states can be optically excited from the $^1\Sigma^+$ ground-state giving rise to the parallel and perpendicular transitions and to the $\Delta\Omega = \pm 1$ coherence. As shown in section 2.1.7, the underlying dissociation dynamics in this case can, in general, be described by three anisotropy parameters, α_1, γ_1, and γ'_1; the first two usually contribute to the experimental signal obtained using circularly polarized photolysis light.

Doppler-resolved Faraday detection of the spin-oriented rubidium photofragment was used in the experiment. This technique explores the photofragment magnetic optical birefrigence of a vapor and is based on the gyrotropic component of the atomic polarizability causing the electric field of the probe light to be rotated by a certain angle after the light is passed through a polarized vapor. The experimental signal resulting from the rotation of the probe light polarization is described by a dispersion curve that has zero value at the center of the absorption line. Therefore, in comparison with resonance techniques, the Faraday detection has the advantage of reducing the influence of saturation effects and of thick optical layers on experimental data.[33]

The anisotropy parameters β, α_1, and γ_1 have been determined from experiment. The effect of thermal motion of the parent *RbI* molecules in the absorption cell was taken into account in the experimental data analysis. The values of the anisotropy parameters were found to be: $\beta = 0.48(8)$, $\alpha_1 = 0.138(20)$, and $\gamma_1 = -0.386(60)$, which indicate almost maximum possible spin-1/2 polarization of the produced rubidium atoms, see Table 4.

The obtained anisotropy parameters have been used for determination of the amplitude branching ratio $r_\perp/r_\parallel$ and the phase difference $\Delta\varphi$ of the photodissociation **T**-matrix elements that determine virtually all the dissociation dynamics in the chosen reaction channel. In particular, the photodissociation matrix elements (13) corresponding to the photodissociation via the $\Omega = 0^+$ and $\Omega = 1$ states can be written in the form

$$\langle \Psi_{0^+}^- | \hat{\mathbf{d}}_0 | \Psi_{0^+} \rangle = r_\parallel e^{i\varphi_0} \tag{78}$$

and

$$\langle \Psi_1^- | \hat{\mathbf{d}}_1 | \Psi_{0^+} \rangle = r_\perp e^{i\varphi_1} \tag{79}$$

where $(r_\parallel)^2$ and $(r_\perp)^2$ are the probabilities of the production of the photofragments in the corresponding reaction channels and φ_0 and φ_1 are the scattering phases.

Using eqs 13, 24, 27, 78, and 79, the anisotropy parameters in terms of the scattering amplitudes and phase difference $\Delta\varphi = \varphi_1 - \varphi_0$ can be written as[81]

$$\beta = \frac{2(r_\parallel^2 - r_\perp^2)}{r_\parallel^2 + 2r_\perp^2} \tag{80}$$

$$\alpha_1 = \frac{1}{\sqrt{3}} \frac{r_\perp^2}{r_\parallel^2 + 2r_\perp^2}$$

$$\gamma_1 = \frac{1}{\sqrt{3}} \frac{2\cos\Delta\varphi r_\perp r_\parallel}{r_\parallel^2 + 2r_\perp^2}$$

With the use of eq 80 and the experimental values of the anisotropy parameters, the branching ratio $r_\perp/r_\parallel$ and the phase difference $\Delta\varphi$ were found to be: $r_\perp/r_\parallel = 0.71(19)$ and $\Delta\varphi = 173(29)°$. The obtained negative value of the parameter γ_1 and the large value of the phase shift $\Delta\varphi$ have been interpreted by Korovin and co-workers using a model of precession of the photofragment angular momentum j with the frequency $\Delta\Omega_{coh}(R) = \Delta U_{coh}(R)/\hbar$, where ΔU_{coh} is the energy difference between the molecular states $\Omega = 1$ and 0^+ in the molecular electric field directed along the internuclear axis[69,81]

$$\Delta\varphi = \int_0^\infty \Delta\Omega_{coh}(R)\mathrm{d}R \tag{81}$$

where $R = R_0 + vt$, v is the relative photofragment velocity, R_0 is the equilibrium internuclear axis, and t is the time after absorbtion of the photon.

Therefore, the physical meaning of the obtained experimental result is that in the end of the photodissociation of *RbI* at 266 nm the components of the fragment angular momentum related to the anisotropy parameters α_1 and γ_1 are almost antiparallel to each other.

Note that no nonadiabatic interaction is expected between the 1 and 0^+ continuum states in RbI molecule; therefore

the origin of the obtained phase shift is very similar to that reported by Zare and co-workers in ICl[24,25] and related mostly to the elastic scattering phase shift from two potential curves of different symmetry. Therefore, the oscillations in the orientation signal of the type reported by Zare and co-workers[24,25] are expected also in RbI as function of the photolysis photon energy that can provide important information about the shapes of the unbound molecular potential curves.

3.3. Applications: Triatomic and Polyatomic Molecules

We now turn to a discussion of orbital polarization in dissociation of polyatomic molecules. We will examine the extensive experimental results that have been reported for select triatomic systems NO_2, N_2O, O_3, SO_2, CS_2, and OCS, as well as the more complex molecule, ethylene sulfide. It should be noted that the theoretical interpretation of results for polyatomic systems is hampered by the fact that the theory of Siebbeles et al. that forms the foundation of these analyses was developed in a basis best suited for diatomic molecules. Despite this, we believe that the *kinematic part* of the polarization cross sections in eq 11, which includes the recoil photofragment angular momentum distributions and related vector coefficients, is valid for polyatomic, as well as diatomic, molecules, and therefore the anisotropy parameters which can be obtained from experiment sufficiently describe the photodissociation of any molecule within first-order light-matter interaction perturbation theory.[186]

Although the expression for the dynamical functions in eq 13 is written in the form where Ω is a good quantum number, which is correct for linear molecules, for planar polyatomic molecules this is generally not the case. This makes it very complicated to estimate the values of the dynamical functions corresponding to certain dissociation processes in polyatomic molecules without high-level computation, as can be done for most of the diatomic molecules. Indeed, the formal theory of molecular photodissociation[35,37] can in principle be used for computation of the dynamical function values for any triatomic molecule regardless of the basis used. However, the computational difficulties are so high that no theoretical determination of the dynamical functions or anisotropy parameters for any triatomic or polyatomic molecule has been reported so far.

Nevertheless, as we show later, qualitative interpretations of the results of these studies based on the anisotropy parameter values determined from experiment are often possible and can provide deep insight into the underlying dynamics in some cases.

3.3.1. NO_2

In 1999, Ahmed and co-workers applied the theory of Siebeles et al. to dissociation of a polyatomic molecule for the first time in a study of NO_2 photodissociation at 213 nm.[8,23] Their 2-color imaging experiments probed alignment in the fine structure components of the ground-state oxygen atom product of that process. The alignment was negligible for the $^3P_2$ and $^3P_0$ states (the latter state cannot possess alignment). However, they reported substantial alignment in the $^3P_1$ O atom. This was dominated by an incoherent parallel contribution, but a significant component arising from the γ'_2 coherent term was also seen. This was ascribed to coherent excitation of parallel and perpendicular components of the transition moment in the O atom recoil frame, a consequence of the fact that the transition moment, which lies along a line connecting the oxygen atoms, is at some angle to the dominant recoil direction. The O atom recoil frame thus has both parallel and perpendicular components. The product O atom was said to "remember" the original molecular plane from which it came. This is an example of what has been termed a "static coherence" because the relative phases are fixed by the geometry, and this can arise even in dissociation on a single electronic state.

Recently, Coriou et al. examined NO_2 dissociation in a series of one-color imaging experiments in the region 200−205 nm.[151] This region was chosen because both O(^1D) and O(^3P) products could be probed here. For the ground-state O atom products, a broad distribution extending to 2.5 eV total energy release was observed, with a broad peak around 1.2 eV and sharper peaks appearing at lower energy. Similar behavior was seen in the 213 nm experiments of Ahmed,[23] but with perhaps less of the broad component. They reported the $^3P_2$:$^3P_1$:$^3P_0$ fine-structure distribution as 1.0:0.02:0.02 but expressed some suspicion that the large $^3P_2$ signal arose from an accidental resonance. Clearly, two-color measurements should be more reliable. They did not report angular momentum polarization measurements for the ground-state O atom but found β parameters around 1.0, somewhat lower than that reported by Ahmed et al. at 226 nm.

Coriou et al. also examined the O(^1D) product of NO_2 dissociation, at 203.8 and 205.5 nm. They determined the $Q = 0$ components of the $K = 2$ and 4 recoil frame multipole moments for REMPI detection through the $^1F_3$ and $^1P_1$ states corresponding to the range of each cofragment vibrational level, NO ($v = 0-4$). These were compared to semiclassical model calculations based on electrostatic interaction potentials for NO_2 developed as a function of the Jacobi angle. The best agreement was found with the $3A'$ model potential. It was argued, however, that averaging over a range of Jacobi angles consistent with the observed β parameters, the $1A'$ model potential fit as well, and this assignment was favored for consistency with the available literature. Finally, we should note that Brouard and co-workers recently studied NO_2 dissociation at 308 and 226 nm.[148] They found negligible O atom alignment at 308 nm and argued that Π character of the NO cofragment may lead to a more dense manifold of crossings and avoided crossings that could scramble the angular momentum polarization. Their results at 226 nm clearly showed a sharp fast peak for NO_2 dissociation, but an additional slow contribution was ascribed to N_2O_4 dissociation; this is not surprising given the large dissociation cross section for the latter molecule in the deep UV. Their results implied that some of the very slow structured products seen in the Ahmed study and, by analogy in the Coriou work above, may come from N_2O_4. Although it is surprising that the latter would give rise to such sharp structure, this is an important point for NO_2 studies in UV, and a deeper investigation is warranted.

It should be noted that the NO coproduct in NO_2 photodissociation is also highly polarized. The rotational angular momentum orientation and alignment of the NO fragments generated via linearly polarized 308 nm photodissociation of NO_2 was determined in an earlier study by Brouard's group[94] using laser-induced fluorescence. By observing the dependence of the photofragment NO Doppler-

resolved transition line shapes on experimental geometry, Brouard et al. determined multipole moments of the photofragment angular momentum distribution up to and including rank 3.

3.3.2. N_2O

The N_2O ground-state is linear and of $^1\Sigma^+$ symmetry, and there are excited states of $^1\Sigma^-$ and $^1\Delta$ symmetry. Optical transitions to these states are forbidden in linear geometry, as is also the case for OCS discussed below. As the molecule bends, these transitions gain intensity, the $^1\Sigma^-$ becomes the $1^1A''$ state and the $^1\Delta$ state splits into a Renner−Teller pair consisting of the $2^1A'$ and $2^1A''$ states. The latter is higher in energy and direct excitation of the $2^1A''$ state is believed to play at most a minor role in the dissociation in this energy region. Extensive calculations of these excited states[152–155] have been performed, and it is found that transition to the $2A'$ state dominates. The transition moment for this excitation lies in the plane of the molecule and largely follows the direction of the NO bond as the molecule is bent[155] but has both parallel and perpendicular components. However direct excitation of the $1^1A''$ state is also possible. The dissociation proceeds via crossing of these states with a repulsive $^1\Pi$ state ($^1A'^1A''$ in C_s) at larger NO distances. The importance of bending in promoting the transition is widely known both in experiment and theory, and bending in the excited-state accounts for the high N_2 rotational distribution seen, which peaks near $J = 75$.[156] The population anisotropy is speed-dependent,[156] and β averages about 0.5.[157] A similar value was obtained by Ahmed and co-workers using an approach that exploited the fact that the linestrength factors for the rank 2 alignment are opposite in sign for the two commonly employed REMPI transitions for $O(^1D)$. By making linear combinations of the angular distributions obtained via the two transitions, and optimizing the fit to the alignment-free expression, one could effectively eliminate the rank 2 alignment.

The first evidence for multiple dissociation components and $O(^1D)$ orbital alignment in 205 nm photodissociation of N_2O was reported by Suzuki et al.[121] in 1996 using ion imaging. Suzuki et al. presented the photofragment recoil distribution consisting of at least two components and suggested that there are overlapping electronic transitions, nonadiabatic transitions, or both that lead to different dissociation pathways.

A number of groups have studied $O(^1D)$ orbital polarization in N_2O photodissociation in the deep UV. Neyer et al., performed a one-color study probing state-specific N_2 angular distributions as well as alignment in the $O(^1D)$ in the region from 200−205 nm.[156,158] They employed a diagonal treatment in which the $O(^1D)$ m_J values were fitted with arbitrary independent angular distributions. The rank $K = 4$ contribution to the alignment was included in the treatment, but they reported difficulty fitting the results. They found the alignment dominated by $|m| = 1$ for the bulk of the distribution. Ahmed et al., in an imaging study of the rank 2 alignment in N_2O photodissociation at 193 nm, explicitly accounted for coherence using the laboratory frame anisotropy parameters discussed above. They found that the rank 2 alignment was dominated by an incoherent parallel contribution but also showed a significant perpendicular coherent component. The diagonal elements of the density matrix obtained by Ahmed et al., averaged over the angular distribution, agreed quite well with that determined by Neyer et al.

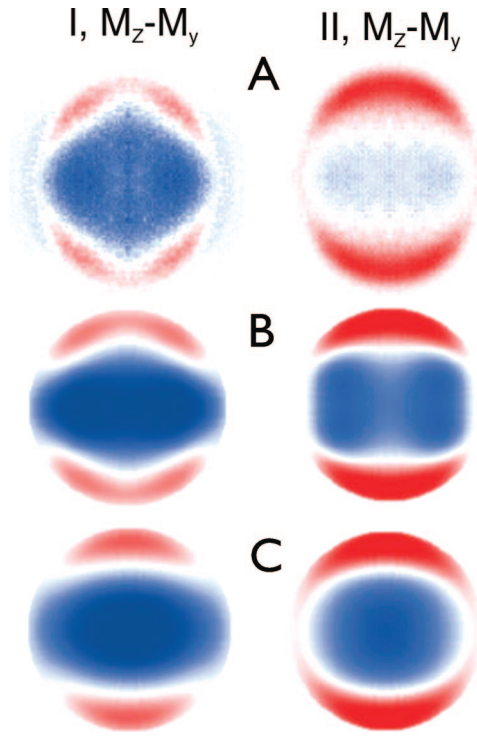

Figure 18. (A) Experimental unsliced alignment difference images for O ($^1D_2$) from N_2O dissociation at 193 nm for two experimental geometries showing forward convolution simulations (B) including and (C) neglecting the $K = 4$ contribution. Reprinted with permission from Smolin et al., *J. Chem. Phys.* **121** 6759 (2004). Copyright 2004, American Institute of Physics.

More recently, Teule et al.[155] studied dissociation of specific rotational levels of bend-excited N_2O prepared using a hexapole state selector. They used the same diagonal approximation employed in the earlier study, including the rank 4 contribution and fitted the $|m_J|$ levels independently. They supplemented these measurements with a theoretical prediction of the $|m|$ distributions on the basis of ab initio calculations of the potentials at short-range, with long-range potentials based on a quadrupole−quadrupole interaction. The model of Teule et al. then predicted $|m_J|$ distributions that depend on the bend angle of the dissociating molecule. For the $2A'$ transition, the product $|m| = 1$ was found to dominate for bend angles to about 35°, after which $|m| = 0$ and 2 both contributed with a similar angular dependence. Teule et al. then correlated the bend angles associated with production of N_2 $J = 70$ and 82 with the alignment in the $O(^1D)$ cofragment.

Smolin et al.[85] have re-examined the 193 nm dissociation of N_2O with specific attention to determination of all even-rank anisotropy parameters for $O(^1D)$, including both incoherent and coherent contributions. The results showed quite good agreement with the earlier analysis that considered only the $K = 2$ alignment but provided values for the $K = 4$ parameters as well. The experimental data for two geometries are shown in Figure 18, along with simulations obtained from the analysis with the $K = 4$ contributions included (Figure 18B) and omitted (Figure 18C). Nonzero values for all $K = 4$ parameters are obtained from the data, although the magnitude of these are lower than the $K = 2$ contributions.

Although a detailed interpretation of these observations is beyond the scope of what is currently theoretically possible, it is clear that they reveal the complex dynamics of this process. With multiple electronic states involved in

the excitation, and a number of nonadiabatic transitions likely during the dissociation, a complete characterization of the atomic orbital polarization must include many parameters to define the relevant amplitudes and phases of the photofragment scattering matrix.

The angular momentum alignment distributions of the $O(^3P_J)$ products of N_2O photolysis at 193 nm via the spin-forbidden triplet dissociation channel have been investigated by Brouard et al.[107] using velocity map imaging. The measured velocity and spatial anisotropy distributions indicate that around 60% of the available energy appears in product translation, with the remainder being released into internal excitation of the N_2 cofragment. As discussed in section 2.1.10, the small or zero value of the anisotropy parameter γ_2 measured by Brouard et al. is in qualitative agreement with the theoretical prediction for this type of reactions. The measured $O(^3P_J)$ alignment anisotropy parameters have been interpreted in terms of an instantaneous dissociation model, which suggests preferential population of $M_L = 0$ states and an electron density distribution peaking perpendicular to the direction of the breaking bond. This is consistent with dissociation on a surface of Σ^- symmetry, the most likely candidate correlating with ground-state products being the asymptotic $^3\Sigma^-$ ($^3A''$) surface. There are several possible routes to this surface, and these are considered in light of the measured velocity distributions and velocity-dependent spatial anisotropy parameters of the $O(^3P_J)$ products relative to the dominant $O(^1D)$ dissociation channel.

3.3.3. O_3

Although the dominant features of ozone photoabsorption in the ultraviolet spectral region are well-understood, there remain puzzles that so far elude definitive explanation: the mass independent heavy isotope enrichment in the stratosphere,[159,160] the vibrational structure seen in the Hartley and Huggins bands,[161,162] the varying bimodal vibrational distributions seen in the ground electronic state photolysis products,[163] and the variation in the vibrational distributions in the dominant excited-state products throughout the UV.[164] The methods discussed in this review are ideally suited to probe the details of ozone's photochemistry, a system notorious for its electronic complexity,[165–168] and interest in ozone dates to some of the earliest imaging studies of orbital alignment in work from the Houston group.[98,163,169–171]

Ozone's intense UV absorption in the Hartley band peaks around 254 nm, and this was ascribed solely to excitation to the $\tilde{B}$ state in the diabatic representation (see potential energy surface cuts in Figure 19 from ref 166). Subsequent diabatic dissociation yields mainly $O(^1D)$ and $O_2(a^1\Delta_g)$, but roughly 10% of the branching leads to ground-state products via the $\tilde{R}$ state. Dylewski et al. reported a detailed study of alignment in ozone dissociation across a significant portion of the Hartley band. They applied both the diagonal treatment, in which coherences were neglected, and the angular dependence of the m_J distribution was determined by fitting, and a fully quantum mechanical approach.[98] They concluded that at dissociation wavelengths of 255 and 298 nm, an incoherent parallel excitation mechanism dominates, supporting previous assertions, based on theory, that the initial absorption and subsequent dissociation largely take place on the 1^1B_2 surface. Their data also clearly show a $K = 4$ contribution, suggesting additional participation of other excitation or dissociation pathways, but this was not included in the analysis. They also reconstructed the $K = 0, 2$ contributions to the $O(^1D)$ angle-dependent density matrices. More recently, Hancock and co-workers[172,173] have reported significant alignment and orientation in the molecular $O_2(a^1\Delta_g)$ fragment, and this was seen to fluctuate with product rotational state, perhaps related to the rotational-state dependent curve crossing reported by Valentini and coworkers.[174] This observation of substantial rotational orientation is surprising and, to date, lacking a thorough explanation.

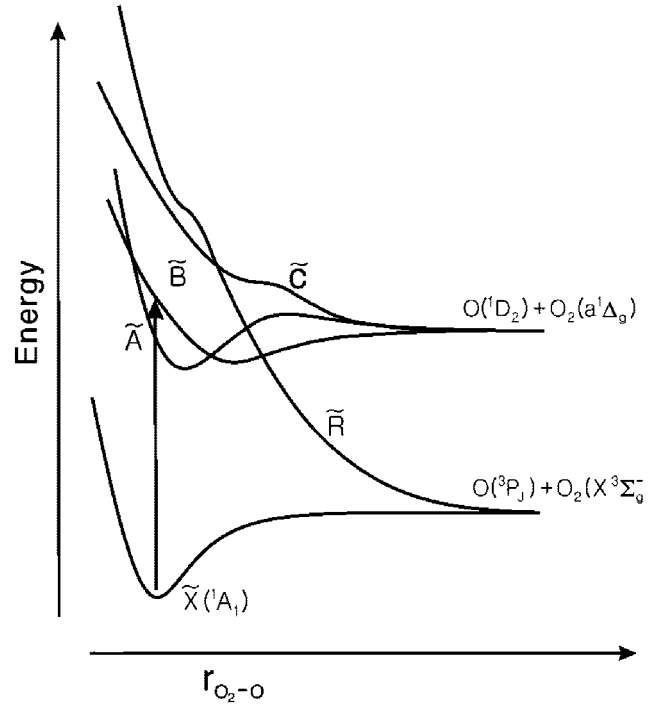

Figure 19. Schematic cuts through diabatic potential energy surfaces for ozone.

Recently Lee et al. reported detailed measurement of $K = 1$ and 2 polarization of the $O(^1D)$ from ozone dissociation at wavelengths from 248−285 nm.[80] This study, using DC slice imaging, allowed the recoil speed-dependence of the polarization to be revealed with great clarity. Experimental images are shown in Figure 20 for photolysis at 266 nm using left and right circularly polarized probe light. The dissociation laser was polarized both circularly and linearly at 45°, as shown, to detect the atomic orientation effect. The four rings in each image correspond to $v = 0-3$ in the $O_2(a^1\Delta_g)$ cofragment. The difference images show that the values of orientation anisotropy parameters (α_1, γ_1), obtained using circularly polarized photolysis light, are negligible within the statistical error. For the case of 45° linearly polarized light, however, there is a strong orientation effect (γ'_1) that is strongly dependent upon the photofragment recoil speed. A striking feature is the change in sign of the innermost ring relative to the other three, which is confirmed by switching the direction of the photolysis polarization from +45° to −45°, as shown. This clearly reveals that the coherent parallel/perpendicular contribution is dominant and is correlated with the recoil of the O_2 cofragment in ozone photodissociation.

To investigate closely the recoil speed dependence of γ'_1, these measurements were carried out at various dissociation wavelengths (Figure 21). A change of sign in the difference images and a change of sign in γ'_1 is seen for the slower fragments consistently. This reveals that the sign and

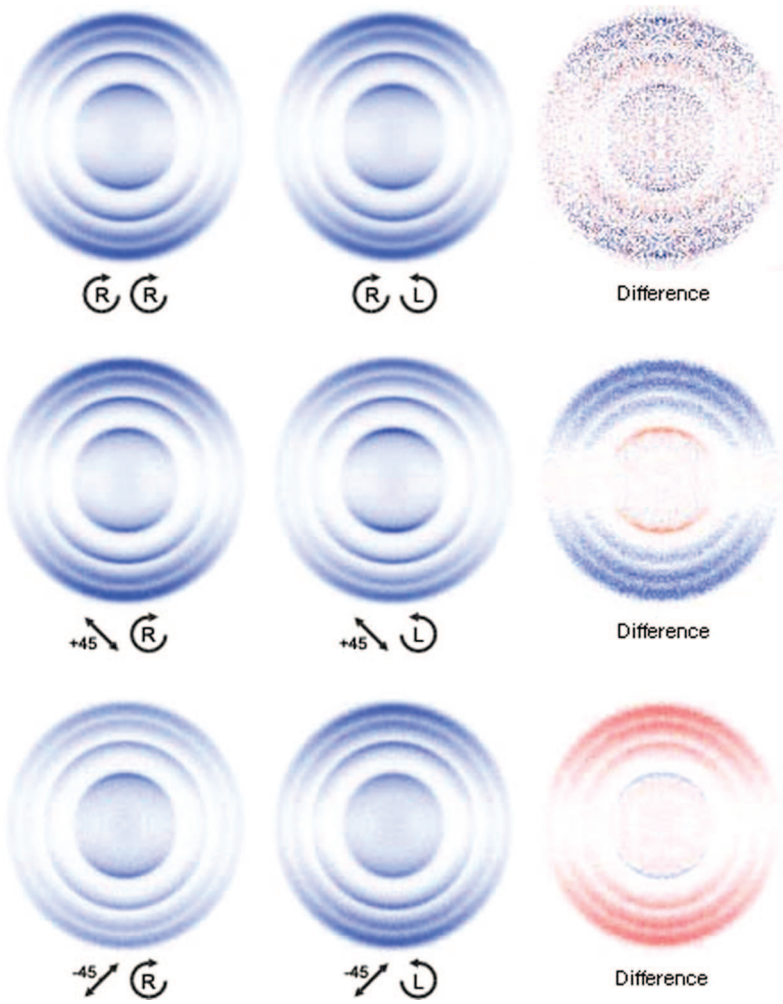

Figure 20. Experimental raw DC sliced images and orientation difference images for O^1D_2 dissociation at 266 nm at the indicated photolysis and probe laser polarizations. S. K. Lee et al., *Phys. Chem. Chem. Phys.* 2005, **7** 1. Reproduced by permission of the PCCP owner societies.

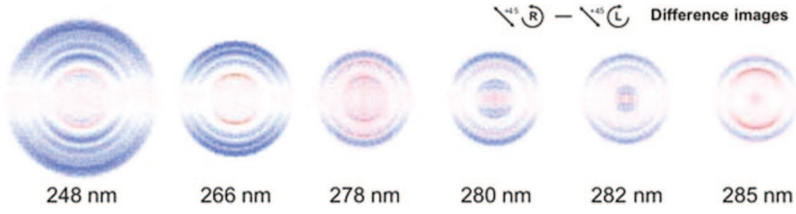

Figure 21. Wavelength dependence of the difference images for orientation produced by dissociation of ozone with linearly polarized light. S. K. Lee et al., *Phys. Chem. Chem. Phys.* 2005, **7** 1. Reproduced by permission of the PCCP owner societies.

magnitude of γ'_1 correlates most strongly with the O atom recoil speed rather than the specific vibrational level of O_2 cofragment. In particular, for the photolysis wavelengths near 280 nm, a sharp change of sign in one ring is seen, implying that the correlation of γ'_1 with cofragment rotational level may be part of the dependence of the orientation effect on recoil speed.

The absolute $K = 1$ orientation anisotropy parameters can be obtained by fitting the difference images with proper normalization. For the γ'_1 case, it is also possible to measure directly the orientation parameter by simply integrating the total intensity of the difference image at each recoil speed. With the latter approach, γ'_1 is found and plotted as a function of O atom recoil speed in Figure 22 for selected wavelengths. One notable feature of these plots is that the peak of the orientation parameter does not generally occur at the peak of the population for each vibrational level. Instead, the maximum occurs at the slow side (corresponding to higher rotational states of the cofragment) at each vibrational level except for the innermost ring. For the inner ring, where γ'_1 changes sign, this dependence on cofragment rotational level is also inverted. That is, for the inner rings it is the lower rotational levels that have the largest magnitude of the orientation, and this occurs for rotational levels that are lower than the most probable levels for the given vibration. This behavior is consistently observed for other photolysis wavelengths.

The observation of a significant γ'_1 parameter is not surprising in dissociation of a nonlinear triatomic for the same reason that the γ_2 parameter was seen in NO_2, that is, there are both parallel and perpendicular components of the transition moment in the O atom recoil frame. Although this static coherence effect may play an important role in the orientation seen in ozone, the profound speed dependence

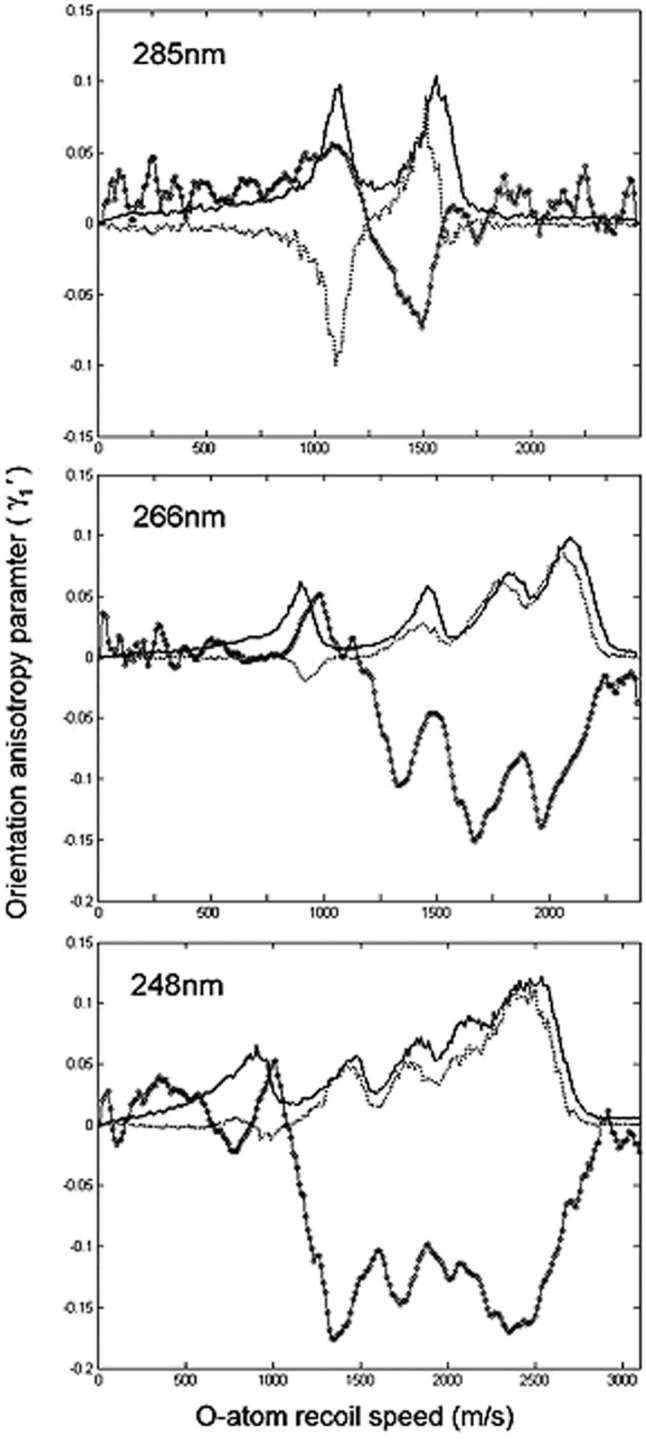

Figure 22. O atom recoil speed distribution (solid line), orientation difference signal (dotted line), and γ_1 orientation parameter (circles) for ozone dissociation at indicated wavelength. S. K. Lee et al., *Phys. Chem. Chem. Phys.* 2005, **7** 1. Reproduced by permission of the PCCP owner societies.

shows that this effect alone is inadequate to account for all the observations. The change of γ'_1 may reflect the changing diabatic and adiabatic dynamics in the dissociation. Schinke has recently argued that photoexcitation in the Hartley−Huggins band system is exclusively to the *B* state, but curve crossings with the *A* state occur both at very short-range (not likely to be important in this case), and at longer range.[165] Both the *B* and the *A* states encounter the *R* state subsequently, and there is additional opportunity for recrossing back. Furthermore, the *A* and the *B* states correlate asymptotically to the same electronic states of the products. Coherences created in the initial excitation may be preserved and give rise to interference following these curve crossings. In fact, the abrupt change seen as a function of recoil speed in each image may be a consequence of diabatic dissociation on the *B* state giving rise to large magnitude orientation effects for higher recoil speeds, with adiabatic dissociation (i.e., crossing to the *A* state) quenching this effect at lower recoil speeds. Superimposed upon these large effects may be smaller modulations induced by the long-range interactions and by other nonadiabatic processes. Additional theoretical investigation will be necessary to place this speculation on a more secure footing.

The study of angular momentum polarization in ozone has been extended both to the long wavelength and the short wavelength side of the Hartley band in recent work from Oxford. Brouard and co-workers examined $O(^1D_2)$ polarization following ozone dissociation at 193 and 205 nm using velocity map imaging.[175] The results at 205 nm were largely consistent with characteristics of the Hartley band dissociation, although with somewhat reduced anisotropy. The speed distributions agreed very well with wavepacket calculations from Baloitcha and Balint-Kurti performed exclusively using the diabatic *B* state, providing good evidence in support of the assignment as exclusively Hartley band in origin.[166,167] The results at 193 nm were seen as significantly different; however, the speed-dependent β parameters were found to be largely negative, as reported in earlier work and in contrast to results in the Hartley band. Furthermore, the velocity distributions showed a slow contribution suggesting the onset of a new electronic transition. We should note that 193 nm is near a local minimum in the ozone absorption, with a VUV band rising to shorter wavelength. Brouard et al. also reported polarization measurements for all anisotropy parameters through $K = 4$ obtained using the Fourier moment decomposition method. The results were presented in various forms: with explicit speed-dependence, integrated in separate fast (Hartley-band like) and slow (non-Hartley-band) distributions, and finally integrated over the recoil distribution and transformed to the molecular frame. Of particular note was the observation of non-zero values for the orientation induced by circularly polarized photolysis light (α_K and γ_K). This behavior was not seen in the Hartley band, supporting the notion that multiple excited states are directly accessed in ozone absorption at 193 nm. It is somewhat puzzling, however, that this "transfer helicity" appears in the fast component of the dissociation, which they otherwise associate with the Hartley-band component of the dissociation. Brouard and co-workers modeled the polarization effects by developing electrostatic long-range potentials in the manner of Teule et al., neglecting coherent excitation of multiple electronic states. They found consistency between experiment and the model if dissociation on the lowest state (Δ at linearity) were assumed. Interestingly, this same state was found to account for the dominant coherent orientation seen by Lee and co-workers[80] in the Hartley band.

The Hancock group has studied a number of issues in ozone dissociation on the long wavelength edge of the Hartley band using a REMPI-TOF technique. They reported product state distributions and angular momentum polarization in the diatomic O_2 ($a^1\Delta_g$) product.[172,173] This effort was extended by Ritchie and co-workers to include studies of angular momentum polarization in the $O(^1D_2)$ in the same region.[176,177] Their approach relied upon first obtaining the

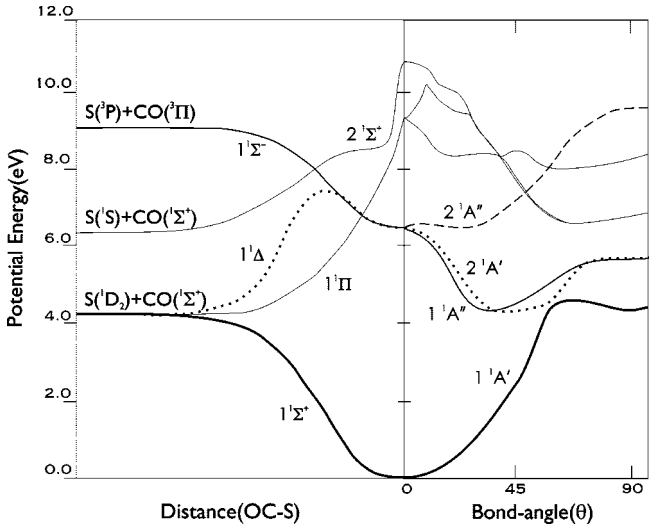

Figure 23. Cuts through the relevant potential energy surfaces of OCS adapted from ref 178 Reused with permission from Suk Kyoung Lee, *J. Chem. Phys.*, **125**, 144318 (2006). Copyright 2006, American Institute of Physics.

laboratory frame polarization using the bipolar moment approach, with subsequent transformation of these to the molecular frame parameters. The results, extended to rank 4, were found to be largely consistent with the work of Dylewski et al. for the alignment and with Lee and co-workers for orientation. They also found incorporation of the $K = 4$ results to be important in obtaining an accurate fit overall.

3.3.4. OCS

The first published imaging investigation of atomic orbital alignment in photodissociation was a study of carbonyl sulfide dissociation reported by Suzuki and co-workers in 1996.[86] This was followed in 1998 by a major study from the Suzuki group combining theory and experiment in a comprehensive treatment of the process.[178] Since that time, OCS has become a cornerstone molecule in the study of these phenomena, with almost all of the work conducted near the peak of the first absorption band around 222 nm. We will examine this molecule and the rich literature surrounding it in some detail.

Cuts through the potential surfaces of OCS are shown in Figure 23 to guide the following discussion. The ground-state of OCS is linear, but dipole excitation of OCS is weakly allowed only for bent molecules, so we will consider the symmetry of the relevant excited states in both $C_{\infty v}$ and C_s symmetry.[178] The ground $1^1\Sigma^+$ state becomes $1^1A'$, and there are $1^1\Sigma^-(1^1A'')$ and $1^1\Delta(2^1A' + 2^1A'')$ states accessible in the UV region. Ab initio calculations by Suzuki et al. showed that the $(1^1A'')$ and $(2^1A')$ surfaces are strongly bent and show a similar topography. They cross a $(^1\Pi)$ state $(C_{\infty v})$, and this results in avoided crossings and adiabatic dissociation pathways leading to $S(^1D)$ and $CO(X^1\Sigma^+)$ from both excited states. Suzuki obtained images for both ground-state $S(^3P)$ atoms and $S(^1D)$, and we focus on the latter, the dominant product (>95%).The experimental images and simulations are reproduced in Figure 24. The imaging study at wavelengths from 222 to 248 nm confirmed the existence of a bimodal rotational distribution in CO seen earlier by Houston and co-workers.[179,180] The experimental observations, supplemented by sophisticated wavepacket calculations, showed that the low rotational levels arose from excitation of both

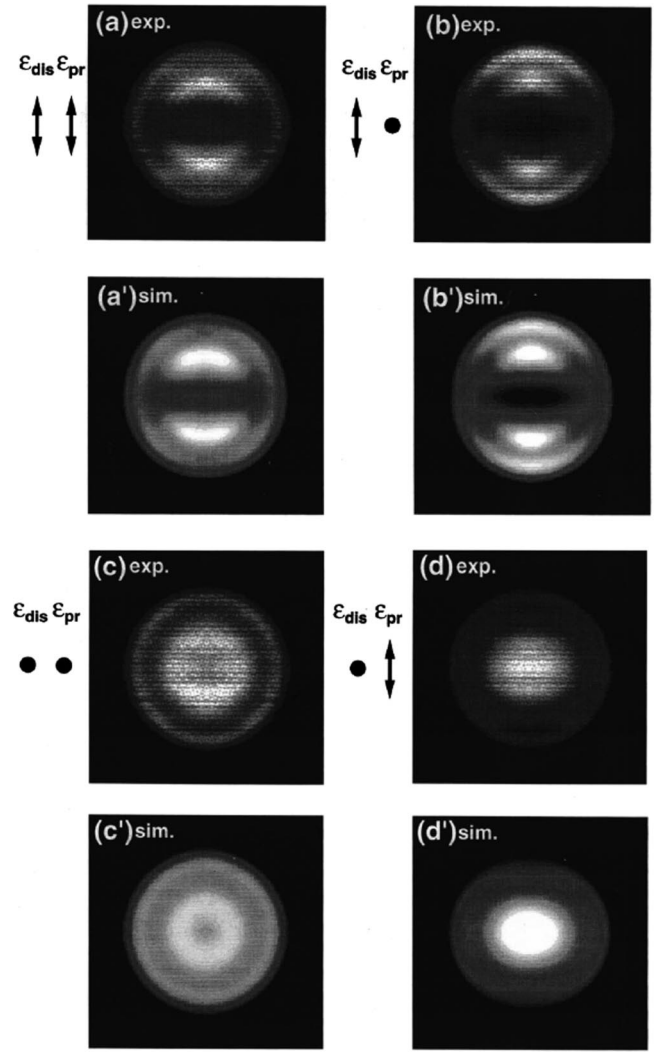

Figure 24. $S(^1D_2)$ images and simulations for dissociation of OCS at 223 nm for indicated combination of photolysis and probe laser polarizations. Reused with permission from Toshinori Suzuki, *J. Chem. Phys.*, **109**, 5778 (1998). Copyright 1998, American Institute of Physics.

the $2^1A'$ state and the $1^1A''$ state, while the slower peak, corresponding to higher rotational excitation, could be associated exclusively with $2^1A'$ excitation, followed by a nonadiabatic interaction at large bending angles leading finally to dissociation on the ground-state surface. Suzuki et al. measured $S(^1D)$ alignment images at 223 nm, and analyzed the results using a diagonal approach.

For the fast component, they found m_J distributions of 0.48:0.24:0.02 for $0/\pm1/\pm2$, respectively, while for the slow peak the values were 0.60:0.14:0.06. After taking into account the alignment, they obtained β values of 1.8 and 0.7 for the slow and fast peaks, respectively. One other significant observation in the Suzuki work was the importance of bending motion to account for the large rotational excitation. Large impact parameters (>1.5Å) are implied by the large rotational excitation and modest recoil speeds. These impact parameters are not consistent with an impulsive origin for the rotational excitation for a quasi-linear molecule.

Shortly after Suzuki's detailed study, Zare and co-workers measured the speed-dependent orientation in $S(^1D)$ produced in photolysis by linearly polarized light at 223 nm.[83] This yields the molecular frame $Im[a_1^{(1)}(\parallel,\perp)]$ parameter, which is related to the laboratory-frame γ_1' parameter. They found

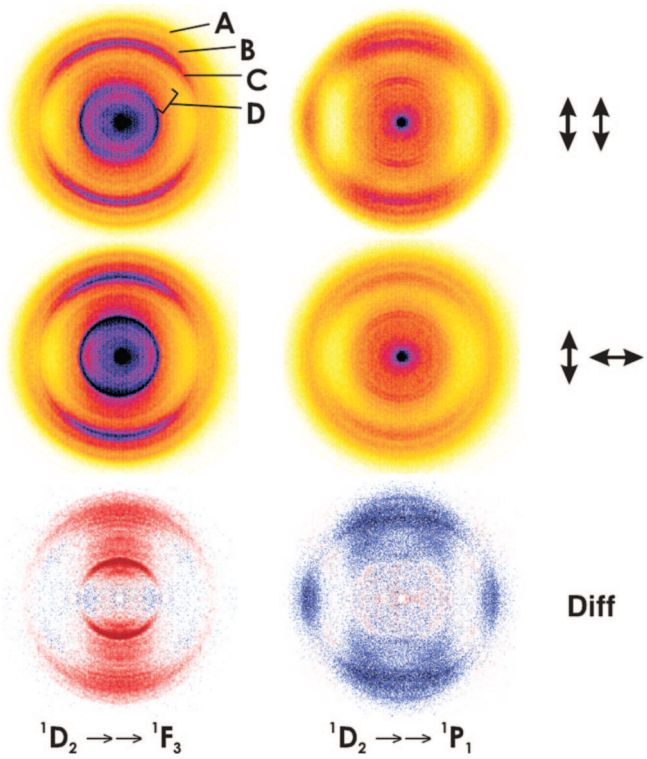

Figure 25. S($^1D_2$) images for dissociation of OCS at 193 nm for indicated combination of photolysis and probe laser polarizations and indicated probe transition. Reused with permission from Suk Kyoung Lee, *J. Chem. Phys.*, **125**, 144318 (2006). Copyright 2006, American Institute of Physics.

a maximum orientation for the fast peak that Suzuki ascribed to simultaneous A' and A'' excitation, and significantly less for the slow peak ascribed to excitation to the A' state exclusively. They favored interpretation of the orientation as evidence for coherent excitation to these two states, although a static coherence analogous to NO_2 could not be ruled out.

Later, Rakitzis and co-workers[91] suggested a method to measure directly the photofragment alignment from Abel-invertible two-dimensional ion images, as a function of photofragment recoil velocity. The method was applied for S($^1D_2$) atoms from the photodissociation of OCS at 223 nm. The results were analyzed in terms of coherent and incoherent contributions from two dissociative states, showing that the phase differences of the asymptotic wave functions of the fast and slow recoil-velocity channel are approximately $\pi/2$ and 0, respectively.

Recently, Lee et al. conducted a detailed study of angular momentum polarization in S(^1D) from OCS dissociation at 193 nm.[62] They reported complete measurement of all anisotropy parameters through rank $K = 4$ as a function of recoil speed and angle, obtained using the dc slice imaging approach. The dc sliced alignment difference images are shown at the bottom of Figure 25. The alignment images are very different on the different probe transitions, in this case showing the important contribution of the $K = 4$ multipole. Lee et al. detected three main bands (A−C in Figure 25) in the recoil speed distribution at 193 nm, and each showed a distinct angular distribution and associated polarization parameters. The dominant, innermost C ring exhibited the maximum anisotropy, $\beta \approx 0.8$, while the intermediate B ring showed the minimum, $\beta \approx 0.3$. Coherent speed dependent alignment was seen in both the A and B rings for $K = 2$ and 4, while the C ring showed little alignment. The $K = 1$ orientation showed a strong peak in the γ_1' parameter for the B ring, which dropped off abruptly toward both the A and C rings.

These observations were interpreted in a manner consistent with Suzuki's results at longer wavelength, that is, the A ring was ascribed primarily to adiabatic dissociation via the 2A′ surface, while the B ring includes a considerable contribution from adiabatic dissociation via the 1A″ surface. This gives a perpendicular contribution to the angular distribution in the B ring, reducing the β value, and at the same time accounting for the strong γ_1' peak. The C ring was ascribed to initial excitation to the 2A′ surface, followed by a nonadiabatic transition to the 1A′ surface on the way to dissociation. However, the above interpretation is not unique because it does not take into account strong bending motion in the OCS excited states. As discussed earlier, the value of β can be significantly changed from its extremal negative to the extremal positive values depending of the amplitude and the sign of the bending angle $\alpha^{(0)}$ within the same parallel $A' \leftarrow A'$ transition. Therefore, conclusions concerning the relative excitation intensity to the A' and A'' states should be done with great care. From these detailed anisotropy measurements, Lee et al. were able to construct the complete S(^1D) density matrix for any recoil speed or angle, and they did this explicitly for recoil at 0°, 45°, and 90° for circularly polarized photolysis light.

A final significant observation from this study is highlighted in Figure 26. The S(^1D) magnetic sublevel populations are shown for polar recoil in the B and C rings, obtained using only the $K = 2$ results and including both $K = 2$ and 4. It is seen that for the B ring, the results obtained neglecting the $K = 4$ contribution are seriously in error, implying that measurement of the complete density matrix is essential to obtain an accurate picture of the dynamics in this region.

3.3.5. SO_2

Atomic orbital alignment polarization in photodissociation of SO_2 has been studied at 193 nm by Brouard et al.[108] using resonantly enhanced multiphoton ionization of ground-state O(^3P_J), coupled with velocity-map ion imaging. The photodissociation dynamics of sulfur dioxide have been subjected to many studies over the past three decades, see for example the review paper;[181] however, the details of the dissociation mechanism are yet to be explained unambiguously. The $C^1\tilde{B}_2 \leftarrow X^1\tilde{A}_1$ electronic transition is known to begin at around 240 nm, with predissociation into O(^3P) + SO($^3\Sigma^-$) products occurring above a threshold at approximately 219 nm. Dynamical measurements have been conducted, using a range of experimental techniques, over a wavelength range of 193−218 nm, where the excess energy is insufficient to permit the formation of electronically excited products.

Brouard et al.[108] used velocity-map ion imaging to measure the O(^3P_J) photofragment speed distributions, speed-dependent translational anisotropies, and atomic angular momentum alignment parameters for each of the three spin−orbit states ($J = 0$, 1, 2) following photolysis at a wavelength of 193 nm. The former two measurements provided confirmation of a number of previous findings, however new results have also been obtained. The polarization data for $J = 1$ and 2 have been used to estimate the state multipole moments of the O-atom electron spin and orbital angular momenta. The data suggest that both sources of O-atom electronic angular momentum are polarized. It is shown that the spin polariza-

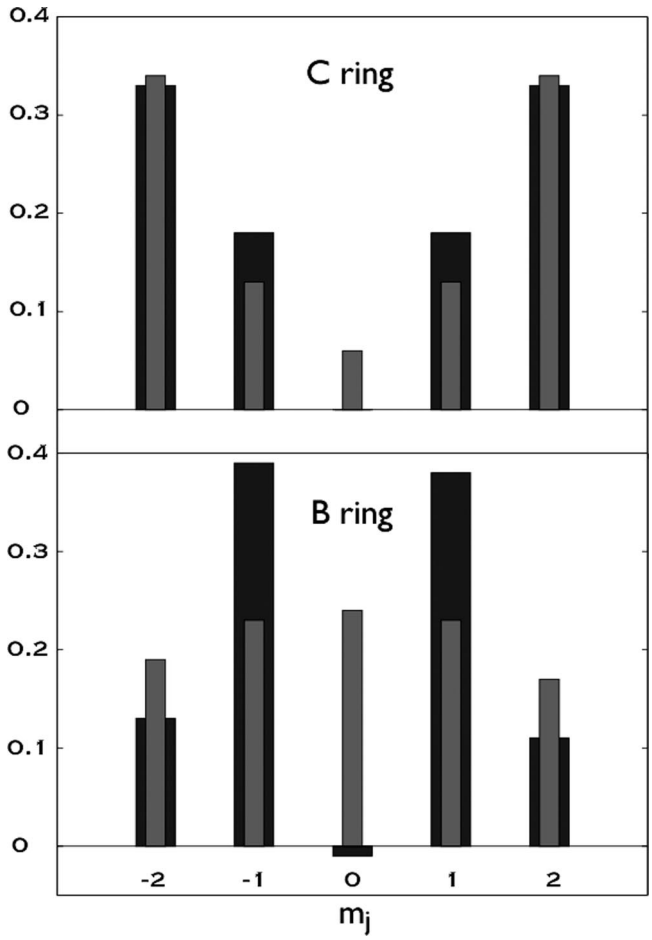

Figure 26. Magnetic sublevel distribution for polar recoil of S($^1D_2$) from dissociation of OCS at 193 nm for indicated recoil region (See Figure 25). Results are shown both neglecting (gray bars) and including (black bars) the $K = 4$ contribution. Reused with permission from Suk Kyoung Lee, *J. Chem. Phys.*, **125**, 144318 (2006). Copyright 2006, American Institute of Physics.

tion could either arise from exit-channel couplings or be a manifestation of the participation of triplet states in the dissociation. The angular dependence of the potential energy in the exit channel was examined using long-range quadrupole−dipole and quadrupole−quadrupole interaction terms, from which molecular-frame multipole moments of the orbital angular momentum of the recoiling O atoms was calculated. Comparison with the experimentally derived multipole moments was used to help provide insight into the dissociation mechanism.

The values of the determined anisotropy alignment parameters were found to be in a qualitative agreement with theoretical prediction, as discussed in the end of section 2.1.10.

3.3.6. Ethylene Sulfide

Atomic orbital polarization in photodissociation of polyatomic systems (meaning here four or more atoms) has only been observed in a single case: a study of ethylene sulfide dissociation at 193 nm reported by Townsend et al.[117] This may be more a consequence of the range of systems to which these experimental techniques have been applied rather than any fundamental physical restrictions. In UV dissociation of ethylene sulfide, S atom loss is the dominant dissociation pathway, and branching to S(^{1}D) production is about 40%.[182] Photofragment translational spectroscopy studies using tunable synchrotron radiation had shown a broad trimodal velocity distribution for S(^1D), and this was ascribed to dissociation via several distinct potential energy surfaces.[183,184] The excitation was believed to to proceed from a predominantly nonbonding orbital localized on the sulfur atom via a $4p_x$ Rydberg state[185] to yield a broad continuum of photofragment kinetic energies in the approximate range 0−2.6 eV. The excitation is known to be predominantly parallel in nature and a recoil-energy averaged value of β of about 1.1 had been determined.[182]

The study by Townsend et al. reported only the $K = 2$ laboratory frame anisotropy parameters. This study was the first slice imaging measurement of orbital polarization beyond a diatomic, so it was the first to demonstrate a nontrivial speed dependence. The study clearly confirmed the trimodal distribution reported earlier and quite interestingly showed significant orbital alignment only for the fastest peak, which had been ascribed to a direct excited-state dissociation process. For the slowest S($^1D_2$) fragments, the observed marginal alignment shows only a coherent perpendicular mechanism (η_2). The region corresponding to intermediate S-atom speeds displays no alignment at all. For the fastest photofragments, the alignment is dominated by a coherent superposition of perpendicular and parallel processes (γ_2), although there are also significant contributions from a coherent perpendicular mechanism (η_2) and also an incoherent excitation (s_2 and α_2).

A careful examination the absorption spectrum of ethylene sulfide reveals that, in addition to the strong Rydberg peak mentioned above, there are additional series beginning at longer wavelength, assigned as vibrational progressions of the $4p_z$ Rydberg orbital (B_1 overall symmetry) and, beginning at even longer wavelength, to a 4s Rydberg state (also B_1 symmetry overall).[185] These are pure perpendicular excitations, while the A_1 excitation is pure parallel (here parallel and perpendicular Õ refer to the direction of the transition moment relative to the molecular symmetry axis). The close proximity of the peaks corresponding to the $4p_z$ B_1 state suggest this contribution may be responsible for both the coherent parallel/perpendicular alignment and the incoherent perpendicular contribution for the fast peak. The alignment measurements thus suggest a modification of the earlier decomposition of the absorption spectrum at 193 nm.

4. Acknowledgments

We would like to thank the students and postdocs who have contributed to all this work over the years: Dr. Suk Kyoung Lee, Dr. Dave Townsend, Dr. Allan Bracker, Dr. Andrey Smolin, Dr. Konstantin Korovin, Dr. Vladislav Kuznetsov. We also want to acknowledge Dr. Greg Hall, Prof. Paul Houston, Prof. G.G. Balint-Kurti, Prof. J.A. Beswick, Prof. M. Brouard, Prof. K.-H. Gericke, Prof. A.J. Orr-Ewing, and Prof. D. Zimmermann, for valuable discussions. We would also like to thank our colleagues for their contributions to this active field. This work was supported by a Cooperative Grant from the Civilian Research and Development Foundation, CRDF Award No. RC2-2570-ST-03, and by the National Science Foundation under award numbers CHE-0415393 and CHE-0715300.

5. References

(1) Simons, J. P. *J. Phys. Chem.* **1987**, *91*, 5378.
(2) Houston, P. L. *J. Phys. Chem.* **1987**, *91*, 5388.
(3) Hall, G. E.; Houston, P. L. *Annu. Rev. Phys. Chem.* **1989**, *40*, 375–405.
(4) Vasudev, R.; Zare, R. N.; Dixon, R. N. *J. Chem. Phys.* **1984**, *80*, 4863.
(5) Dixon, R. N. *J. Chem. Phys.* **1986**, *85*, 1866.
(6) Gericke, K.-H.; Klee, S.; Comes, F. J.; Dixon, R. N. *J. Chem. Phys.* **1986**, *85*, 4463.
(7) Chandler, D. W.; Houston, P. L. *J. Chem. Phys.* **1987**, *87*, 1445.
(8) Siebbeles, L. D. A.; Glass-Maujean, M.; Vasyutinskii, O. S.; Beswick, J. A.; Roncero, O. *J. Chem. Phys.* **1994**, *100*, 3610.
(9) Vasyutinskii, O. S. *Opt. Spectrosc.* **1983**, *54*, 524.
(10) van Brunt, R. J.; Zare, R. N. *J. Chem. Phys.* **1968**, *48*, 4304.
(11) Vasyutinskii, O. S. *Sov. Phys. JETP Lett.* **1980**, *31*, 428.
(12) Rothe, E. W.; Krause, U.; Duren, R. *Chem. Phys. Lett.* **1980**, *72*, 100.
(13) Vigué, J.; Grangier, P.; Roger, G.; Aspect, A. *J. Phys. Lett.* **1981**, *42*, L531.
(14) Vigué, J.; Beswick, J. A.; Broyer, M. *J. Phys. (Paris)* **1983**, *44*, 1225.
(15) Aquilanti, V.; Grossi, G. *J. Chem. Phys.* **1980**, *73*, 1165.
(16) Hale, M. O.; Hertel, I. V.; Leone, S. R. *Phys. Rev. Lett.* **1984**, *53*, 2296.
(17) Hertel, I. V.; Schmidt, H.; Bahring, A.; Meyer, E. *Rep. Prog. Phys.* **1985**, *48*, 375.
(18) Campbell, E. E. B.; Schmidt, H.; Hertel, I. V. *Adv. Chem. Phys.* **1988**, *72*, 37.
(19) Mestdagh, J. M.; Visticot, J. P.; Meynadier, P.; Sublemontier, O.; Suits, A. G. *J. Chem. Soc., Faraday Trans.* **1993**, *89*, 1413.
(20) Beswick, J. A.; Vasyutinskii, O. S. *Com. At. Mol. Phys.* **1998**, *42*, 69.
(21) Wouters, E. R.; Ahmed, M.; Peterska, D. S.; Bracker, A. S.; Suits, A. G.; Vasyutinskii, O. S. Imaging the Atomic Orientation and Alignment in Photodissociation In *Imaging in Chemical Dynamics*; Suits, A. G., Continetti, R. E., Eds.; American Chemical Society: Washington DC, 2000.
(22) Bracker, A. S.; Wouters, E. R.; Suits, A. G.; Lee, Y. T.; Vasyutinskii, O. S. *Phys. Rev. Lett.* **1998**, *80*, 1626.
(23) Ahmed, M.; Peterka, D. S.; Vasyutinskii, O. S.; Suits, A. G. *J. Chem. Phys.* **1999**, *110*, 4115.
(24) Rakitzis, T. P.; Kandel, S. A.; Zare, R. N. *J. Chem. Phys.* **1998**, *108*, 8291.
(25) Rakitzis, T. P.; Kandel, S. A.; Alexander, A. J.; Kim, Z. H.; Zare, R. N. *Science* **1998**, *281*, 1346.
(26) Balint-Kurti, G. G.; Orr-Ewing, A. J.; Beswick, J. A.; Brown, A.; Vasyutinskii, O. S. *J. Chem. Phys.* **2002**, *116*, 10760.
(27) Balint-Kurti, G. G.; Brown, A.; Vasyutinskii, O. S. *Phys. Scr.* **2006**, *73*, C76.
(28) Clark, A. P.; Brouard, M.; Quadrini, F.; Vallance, C. *Phys. Chem. Chem. Phys.* **2006**, *8*, 5591.
(29) Brouard, M.; Cireasa, R.; Clark, A. P.; Quadrini, F.; Vallance, C. Atomic polarization in the photodissociation of polyatomic molecules In *Molecular Reaction and Photodissociation Dynamics in the Gas Phase*; Kleiber, P., Lin, K. C., Eds.; Research Signpost: Trivandrum, India, 2007.
(30) Simpson, W. R.; Orr-Ewing, A. J.; Kandel, S. A.; Rakitzis, T. P.; Zare, R. *J. Chem. Phys.* **1995**, *103*, 7299.
(31) Kandel, S. A.; Rakitzis, T. P.; Lev-On, T.; Zare, R. *J. Chem. Phys.* **1996**, *105*, 7550.
(32) Rakitzis, T. P.; Kandel, S. A.; Lev-On, T.; Zare, R. *J. Chem. Phys.* **1997**, *107*, 9392.
(33) Picheyev, B. V.; Smolin, A. G.; Vasyutinskii, O. S. *J. Phys. Chem.* **1997**, *101*, 7614.
(34) Korovin, K. O.; Picheyev; B, V.; Vasyutinskii, O. S.; Valipour, H.; Zimmermann, D. *J. Chem. Phys.* **2000**, *112*, 2059.
(35) Balint-Kurti, G. G.; Shapiro, M. *Chem. Phys.* **1981**, *61*, 137.
(36) Morse, M. D.; Band, Y. B.; Freed, K. F. *J. Chem. Phys.* **1983**, *78*, 6066.
(37) Balint-Kurti, G. G.; Shapiro, M. Quantum theory of molecular photodissociation In *Photodissociation and Photoionization*; Lawley, K. , Ed.; John Wiley & Sons, 1985.
(38) Roncero, O.; Villarreal, P.; Delgado-Barrio, G.; Halberstadt, N.; Beswick, J. A. *J. Phys. Chem.* **1994**, *98*, 3307.
(39) Uberna, R.; Hinchliffe, R. D.; Cline, J. I. *J. Chem. Phys.* **1995**, *103*, 7934.
(40) Fuglesang, C. D.; Baugh, D. A.; Pipes, L. C. *J. Chem. Phys.* **1996**, *105*, 9796.
(41) Mo, Y. X.; Suzuki, T. *J. Chem. Phys.* **1998**, *108*, 6780.
(42) Bracker, A. S.; Wouters, E. R.; Suits, A. G.; Vasyutinskii, O. S. *J. Chem. Phys.* **1999**, *110*, 6749.
(43) Mo, Y.; Suzuki, T. *J. Chem. Phys.* **2000**, *112*, 3463.
(44) Kuznetsov, V. V.; Vasyutinskii, O. S. *J. Chem. Phys.* **2005**, *123*, 034307.
(45) Zare, R. N. *Angular Momentum*; Wiley: New York, 1988.
(46) Blum, K. *Density Matrix Theory and Applications*, 2nd ed.; Plenum: New York, 1996.
(47) Varshalovich, D. A. Moskalev V. K. K. *Quantum Theory of Angular Momentum*; World Scientific: New York, 1988.
(48) Happer, W. *Rev. Mod. Phys.* **1972**, *44*, 170.
(49) Fano, U.; Macek, J. H. *Rev. Mod. Phys.* **1973**, *45*, 553.
(50) Mott, N. F.; Massey, H. S. W. *The Theory of Atomic Collision*, 3rd ed.; Oxford University Press: Oxford, U.K., 1965.
(51) Nikitin, E. E.; Umanskii, S. Y. *Theory of Slow Atomic Collisions*; Springer-Verlag: Berlin, 1984.
(52) Child, M. S. *Molecular Collision Theory*, reprint ed.; Dover Publications, Inc.: Mineola, NY, 1996.
(53) Kuznetsov, V. V.; Vasyutinskii, O. S. *J. Chem. Phys.* **2007**, *127*, 044308.
(54) Wang, Y.; Loock, H. P.; Cao, J.; Qian, C. X. W. *J. Chem. Phys.* **1995**, *102*, 808.
(55) Rakitzis, T. P.; Zare, R. N. *J. Chem. Phys.* **1999**, *110*, 3341.
(56) Eppink, A. T. J. B.; Parker, D. H.; Janssen, M. H. M.; Buijsse, B.; van der Zande, W. *J. Chem. Phys.* **1998**, *108*, 1305.
(57) Alexander, A. J.; Kim, Z. H.; Kandel, S. A.; Zare, R. N.; Rakitzis, T. P.; Asano, Y.; Yabushita, S. *J. Chem. Phys.* **2000**, *113*, 9022.
(58) Kummel, A. C.; Sitz, G. O.; Zare, R. N. *J. Chem. Phys.* **1988**, *88*, 6707.
(59) Alexandrov, E. B.; Chaika, M. P.; Khvostenko, G. I. *Interference of Atomic States*; Springer-Verlag: New York, 1993.
(60) Kupriayanov, D. V.; Vasyutinskii, O. S. *Chem. Phys.* **1993**, *171*, 25.
(61) Gordon, R. J.; Hall, G. E. Applications of Doppler spectroscopy in photofragmentation In *Advances in Chemical Physics*, Vol. XCVI; Prigogine, I., Rice, S., Eds.; John Wiley and Sons, Inc.: New York, 1996.
(62) Lee, S. K.; Silva, R.; Thamanna, S.; Vasyutinskii, O. S.; Suits, A. G. *J. Chem. Phys.* **2006**, *125*, 121101.
(63) Schinke, R. *Photodissociation Dynamics*; Cambridge University Press: Cambridge, U.K., 1993.
(64) Brown, A.; Balint-Kurti, G. G. *J. Chem. Phys.* **2000**, *113*, 1870.
(65) Brown, A.; Balint-Kurti, G. G. *J. Chem. Phys.* **2000**, *113*, 1879.
(66) Glass-Maujean, M.; Beswick, J. A. *Phys. Rev. A* **1987**, *36*, 1170.
(67) Flemming, E.; Wilhelmi, W.; Schmoranzer, H.; Glass-Maujean, M. *J. Chem. Phys.* **1995**, *103*, 4090.
(68) Landau, L. D.; Lifshitz, E. M. *Quantum Mechanics: Non-relativistic Theory. Course of Theoretical Physics*, 3rd ed.; Pergamon: London, 1977.
(69) Vasyutinskii, O. S. *Sov. Phys. JETP* **1981**, *54*, 855.
(70) Herzberg, G. *Molecular Spectra and Molecular Structure. I. Spectra of Diatomic Molecules*, 2nd ed.; D. van Nostrand: Toronto, Canada, 1950.
(71) Mulliken, R. S. *Phys. Rev.* **1930**, *36*, 1440.
(72) Saute, M.; Bussery, B.; Aubert-Frécon, M. *Mol. Phys.* **1984**, *51*, 1459.
(73) Zare, R.; Herschbach, D. *Proc. IEEE* **1963**, *51*, 173.
(74) Jonah, C. *J. Chem. Phys.* **1971**, *55*, 1915.
(75) Busch, G. E.; Wilson, K. R. *J. Chem. Phys.* **1972**, *56*, 3638.
(76) Demyanenko, A. V.; Dribinski, V.; Reisler, H.; Meyer, H.; Qian, C. X. W. *J. Chem. Phys.* **1999**, *111*, 7383.
(77) Smolin, A. G.; Nahler, N. H.; Vasyutinskii, O. S.; Vieuxmair, O. P. J.; Balint-Kurti, G. G.; Orr-Ewing, A. J.; Ashfold, M. N. R. *J. Chem. Phys.* **2006**, *124*, 094305.
(78) Rakitzis, T. P.; Samartzis, P. C.; Toomes, R. L.; Kitsopoulos, T. N.; Brown, A.; Balint-Kurti, G. G.; Vasyutinskii, O. S.; Beswick, J. A. *Science* **2003**, *300*, 1936.
(79) Rakitzis, T. P.; Samartzis, P. C.; Toomes, R. L.; Kitsopoulos, T. N. *J. Chem. Phys.* **2004**, *121*, 7222.
(80) Lee, S. K.; Townsend, D.; Vasyutinskii, O. S.; Suits, A. G. *Phys. Chem. Chem. Phys.* **2005**, *7*, 1.
(81) Korovin, K. O.; Veselov, A. A.; Mikheev, E. M.; Vasyutinski, O. S.; Zimmermann, D. *Opt. Spect.* **2005**,
(82) Rakitzis, T. P.; Kandel, S. A.; Alexander, A. J.; Kim, Z.; Zare, R. *J. Chem. Phys.* **1999**, *110*, 3351.
(83) Kim, Z. H.; Alexander, A. J.; Zare, R. N. *J. Phys. Chem.* **1999**, *103*, 10145.
(84) Rakitzis, T. P.; Samartzis, P. S.; Kitsopoulos, T. N. *J. Chem. Phys.* **1999**, *111*, 10415.
(85) Smolin, A. G.; Vasyutinskii, O. S.; Wouters, E. R.; Suits, A. G. *J. Chem. Phys.* **2004**, *121*, 1.
(86) Mo, Y.; Katayanagi, H.; Heaven, M.; Suzuki, T. *Phys. Rev. Lett.* **1996**, *77*, 830.
(87) Buijsse, B.; van der Zande, W.; Eppink, A.; Parker, D.; Lewis, B. R.; Gibson, S. T. *J. Chem. Phys.* **1998**, *108*, 7229.
(88) Ahmed, M.; Peterka, D. S.; Wouters, E. R.; Vasyutinskii, O. S.; Suits, A. G. *Faraday Discuss.* **1999**, *113*, 425.

(89) Mo, Y. X.; Katayanagi, H.; Suzuki, T. *J. Chem. Phys.* **1999**, *110*, 2029.
(90) Dylewski, S. M.; Geiser, J. D.; Houston, P. L. *J. Chem. Phys.* **2001**, *115*, 7460.
(91) Rakitzis, T. P.; Samartzis, P. C.; Kitsopoulos, T. N. *Phys. Rev. Lett.* **2001**, *87*, 123001.
(92) Rakitzis, T. P. *Chem. Phys. Lett.* **2001**, *342*, 121.
(93) Nestorov, V. K.; Hinchliffe, R. D.; Uberna, R.; Cline, J. I. *J. Chem. Phys.* **2001**, *115*, 7881.
(94) Brouard, M.; O'Keeffe, P.; Joseph, D. M.; Minayev, D. *Phys. Rev. Lett.* **2001**, *86*, 2249.
(95) Costen, M. L.; Hall, G. E. *Phys. Chem. Chem. Phys.* **2007**, *9*, 272.
(96) Rakitzis, T. P.; Hall, G. E.; Costen, M. L.; Zare, R. N. *J. Chem. Phys.* **1999**, *111*, 8751.
(97) Alexander, A. J.; Kim, Z. H.; Zare, R. N. *J. Chem. Phys.* **2003**, *118*, 10566.
(98) Dylewski, S. M.; Geiser, J. D.; Houston, P. L. *J. Chem. Phys.* **2001**, *115*, 7460.
(99) Siebbeles, L. D. A.; Schins, J. M.; van der Zande, W. J.; Los, J.; Glass-Maujean, M. *Phys. Rev. A* **1991**, *44*, 343.
(100) Siebbeles, L. D. A.; Schins, J. M.; Los, J.; Glass-Maujean, M. *Phys. Rev. A* **1991**, *44*, 1584.
(101) Glass-Maujean, M.; Siebbeles, L. D. A. *Phys. Rev. A* **1991**, *44*, 1577.
(102) Siebbeles, L. D. A.; Beswick, J. A. *J. Chem. Soc., Faraday Trans.* **1992**, *88*, 2565.
(103) Kim, H.; Dooley, K. S.; North, S. W.; Hall, G. E.; Houston, P. L. *J. Chem. Phys.* **2006**, *125*, 133316.
(104) Zare, R. N. *Ber. Bunsenges Phys. Chem.* **1982**, *86*, 422.
(105) Liyanage, R.; Gordon, R. J. *J. Chem. Phys.* **1997**, *107*, 7209.
(106) Mukamel, S.; Jortner, J. *J. Chem. Phys.* **1974**, *61*, 5348.
(107) Brouard, M.; Clark, A. P.; Vallance, C.; Vasyutinskii, O. S. *J. Chem. Phys.* **2003**, *119*, 771.
(108) Brouard, M.; Cireasa, R.; Clark, A. P.; Preston, T. J.; Vallance, C.; Groenenboom, G. C.; Vasyutinskii, O. S. *J. Phys. Chem.* **2004**, *108*, 7965.
(109) Kummel, A. C.; Sitz, G. O.; Zare, R. N. *J. Chem. Phys.* **1986**, *85*, 6874.
(110) Chichinin, A. I.; Gericke, K.-H.; Einfeld, T. S.; Maul, C. In *Imaging in Molecular Dynamics: Technology and Applications*; Whitaker, B. J., Ed.; University Press, Cambridge, U.K., 2003.
(111) Chichinin, A. I.; Shternin, P. S.; Goedeke, N.; Maul, C.; Vasyutinskii, O. S.; Gericke, K.-H. *J. Chem. Phys.* **2006**, *125*, 034310.
(112) Shternin, P. S.; Ivanov, V. K.; Suits, A. G.; Vasyutinskii, O. S. *Phys. Chem. Chem. Phys.* **2006**, *8*, 2972.
(113) Mo, Y.; Suzuki, T. *J. Chem. Phys.* **1998**, *109*, 4691.
(114) Meyer, H. *Chem. Phys. Lett.* **1994**, *230*, 510.
(115) Bass, M. J.; Brouard, M.; Clark, A. P.; Vallance, C.; Martinez-Haya, B. *Phys. Chem. Chem. Phys.* **2003**, *5*, 856.
(116) Wouters, E. R.; Beckert, M.; Russell, L. J.; Rosser, K. N.; Orr-Ewing, A. J.; Ashfold, M. N. R.; Vasyutinskii, O. S. *J. Chem. Phys.* **2002**, *117*, 2087.
(117) Townsend, D.; Lee, S. K.; Suits, A. G. *Chem. Phys.* **2004**, *301*, 197.
(118) Strickland, R. N.; Chandler, D. W. *Appl. Opt.* **1991**, *30*, 1811.
(119) Castleman, K. R. *Digital Image Processing*; Prentice-Hall: Englewood Cliffs, New York, 1996.
(120) Dribinski, V.; Ossadtchi, A.; Mandelshtam, V.; Reisler, H. *Rev. Sci. Instrum.* **2002**, *73*, 2634.
(121) Suzuki, T.; Katayanagi, H.; Mo, Y.; Tonokura, K. *Chem. Phys. Lett.* **1996**, *256*, 90.
(122) Gebhardt, C. R.; Rakitzis, T. P.; Samartzis, P. C.; Ladopoulos, V.; Kitsopoulos, T. N. *Rev. Sci. Instrum.* **2001**, *72*, 3848.
(123) Townsend, D.; Minitti, M. P.; Suits, A. G. *Rev. Sci. Instrum.* **2003**, *74*, 2530.
(124) Lin, J. J.; Zhou, J.; Shiu, W.; Liu, K. *Rev. Sci. Instrum.* **2003**, *74*, 2495.
(125) Eppink, A. T. J. B.; Parker, D. H. *Rev. Sci. Instrum.* **1997**, *68*, 3477.
(126) Parker, D. H.; Eppink, A. T. J. B. *J. Chem. Phys.* **1997**, *107*, 2357.
(127) Rakitzis, T. P.; Kitsopoulos, T. N. *J. Chem. Phys.* **2002**, *116*, 9228.
(128) Chestakov, D. A.; Parker, D. H.; Vidma, K. V.; Rakitzis, T. P. *J. Chem. Phys.* **2006**, *124*, 024315.
(129) Asano, Y.; Yabushita, S. *Chem. Phys. Lett.* **2003**, *372*, 348.
(130) Cooper, M. J.; Jackson, P. J.; Rogers, L. J.; Orr-Ewing, A. J.; Ashfold, M. N. R.; Whitaker, B. J. *J. Chem. Phys.* **1998**, *109*, 4367.
(131) Beckert, M.; Wouters, E. R.; Ashfold, M. N. R.; Wrede, E. *J. Chem. Phys.* **2003**, *119*, 9576.
(132) Smolin, A. G.; Orr-Ewing, A. J.; Vasyutinskii, O. S. *Mol. Phys.* **2007**, *105*, 885.
(133) Rakitzis, T. P.; Samartzis, P. C.; Toomes, R. L.; Tsigaridas, L.; Coriou, M.; Chestakov, D.; Eppink, A. T. J. B.; Parker, D. H.; Kitsopoulos, T. N. *Chem. Phys. Lett.* **2002**, *364*, 115.
(134) Brown, A.; Balint-Kurti, G. G.; Vasyutinskii, O. S. *J. Phys. Chem. A* **2004**, *108*, 7790.
(135) Alexander, M. H.; Pouilly, B.; Duhoo, T. *J. Chem. Phys.* **1993**, *99*, 1752.
(136) Rakitzis, T. P. *Phys. Rev. Lett.* **2005**, *94*, 083005.
(137) Smolin, A. G.; Vasyutinskii, O. S.; Balint-Kurti, G. G.; Brown, A. *J. Phys. Chem.* **2006**, *110*, 5371.
(138) Huebert, B. J.; Martin, R. M. J. *J. Phys. Chem.* **1968**, *72*, 3046.
(139) Brown, A. *J. Chem. Phys.* **2005**, *122*, 084301.
(140) Jodoin, D. N.; Brown, A. *J. Chem. Phys.* **2005**, *123*, 054301.
(141) LeRoy, R. J.; Kraemer, G. T.; Manzhos, S. *J. Chem. Phys.* **2002**, *117*, 9353.
(142) Alekseyev, A. B.; Liebermann, H. P.; Kokh, D. B.; Buenker, R. J. *J. Chem. Phys.* **2000**, *113*, 6174.
(143) Slanger, T. G.; Copeland, R. A. *Chem. Rev.* **2003**, *103*, 4731.
(144) Huang, Y. L.; Gordon, R. J. *J. Chem. Phys.* **1992**, *97*, 6363.
(145) Lambert, H. M.; Dixit, A. A.; Davis, E. W.; Houston, P. L. *J. Chem. Phys.* **2004**, *121*, 10437.
(146) Buijsse, B.; van der Zande, W. J.; Eppink, A.; Parker, D. H.; Lewis, B. R.; Gibson, S. T. *J. Chem. Phys.* **1998**, *108*, 7229.
(147) van Vroonhoven, M. C. G. N.; Groenenboom, G. C. *J. Chem. Phys.* **2002**, *117*, 5240.
(148) Brouard, M.; Cireasa, R.; Clark, A. P.; Preston, T. J.; Vallance, C. *J. Chem. Phys.* **2006**, *124*, 064309.
(149) Korovin, K. O.; Veselov, A. A.; Vasyutinski, O. S.; Zimmermann, D. *Opt. Spect.* **2002**, *93*, 530.
(150) Davidovits, P.; Mc.Fadden, D. L. *Alkali Halide Vapours*; Academic: New York, 1979.
(151) Coriou, A. M.; Parker, D. H.; Groenenboom, G. C.; Barr, J.; Novalbos, I. T.; Whitaker, B. J. *Eur. Phys. J. D* **2006**, *38*, 151.
(152) Hopper, D. G. *J. Chem. Phys.* **1984**, *80*, 4290.
(153) Brown, A.; Jimeno, P.; Balint-Kurti, G. G. *J. Phys. Chem.* **1999**, *103*, 11089.
(154) Janssen, M. H. M.; Teule, J. M.; Neyer, D. W.; Chandler, D. W.; Groenenboom, G. C. *Faraday Discuss.* **1999**, *320*, 117.
(155) Teule, T. M.; Groenenboom, G. C.; Neyer, D. W.; Chandler, D. W.; Janssen, M. H. M. *Chem. Phys. Lett.* **2000**, *320*, 177.
(156) Neyer, D. W.; Heck, A. J. R.; Chandler, D. W. *J. Chem. Phys.* **1999**, *110*, 3411.
(157) Felder, P.; Haas, B. M.; Huber, J. R. *Chem. Phys. Lett.* **1991**, *186*, 177.
(158) Neyer, D. W.; Heck, A. J. R.; Chandler, D. W.; Teule, J. M.; Janssen, M. H. M. *J. Phys. Chem. A* **1999**, *103*, 10388.
(159) Babikov, D.; Kendrick, B. K.; Walker, R. B.; Schinke, R.; Pack, R. T. *Chem. Phys. Lett.* **2003**, *372*, 686.
(160) Gao, Y. Q.; Marcus, R. A. *Science* **2001**, *293*, 259.
(161) Molina, L. T.; Molina, M. J. *J. Geophys. Res.* **1986**, *91*, 14501.
(162) Malicet, J.; Daumont, D.; Charbonnier, J.; Parisse, C.; Chakir, A.; Brion, J. *J. Atmos. Chem.* **1995**, *21*, 263.
(163) Geiser, J. D.; Dylewski, S. M.; Mueller, J. A.; Wilson, R. J.; Toumi, R.; Houston, P. L. *J. Chem. Phys.* **2000**, *112*, 1279.
(164) Thelen, M. A.; Gejo, T.; Harrison, J. A.; Huber, J. R. *J. Chem. Phys.* **1995**, *103*, 7946.
(165) Qu, Z.-W.; Zhu, H.; Schinke, R. *Chem. Phys. Lett.* **2003**, *377*, 359.
(166) Baloitcha, E.; Balint-Kurti, G. G. *Phys. Chem. Chem. Phys.* **2005**, *7*, 3829.
(167) Baloitcha, E.; Balint-Kurti, G. G. *J. Chem. Phys.* **2005**, *123*, 014306.
(168) Qu, Z. W.; Zhu, H.; Grebenshchikov, S. Y.; Schinke, R. *J. Chem. Phys.* **2005**, *123*, 074305.
(169) Suits, A. G.; Miller, R. L.; Bontuyan, L. S.; Houston, P. L. *J. Chem. Soc., Faraday Trans.* **1993**, *89*, 1443.
(170) Wilson, R. J.; Mueller, J. A.; Houston, P. L. *J. Phys. Chem. A* **1997**, *101*, 7593.
(171) Taniguchi, N.; Takahashi, K.; Matsumi, Y.; Dylewski, S. M.; Geiser, J. D.; Houston, P. L. *J. Chem. Phys.* **1999**, *111*, 6350.
(172) Hancock, G.; Pearson, P. J.; Ritchie, G. A. D.; Tibbetts, D. F. *Phys. Chem. Chem. Phys.* **2003**, *5*, 5386.
(173) Hancock, G.; Pearson, P. J.; Ritchie, G. A. D.; Tibbetts, D. F. *Chem. Phys. Lett.* **2004**, *393*, 425.
(174) Valentini, J. J.; Gerrity, D. P.; Phillips, J.-C. N.; Tabor, K. D. *J. Chem. Phys.* **1987**, *86*, 6745.
(175) Brouard, M.; Cireasa, R.; Clark, A. P.; Groenenboom, G. C.; Hancock, G.; Horrocks, S. J.; Quadrini, F.; Ritchie, G. A. D.; Vallance, C. *J. Chem. Phys.* **2006**, *125*, 133308.
(176) Horrocks, S. J.; Pearson, P. J.; Ritchie, G. A. D. *J. Chem. Phys.* **2006**, *125*, 133313.
(177) Denzer, W.; Horrocks, S. J.; Pearson, P. J.; Ritchie, G. A. D. *Phys. Chem. Chem. Phys.* **2006**, *8*, 1954.
(178) Suzuki, T.; Katayanagi, H.; Nanbu, S.; Aoyagi, M. *J. Chem. Phys.* **1998**, *109*, 5778.
(179) Sivakumar, N.; Hall, G. E.; Houston, P. L.; Hepburn, J. W.; Burak, I. *J. Chem. Phys.* **1988**, *88*, 3692.

(180) Strauss, C. E.; McBane, G. C.; Houston, P. L.; Burak, I.; Hepburn, J. W. *J. Chem. Phys.* **1989**, *90*, 5364.
(181) Cosofret, B. R.; Dylewski, S. M.; Houston, P. L. *J. Phys. Chem. A* **2000**, *104*, 10240.
(182) Kim, H. L.; Satyapal, S.; Brewer, P.; Bersohn, R. *J. Chem. Phys.* **1989**, *91*, 1047.
(183) Qi, F.; Sorkhabi, O.; Suits, A. G. *J. Chem. Phys.* **2000**, *112*, 10707.
(184) Qi, F.; Sorkhabi, O.; Suits, A. G.; Chien, S. H.; Li, W. K. *J. Am. Chem. Soc.* **2001**, *123*, 148.
(185) Carnell, M.; Peyerimhoff, S. D. *Chem. Phys. Lett.* **1993**, *212*, 654.
(186) Shternin, P. S.; Vasyutinskii, O. S. *J. Chem. Phys.* **2008**, *128*, 194314.
(187) Alexander, A. J.; Rakitzis, T. P. *Mol. Phys.* **2005**, *103*, 1665.
(188) Alexander, A. J. *Phys. Chem. Chem. Phys.* **2005**, *7*, 3693.
(189) Alexander, A. J. *J. Chem. Phys.* **2005**, *123*, 194312.
(190) Alexander, A. J. *J. Chem. Phys.* **2003**, *118*, 6234.
(191) Sofikitis, D.; Rubio-Lago, L.; Martin, M. R.; Brown, D. J. A.; Bartlett, N. C.-M.; Alexander, A. J.; Zare, R. N.; Rakitzis, T. P. *J. Chem. Phys.* **2007**, *127*, 144307.
(192) Sofikitis, D.; Rubio-Lago, L.; Alexander, A. J.; Rakitzis, T. P. *Europhys. Lett.* **2008**, *81*, 68002.

CR040085C